

DA 126454
TR 82-5

DTIC FILE COPY

TECHNICAL REPORT NO. 82-5
SEISMIC METHODS
OF
INFRASONIC SIGNAL DETECTION

ANNUAL REPORT NO. 1

DTIC
ELECTE
APR 06 1983
S E

Sponsored by

Advanced Research Projects Agency (DOD)
ARPA Order No. 4246
Monitored by AFOSR under Contract No. F49620-81-C-0056

Approved for public release;
distribution unlimited.

"Original contains color
plates: All DTIC reproductions
will be in black and
white"

UNCLASSIFIED

SECURITY CLASSIFICATION OF THIS PAGE (When Data Entered)

REPORT DOCUMENTATION PAGE		READ INSTRUCTIONS BEFORE COMPLETING FORM
1. REPORT NUMBER AFOSR-TR- 83-0131	2. GOVT ACCESSION NO. AD A126 454	3. RECIPIENT'S CATALOG NUMBER
4. TITLE (and Subtitle) Seismic Methods of Infrasonic Signal Detection		5. TYPE OF REPORT & PERIOD COVERED Annual Report No. 1
7. AUTHOR(s) F. J. Mauk, G. G. Sorrells, L. Grant, K. B. Taylor		6. PERFORMING ORG. REPORT NUMBER
9. PERFORMING ORGANIZATION NAME AND ADDRESS Teledyne Geotech 3401 Shiloh Road Garland, Texas 75040-1676		8. CONTRACT OR GRANT NUMBER(s) F49620-81-C-0056
11. CONTROLLING OFFICE NAME AND ADDRESS Defense Advanced Research Project Agency (DOD) Bolling AFB, D. C. 20332		10. PROGRAM ELEMENT, PROJECT, TASK AREA & WORK UNIT NUMBERS ARPA Order No. 4246
14. MONITORING AGENCY NAME & ADDRESS (if different from Controlling Office) AFOSR/NP Bolling AFB, D. C. 20332		12. REPORT DATE Sep 1982
		13. NUMBER OF PAGES 147
		15. SECURITY CLASS. (of this report) Unclassified
		15a. DECLASSIFICATION/DOWNGRADING SCHEDULE
16. DISTRIBUTION STATEMENT (of this Report) Approved for public release; distribution unlimited.		
17. DISTRIBUTION STATEMENT (of the abstract entered in Block 20, if different from Report) <i>Original contains color plates: All DTIC reproductions will be in black and white</i>		
18. SUPPLEMENTARY NOTES The views and conclusions contained in this document are those of the authors and should not be interpreted as necessarily representing the official policies either expressed or implied of the Defense Advanced Research Projects Agency or the U. S. Government.		
19. KEY WORDS (Continue on reverse side if necessary and identify by block number)		
20. ABSTRACT (Continue on reverse side if necessary and identify by block number) Infrasound monitoring using a three-component borehole seismograph and surface microbarograph array show that within a frequency band extending between about 0.005 Hz to about 0.05-0.1 Hz, depending on local wind conditions, the infrasonic depth will be no worse than, and can be considerably better than, that observed on a microbarogram. Results lend credence to the hypothesis that, within this frequency band, infrasonic signals generated by sources in the low to moderate kiloton yield range can be seismically observed and can be positively identified without the aid of microbarometric data.		

DD FORM 1 JAN 73 1473

EDITION OF 1 NOV 65 IS OBSOLETE

UNCLASSIFIED

SECURITY CLASSIFICATION OF THIS PAGE (When Data Entered)

AIR FORCE OFFICE OF SCIENTIFIC RESEARCH (AFSC)
NOTICE OF TRANSMITTAL TO DTIC
This technical report has been reviewed and is
approved for public release IAW AFR 190-12.
Distribution is unlimited.
MATTHEW J. KERPER
Chief, Technical Information Division



TECHNICAL REPORT NO. 82-5

SEISMIC METHODS
OF
INFRASONIC SIGNAL DETECTION

ANNUAL REPORT NO. 1

by

F. J. Mauk, G. G. Sorrells, L. Grant, K. B. Taylor

Accession For	
NTIS GRA&I	<input checked="checked" type="checkbox"/>
DTIC TAB	<input type="checkbox"/>
Unannounced	<input type="checkbox"/>
Justification	
By _____	
Distribution/	
Availability Codes	
Dist	Avail and/or Special
A	

The views and conclusions contained in this document are those of the authors and should not be interpreted as necessarily representing the official policies, either expressed or implied, of the Defense Advanced Research Projects Agency or the U. S. Government.

Sponsored by

Advanced Research Projects Agency (DOD)
ARPA Order No. 4246
Monitored by AFOSR under Contract #F49620-81-C-0056

TELEDYNE GEOTECH
3401 Shiloh Road
Garland, Texas 75040-1676

CPT 204

30 September 1982

TABLE OF CONTENTS

	<u>Page</u>
LIST OF SYMBOLS AND NOMENCLATURE	iii
LIST OF FIGURES	v
LIST OF TABLES	x
1. BACKGROUND	
1.1 Rationale for Infrasonic-Acoustic Signal Detection Research	1
1.2 The Previous Method to Detect and Analyze Infrasonic Signals	1
1.3 An Alternative Method to Detect and Analyze Infrasonic Signals	2
2. RESEARCH PROGRAM	5
2.1 Proposed Research Objective	5
2.2 Instrumentation and Data Collection Methodology	6
2.3 Evaluation of Ambient Noise Fields and Effects on Infrasonic Signal Discrimination	10
2.4 Comparative Analysis of Recorded Infrasonic Signals	24
2.4.1 The Eruption Sequence of El Chichon Volcano 29 March - 6 April 1982 Qualitative Analysis	24
2.4.2 Quantitative Analysis of the El Chichon Eruptions	59
2.4.3 Estimation of Energy Release from the El Chichon Explosions	84
3. SUMMARY, CONCLUSIONS AND RECOMMENDATIONS	93
4. REFERENCES	95
APPENDIX A - Derivation of Infrasonic SNR	
APPENDIX B - Earth Transfer Function	
APPENDIX C - El Chichon Reports from SEAN Bulletin, Volume 7, Numbers 3, 4, 5, and 6	
APPENDIX D - Selected References on Volcanic Explosivity, Energy and Magnitude	
APPENDIX E - Selected References on the Propagation Characteristics of Acoustic-Gravity Modes in the Atmosphere	
APPENDIX F - Abstracts of Papers Presented	

LIST OF SYMBOLS AND NOMENCLATURE

A_1 -	The collection of all gravity and infrasonic-acoustic modes which constitute a signal train that has arrived at the recording site from the source by traveling the shortest great-circle (direct) route.
A_2 -	The gravity-infrasonic acoustic mode wave train which travels the antipodal great circle route from the source to the receiver. Some authors refer to this as B_1 .
GR -	Atmospheric guided waves, commonly called gravity modes, characterized by well-defined, upper-frequency cutoffs. GK modes are numbered in inverse order of the proximity of their modal surfaces to the origin.
GR_0 -	A relatively non-dispersive gravity mode characterized by periods greater than 270 seconds and group velocities of 310 ± 12 m/sec. Faster velocities in the downwind direction.
GR_1 -	A gravity mode considerably more dispersive than GR_0 with group velocities of 225 ± 25 m/sec. Although GR_1 is theoretically predicted, it has not been observed.
$G_z(f)$ -	Transfer function relating infrasonic atmospheric pressure variations to vertical earth movements.
$G_{zm}(\omega)$ -	Cross-power spectral density between the vertical seismograph power and microbarograph power spectra.
g_{zn} -	Greens function for vertical component of displacement caused by wind noise.
G_{zs} -	Greens function for vertical component of displacement caused by an infrasonic signal.
ΔH	Volcanic column height (km)
I_{zm} -	Difference in signal-to-noise ratios on vertical-mode seismograms and microbarograms
\dot{M}	Mass flux (g/sec)
$M(\omega)$ -	Microbarograph power spectra
$m(t)$ -	Output of a microbarograph
$N_m(f)^2$	Microbarometric noise corrected for instrument responses
M_z -	Vertical component of seismic noise

LIST OF SYMBOLS AND NOMENCLATURE (continued)

$N_z(f)^2$	Estimated power spectra of vertical seismic noise
P_n	Turbulent noise created by the wind
P_s	Infrasonic pressure signal
\dot{Q}	Thermal energy flux (ergs/sec)
r_m	Response of microbarograph
r_s	Response of the seismograph
S	Atmospheric guided waves distinguished from the GR modes in that they have no upper frequency cutoff. Numerical ordering is related to the proximity of the modes' surfaces in the frequency-phase velocity space to the origin. Frequently referred to as infrasonic-acoustic modes.
S_0	An acoustic mode with appreciable amplitude only for periods between 300 seconds and 150 seconds. The group velocities are 310 ± 20 m/sec for wave periods from 220 seconds and 150 seconds.
S_1	Highly dispersive acoustic modes in which composite Lamb and ray-refraction directing mechanisms are important. S_1 modes can contribute significantly to the A trains for wave periods from 210 seconds to 90 seconds. For wave periods from 210 seconds to 135 seconds, the group velocities increase from 200 ± 5 m/sec to 300 ± 15 m/sec. From periods of 135 seconds to 90 seconds, the group velocity is constant at 300 ± 15 m/sec.
S_2	Highly dispersive acoustic modes similar to S_1 . Principally contribute to A trains at periods from 165 seconds to 90 seconds. Group velocities at the longest periods are 200 ± 10 m/sec and 280 ± 10 m/second at periods approximately 90 seconds.
S_n ($n > 2$)	Higher order acoustic modes whose principal contribution to the A trains are as highly dispersed waves with wave periods less than 90 seconds and group velocities from 200 to 300 m/sec.
SNR_z	Vertical seismic infrasonic SNR
$(SNR)_z$	Signal-to-noise ratio for earth motion
SNR_m	Microbarometric seismic infrasonic SNR
$(SNR)_m$	Signal-to-noise ratio for pressure field
$u_z(t)$	Output of a vertical seismograph

LIST OF SYMBOLS AND NOMENCLATURE (continued)

- $U_z(\omega)$ - Seismograph vertical power spectra
(*) - Denotes convolution

LIST OF FIGURES

<u>Number</u>		<u>Page</u>
1	(a) Infrasonic acoustic signals from a 55-60 MT atmospheric nuclear test 31 October 1961 recorded at stations PAL (6680 km) and PIE (11,592 km) (after Donn and Shaw, 1967). (b) Infrasonic acoustic signals from the 18 May 1980 explosion of Mt. St. Helens recorded on the ANMO seismograph	3
2	Theoretical gain in the infrasonic signal to wind noise ratio achieved through the use of a buried vertical seismograph as compared to a microbarograph	4
3	McKinney, Texas, microbarograph/seismograph experiment layout	7
4	Seismic and recording subsystems - McKinney infrasonic study	8
5	Relative responses of seismograph channels to displacement and microbarograph channels to pressure	9
6	Power spectral densities of calibrated microbarometric data corrected for instrument response (MKB#1) for two wind conditions	11
7	Power spectral densities of calibrated vertical seismic data corrected for instrument response during two wind conditions	13
8	Power spectral densities of calibrated north-south seismic data corrected for instrument response during two wind conditions	14
9	Power spectral densities of calibrated east-west seismic data corrected for instrument response during two wind conditions.	15
10	Ordinary coherence estimates between microbarometric and seismic noise fields under low wind conditions. (a) Microbarometric and vertical seismic component (b) Microbarometric and north-south seismic component. (c) Microbarometric and east-west seismic component. Data are uncorrected for instrument response.	16

LIST OF FIGURES (continued)

<u>Number</u>		<u>Page</u>
11	Ordinary coherence estimates between microbarometric and seismic noise fields under moderate wind conditions. (a) Microbarometric and vertical seismic component. (b) Microbarometric and north-south seismic component. (c) Microbarometric and east-west seismic component. Data are uncorrected for instrument responses. Seismic data are low-pass filtered (corner 0.0417 hz, 24 db/octave roll off) prior to coherence estimation.	17
12	Theoretical response of an elastic layered half space to atmospheric loading.	19
13	The difference between signal-to-noise ratios of vertical seismic and microbarometric data under low and moderate wind conditions	20
14	Comparison of observed and calculated vertical displacement earth response functions for an infrasonic signal. The data shown are appropriate for observations made at a depth of 150 meters at McKinney, Texas.	22
15	Comparison of observed and calculated north-south horizontal displacement earth response functions for infrasonic signals. The data shown are appropriate for observations made at a depth of 150 meters at McKinney, Texas.	23
16	NOAA satellite infrared image of the El Chichon eruption 29 March 1982. This image was taken approximately two hours after the initiation of the eruption.	25
17	Relative responses of the seismographs to displacement prior to and post filtration (low-pass filter corner 24 seconds, 24 dB/octave roll off). Response of the microbarograph to pressure is shown for comparison.	30
18	El Chichon eruption time 088 05:32 UCT. Black line - Low-pass filtered vertical seismogram. Red line - Microbarograph array beam steered at azimuth 168°	31/32
19	El Chichon eruption time 088 05:32 UCT. Black line - Low-pass filtered radial (168°) seismogram. Red line - Microbarograph array beam steered at azimuth 168°	33/34

LIST OF FIGURES (continued)

<u>Number</u>		<u>Page</u>
20	El Chichon eruption time 088 05:32 UCT. Black line - Low-pass filtered transverse (78°) seismogram. Red line - Microbarograph array beam steered at azimuth 168°	35/36
21	El Chichon eruption time 093 08:50 UCT. Black line - Low-pass filtered vertical seismogram. Red line - Microbarograph array beam steered at azimuth 168°	37
22	El Chichon eruption time 093 08:50 UCT. Black line - Low-pass filtered radial (168°) seismogram. Red line - Microbarograph array beam steered at azimuth 168°	38
23	El Chichon eruption time 093 08:50 UCT. Black line - Low-pass filtered transverse (78°) seismogram. Red line - Microbarograph array beam steered at azimuth 168°	39
24	El Chichon eruption time 093 09:12 UCT. Black line - Low-pass filtered vertical seismogram. Red line - Microbarograph array beam steered at azimuth 168°	40
25	El Chichon eruption time 093 09:12 UCT. Black line - Low-pass filtered radial (168°) seismogram. Red line - Microbarograph array beam steered at azimuth 168°	41
26	El Chichon eruption time 093 09:12 UCT. Black line - Low-pass filtered transverse (78°) seismogram. Red line - Microbarograph array beam steered at azimuth 168°	42
27	El Chichon eruption time 094 02:00 UCT. Black line - Low-pass filtered vertical seismogram. Red line - Microbarograph array beam steered at azimuth 168°	43
28	El Chichon eruption time 094 02:00 UCT. Black line - Low-pass filtered radial (168°) seismogram. Red line - Microbarograph array beam steered at azimuth 168°	44

LIST OF FIGURES (continued)

<u>Number</u>		<u>Page</u>
29	El Chichon eruption time 094 02:00 UCT. Black line - Low-pass filtered transverse (78°) seismogram. Red line - Microbarograph array beam steered at azimuth 168°	45/46
30	El Chichon eruption time 094 11:22 UCT. Black line - Low-pass filtered vertical seismogram. Red line - Microbarograph array beam steered at azimuth 168°	47/48
31	El Chichon eruption time 094 11:22 UCT. Black line - Low-pass filtered radial (168°) seismogram. Red line - Microbarograph array beam steered at azimuth 168°	50
32	El Chichon eruption time 094 11:22 UCT. Black line - Low-pass filtered transverse (78°) seismogram. Red line - Microbarograph array beam steered at azimuth 168°	52
33	Noise sample origin time 094 11:54 UCT. Black line - Low-pass filtered vertical seismogram. Red line - Microbarograph MKB No. 1	53/54
34	Noise sample origin time 094 11:54 UCT. Black line - Low-pass filtered north-south horizontal seismogram. Red line - Microbarograph MKB No. 1	55/56
35	Noise sample origin time 094 11:54 UCT. Black line - Low-pass filtered east-west horizontal seismogram. Red line - Microbarograph MKB No. 1	57/58
36	Ordinary coherence estimates for the El Chichon eruption 088 between the microbarograph array beam and the vertical (a), radial (b), and transverse (c) seismograms (9 block sample/75% overlap).	61
37	Ordinary coherence estimates for the El Chichon eruption 088 between pairs of the three seismogram components: (a) vertical and radial, (b) vertical and transverse, (c) radial and transverse (9 block sample/75% overlap).	62

LIST OF FIGURES (continued)

<u>Number</u>		<u>Page</u>
38	Ordinary coherence estimates for the El Chichon eruption 093-A between the microbarograph array beam and the vertical (a), radial (b), and transverse (c) seismograms (5 block sample/75% overlap).	63
39	Ordinary coherence estimates for the El Chichon eruption 093-A between pairs of the three seismogram components: (a) vertical and radial, (b) vertical and transverse, (c) radial and transverse (5 block sample/75% overlap).	64
40	Ordinary coherence estimates for the El Chichon eruption 093-B between the microbarograph array beam and the vertical (a), radial (b), and transverse (c) seismograms (5 block sample/75% overlap).	65
41	Ordinary coherence estimates for the El Chichon eruption 093-B between pairs of the three seismogram components: (a) vertical and radial, (b) vertical and transverse, (c) radial and transverse (5 block sample/75% overlap).	66
42	Ordinary coherence estimates for the El Chichon eruption 094-A between the microbarograph array beam and the vertical (a), radial (b), and transverse (c) seismograms (5 block sample/75% overlap).	67
43	Ordinary coherence estimates for the El Chichon eruption 094-A between pairs of the three seismogram components: (a) vertical and radial, (b) vertical and transverse, (c) radial and transverse (5 block sample/75% overlap).	68
44	Ordinary coherence estimates for the El Chichon eruption 094-B between the microbarograph array beam and the vertical (a), radial (b), and transverse (c) seismograms (13 block sample/75% overlap).	69
45	Ordinary coherence estimates for the El Chichon eruption 094-B between pairs of the three seismogram components: (a) vertical and radial, (b) vertical and transverse, (c) radial and transverse (13 block sample/75% overlap).	70
46	Period and peak-to-peak amplitude (corrected for instrument response) measurements of atmospheric gravity/acoustic modes excited by five explosive eruptions of El Chichon volcano. Microbarometric signals recorded at McKinney, Texas ($\Delta = 16.16^\circ$).	73/74

LIST OF FIGURES (continued)

<u>Number</u>		<u>Page</u>
47	Period and peak-to-peak amplitude (corrected for instrument response) measurements of atmospheric gravity/acoustic modes excited by five explosive eruptions of El Chichon Volcano. Long-period vertical seismic signals recorded at McKinney, Texas (= 16.16°).	79/80
48	Period and peak-to-peak amplitude (corrected for instrument response) measurements of atmospheric gravity/acoustic modes excited by five explosive eruptions of El Chichon volcano. Long-period radial seismic signals recorded at McKinney, Texas (= 16.16°).	81/82
49	Moving window analysis of the microbarometric A_1 wave train from the 093A eruption of El Chichon volcano. Regions of the period (5-500 seconds) versus velocity (240-360 m/sec) space characterized by local power maxima are shaded for clarity.	85
50	Moving window analysis of the microbarometric A_1 wave train from the 093A eruption of El Chichon volcano. The period range has been restricted from 5 to 100 seconds to enhance the relative power details of figure 49. Regions of the period versus velocity space characterized by relative local power maxima are shaded for clarity. See text for additional discussion.	86
51	Eruption cloud height versus kinetic energy	88
52	Relationship between the maximum amplitude of infrasonic-acoustic A_1 wave train and distance. Theoretical attenuation curves are for the relationships of Wexler and Hass (1962)(solid); Harkriver (1964)(dashed); and three inverse distance relationships $R^{-1/2}$, $R^{-2/3}$, R^{-1} . Observed data are for the 30 October 1961 Novaya Zemlya 58 MT weapons test (from Wexler and Hass).	90

LIST OF TABLES

<u>Number</u>		<u>Page</u>
1	Origin times of ten identifiable eruption phases	26
2	Criteria for estimation of the volcanic explosivity index (VEI) [from Newhall and Self (1982)]	27
3	Amplitude and period measurements of microbarometric signals from five eruptions of El Chichon volcano	71/72
4	Amplitude and period measurements of seismically recorded atmospheric signals from five eruptions of El Chichon volcano	77/78
5	Energy and equivalent yield estimations for the El Chichon Explosions	92

1. BACKGROUND

1.1 RATIONALE FOR INFRASONIC-ACOUSTIC SIGNAL DETECTION RESEARCH

It is reasonable to assume that, within the next five years, a relatively large number of new nations will acquire a nuclear weapons capability. Moreover, it is likely that their initial tests of this capability will be carried out in the atmosphere. Recent events have indicated the need for additional, independent data sources to verify or corroborate the information provided by current atmospheric nuclear test monitoring systems. This need can readily be met by providing a means for detecting and identifying the infrasonic signals generated by atmospheric nuclear explosions.

1.2 THE PREVIOUS METHOD TO DETECT AND ANALYZE INFRASONIC SIGNALS

In the past, the capability to detect and identify infrasonic signals was vested in a network of small microbarograph arrays. These arrays, which are now largely abandoned, consisted of 4-6 microbarographs which had the intrinsic sensitivity to detect atmospheric pressure variations as small as a few tenths of a microbar in the frequency range of 0.001 to 1 Hz. Thus, in the absence of contributions from external noise sources, these arrays had the potential for detecting infrasonic signals generated by atmospheric nuclear explosions in the low kiloton yield range at distances up to a few thousand kilometers or so. Unfortunately, this potential could never be realized in practice because the relatively large atmospheric pressure fluctuations created by the local surface wind can easily be of the order of a few tens to a few hundred microbars.

In order to combat the wind noise problem, pipe arrays were commonly attached to the inlet port of the microbarographs (cf Daniels, 1959). The pipe array typically consisted of a hollow tube, several hundred meters in length and a few centimeters in diameter, with inlet ports spaced at intervals of a meter or so. Given this configuration, the pipe array functioned as a passive wavelength filter which would selectively attenuate short wavelength components of the atmospheric pressure field relative to the longer wavelengths. In the idealized case where the infrasonic signal field is completely organized and the wind noise field is completely disorganized, the pipe array will provide an SNR gain equal to $N^{1/2}$ where N is the number of inlet ports. Experience demonstrated that this gain could generally be approached at frequencies greater than about .1 to .2 Hz for most commonly observed wind conditions. However, for moderately high winds and frequencies below .1 Hz, the wind noise field became organized on a scale comparable to the maximum feasible dimensions of the pipe array (McDonald et al, 1971). Consequently, its capability to suppress wind noise was seriously degraded under these conditions. In order to achieve greater noise suppression at frequencies less than .1 Hz, plans were under way in the early 1970's to deploy large-scale arrays of microbarographs. While implementation of this approach is certainly well within the current state of the art, the probable cost of developing and operating an advanced network leads to the consideration of alternate methods.

1.3 AN ALTERNATIVE METHOD TO DETECT AND ANALYZE INFRASONIC SIGNALS

During the early 1970's, the AFOSR sponsored basic studies of the relationship between local atmospheric pressure changes and low-frequency seismic noise (Sorrells, 1971; Sorrells and Goforth, 1973; Sorrells and Douze 1974; Savino et al, 1972; Savino and Rynn, 1972). An important result of these investigations was the prediction and experimental confirmation that the quasi-static earth movements triggered by the passage of infrasonic waves could be detected at the outputs of a sensitive, long-period seismograph system. This prediction was verified for the case of large, atmospheric nuclear explosions through observations by Sorrells et al (1971) and Savino and Rynn (1972). In addition, later research by Sorrells and Douze (1974) demonstrated that relatively weak infrasonic signals from naturally occurring sources also were detectable seismically.

Equally important was the prediction and observation that the earth acts as a passive wavelength filter with respect to the atmospheric pressure fields, selectively attenuating the shorter wavelength components to a greater degree than the longer wavelength components. The properties of this filter are controlled by the local distribution of elastic constants and the depth of observation and are virtually independent of the state of organization of the input field. Since, for a given frequency, the convective wavelength of wind-generated pressure noise may be an order of magnitude shorter than that of an infrasonic signal, relatively large SNR gains are theoretically possible regardless of the state of organization of the signal and noise field. This point is illustrated by the results shown in figure 2. This is the theoretical infrasonic SNR gain, predicted for observations made at a depth of 100 meters in a homogenous, isotropic, perfectly elastic half space with equivalent Lamé constants. The results shown are appropriate for a vertical seismograph and assume that the propagation speed of the signal is 330 m/sec while convection velocity of the wind-generated noise is 10 m/sec. Observe that the predicted SNR gain is greater than 30 dB throughout the entire frequency range of interest.

Thus, installation of a seismograph system at an appropriate depth in a given location is functionally equivalent to attaching a pipe array to the inlet port of a microbarograph, insofar as the enhancement of infrasonic signal-to-noise ratios is concerned.

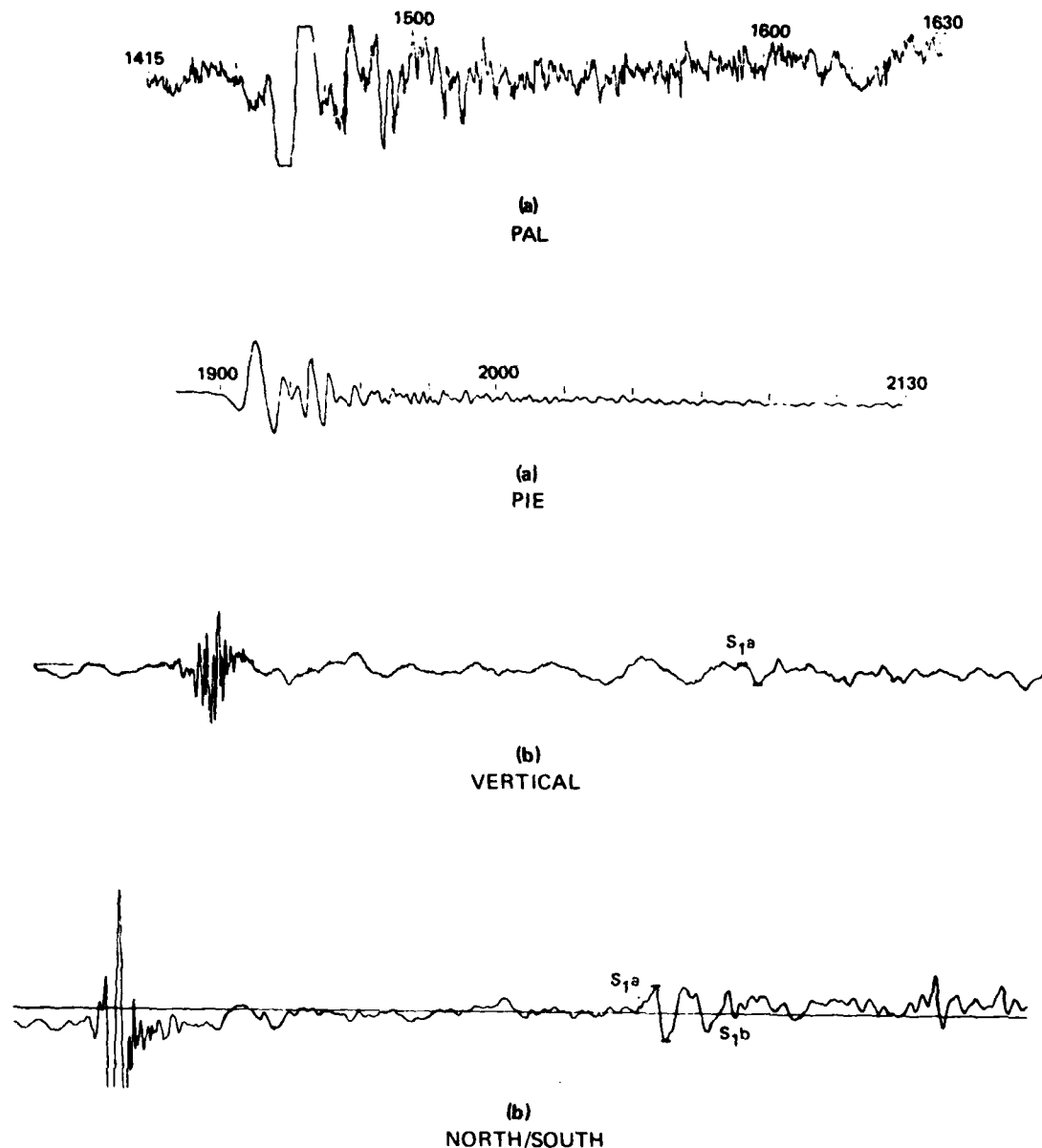


FIGURE 1. (a) INFRASONIC ACOUSTIC SIGNALS FROM A 55-60 MT ATMOSPHERIC NUCLEAR TEST 31 OCTOBER 1961 RECORDED AT STATIONS PAL (6680 km) AND PIE (11,592 km) (AFTER DONN AND SHAW, 1967). (b) INFRASONIC ACOUSTIC SIGNALS FROM THE 18 MAY 1980 EXPLOSION OF MT. ST HELENS RECORDED ON THE ANMO SEISMOGRAPH.

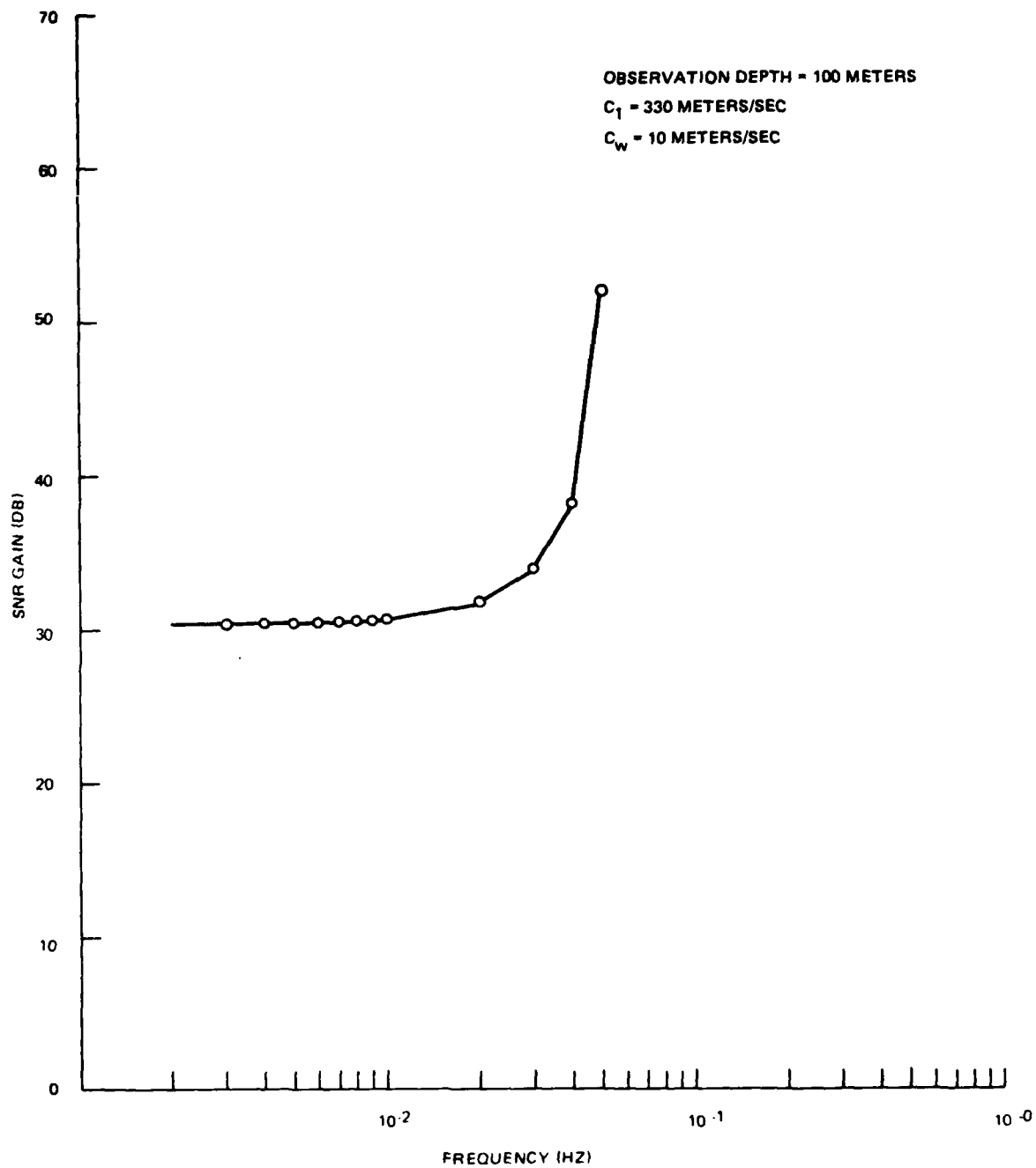


FIGURE 2. THEORETICAL GAIN IN THE INFRASONIC SIGNAL TO WIND NOISE RATIO ACHIEVED THROUGH THE USE OF A BURIED VERTICAL SEISMOGRAPH AS COMPARED TO A MICROBAROGRAPH

G11238A

2. RESEARCH PROGRAM

2.1 PROPOSED RESEARCH OBJECTIVE

The primary goal of this research program is to assess the capability of detecting and analyzing infrasonic-acoustic signals recorded by three-component, long-period seismograph systems. Accomplishment of this program goal required completion of three particular tasks. The first task was to obtain comparable data from a collocated, standard microbarograph array and three-component KS-36000 (SRO) seismograph systems. Since these data were not available at the inception of the program, appropriate instrumentation had to be installed to collect the data. This phase of the program will be discussed in section 2.2. The second task was to analyze the data collected and evaluate the relative capabilities of the microbarograph array method versus the alternative seismic method for discrimination of infrasonic signals. These analyses required investigations of spectral characteristics of both the ambient noise fields recorded by the two sensor systems, investigations of identified infrasonic signals and analysis of the earth response transfer function. The analyses of the ambient noise fields and their effects on infrasonic signal discrimination and the theoretical and observed earth response transfer functions will be discussed in section 2.3. Comparative analyses of recorded infrasonic signals, with emphasis on the detonation and the explosion sequence of El Chichon volcano, will be discussed in section 2.4. The third and final task of this research program was to investigate an alternative method to enhance detection of infrasonic signals produced by low-yield (< 10 KT) nuclear weapons tests. Initially, it was proposed that recording and utilizing multicomponent earth strain data in conjunction with inertial data may enhance significantly the capability to detect infrasonic signals. Because of delays in fabrication, installation, and effective operation of a strain-inertial system (a contemporaneous research program), however, this research objective was not accomplished and will not be discussed in this technical report.

The results of this research program are summarized in section 3 of this report. Conclusions and recommendations for further research also are included in this section.

2.2 INSTRUMENTATION AND DATA COLLECTION METHODOLOGY

Comparative analysis of the capability to record and detect infrasonic-acoustic signals via a conventional microbarograph array and a three-component, borehole seismograph system required the installation and operation of collocated instrumentation. A temporary site for simultaneously recording earth motions and atmospheric pressure variations was established near McKinney, Texas, (approximately thirty miles north of Dallas) late in 1980. The experimental sensor system consisted of a three-component, long-period borehole seismograph (Teledyne Geotech model KS-36000), five model M-4 microbarographs (loaned by Southern Methodist University) and a high-resolution anemometer. The spatial configuration of the instrumentation is illustrated in figure 3. The location of the KS-36000 seismograph is illustrated as a solid circle and is at 33°14'56"N latitude, 96°36'07"W longitude at a depth of 152 meters below the surface. The sites of the microbarographs are illustrated in figure 3 as open circles. One of the microbarographs and the anemometer are surface collocated with the KS-36000 seismograph. The distances and azimuths of the outer four microbarographs from the central facility are given on the illustration. Microbarographs MKB3, MKB4, and MKB5 were located in shallow vaults; the other two, MKB1 and MKB2, were located on the surface. Each microbarograph was fitted at the inlet port with a fifteen-meter length of garden hose (19mm ID) perforated at one-meter intervals. The purpose of this pipe was to attenuate undesirable high-frequency, atmospheric turbulence effects.

A schematic diagram of the total experimental instrumentation is illustrated in figure 4. Signals from the five microbarographs and the anemometer are hardwired into the recording trailer where they are amplified and filtered. These signals are recorded simultaneously in analog format on 16mm develocorder film and in digital format at a sample rate of two samples per second on a Kinometrics 43419 digital recording system. The signals from the three-component KS-36000 seismograph also are hardwired into the recording trailer. There, they are split and separately filtered into a long-period and intermediate-period analog format. These seismic data are recorded on the 16mm develocorder film and added to the digital data string. Thus, with this data collection system, simultaneous well-calibrated, well-timed data from a collocated, standard microbarograph array and three-component, long-period, borehole seismograph were obtained for analysis.

The unity-gain displacement amplitude responses as a function of frequency for the seismograph and microbarograph systems are illustrated in figure 5. The microbarographs characteristically have flat responses for barometric pressure changes with periods between 2.5 hertz and 0.06 hertz. The attenuation for frequencies higher than 2.5 hertz is 36 dB/octave, and is 6 dB/octave for frequencies less than 0.06 hertz. The seismographs, on the other hand, have a peak response at 0.033 hertz and attenuate at 18 dB/octave for ground displacement frequencies either greater than or less than 0.033 hertz. Because the response curves of the microbarographs and seismographs are so different, post-recording filter processing is necessary before visual comparison can be meaningful.

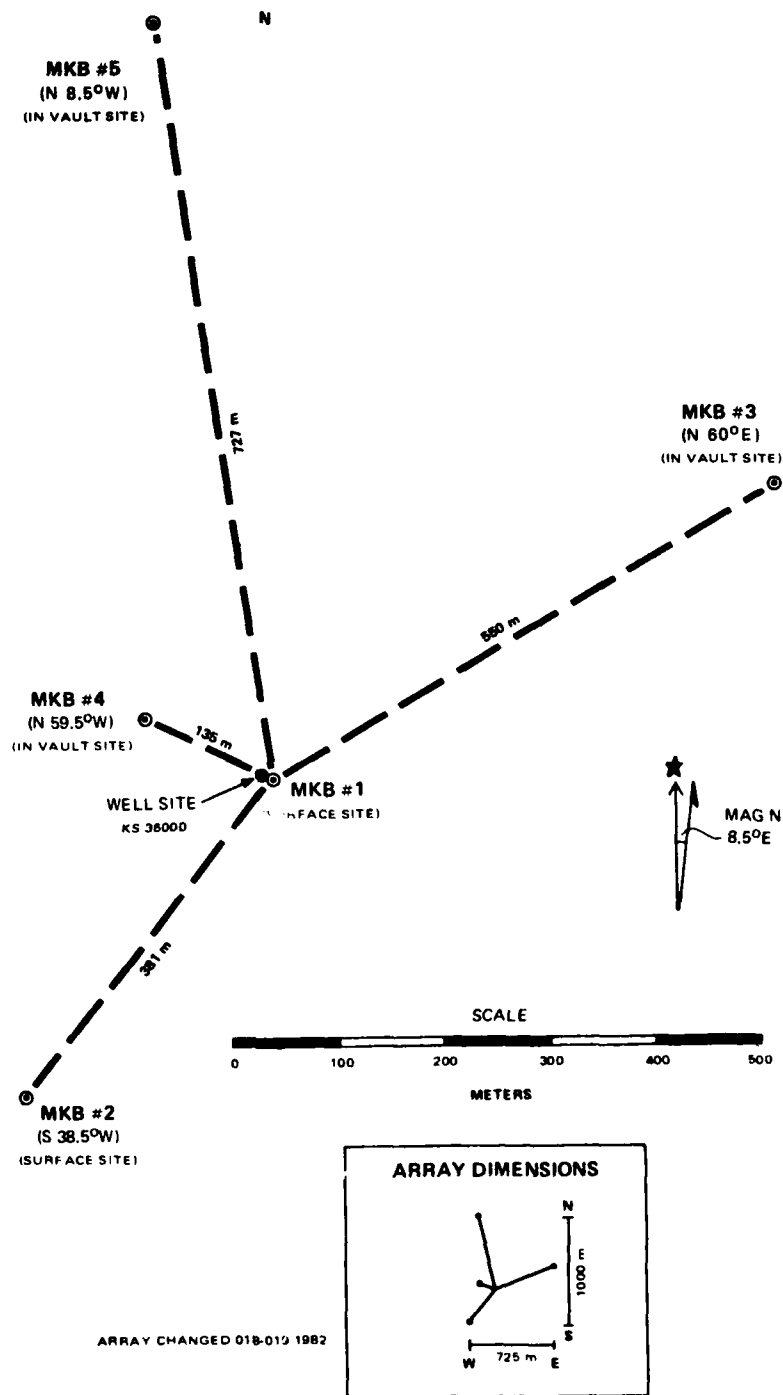


FIGURE 3. MCKINNEY, TEXAS MICROBAROGRAPH/SEISMOGRAPH EXPERIMENT LAYOUT

G 12929

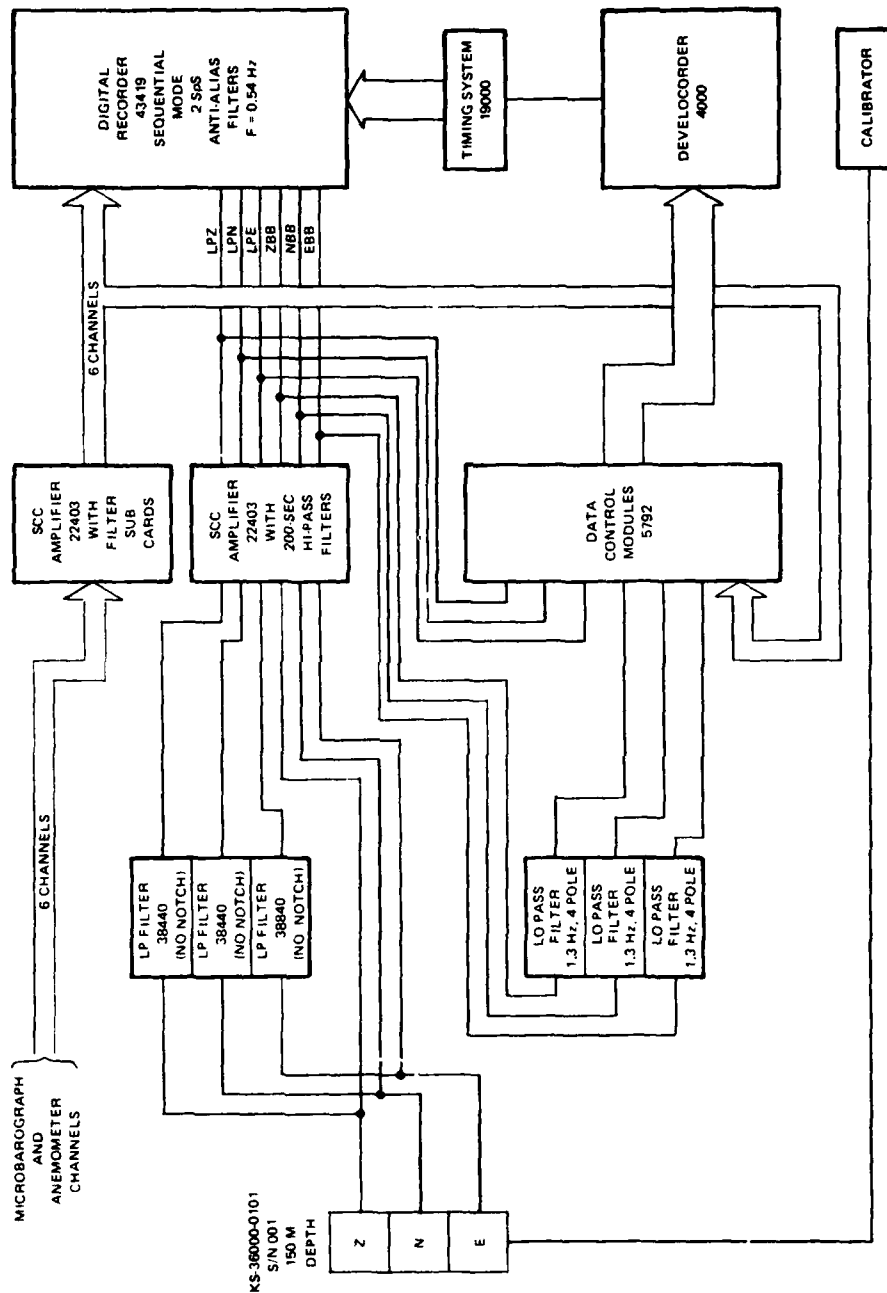


FIGURE 4. SEISMIC AND RECORDING SUBSYSTEMS - MCKINNEY INFRASONIC STUDY

G12347

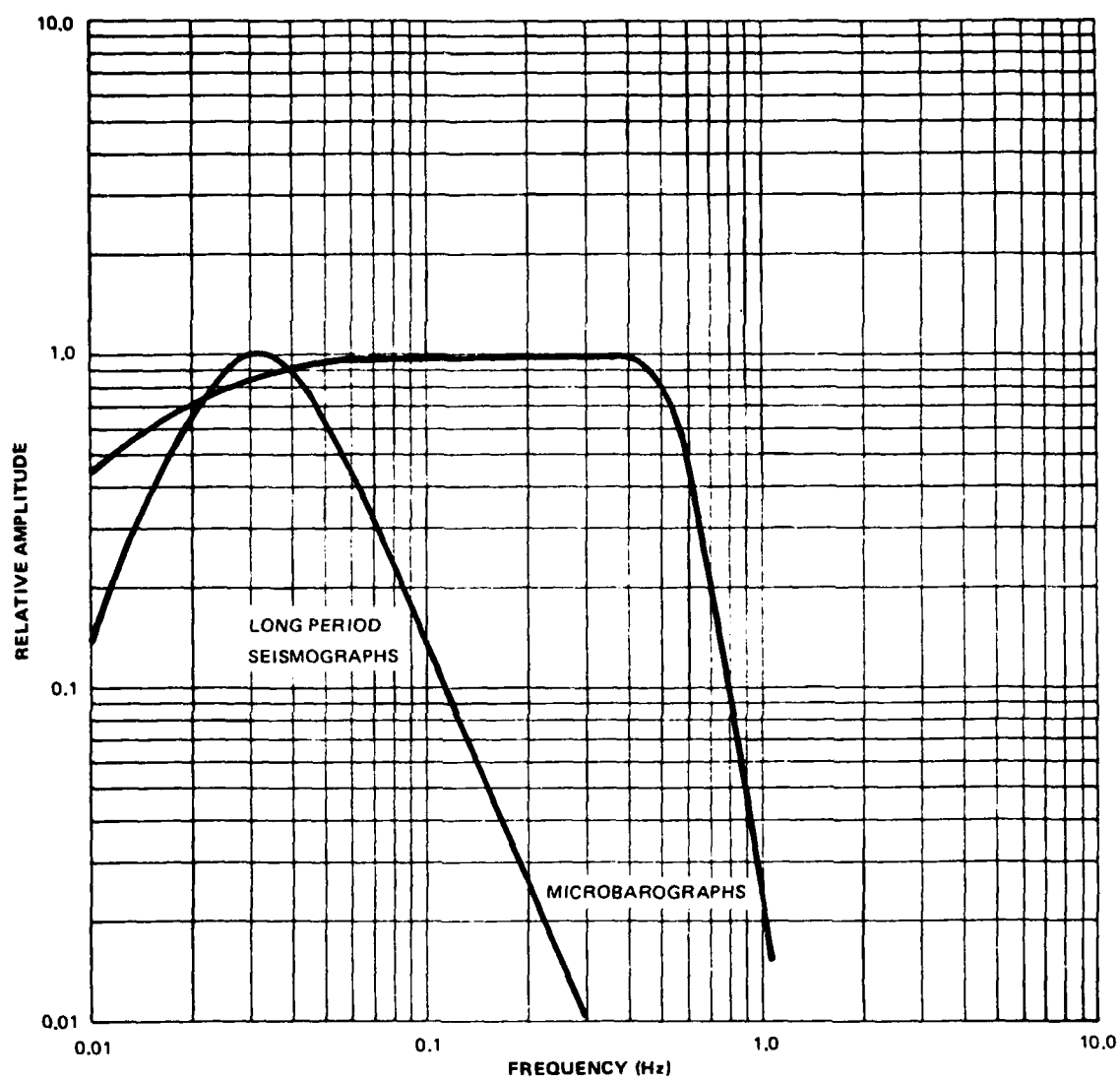


FIGURE 5. RELATIVE RESPONSES OF SEISMOGRAPH CHANNELS TO DISPLACEMENT AND MICRO-BAROGRAPH CHANNELS TO PRESSURE

2.3 EVALUATION OF AMBIENT NOISE FIELDS AND EFFECTS ON INFRASONIC SIGNAL DISCRIMINATION

In section 1.3, we suggested (based on previous studies of Sorrells) that the infrasonic signal discrimination problem may be more easily approached using seismic rather than microbarometric data because the passive wavelength filter properties of the earth permit enhanced infrasonic signal-to-wind noise ratios using seismic data. This would be the case if all of the noise observed seismically were of local barometric origin. In actuality, however, the seismic noise field has components which are correlated with local barometric noise and components which are uncorrelated with the local barometric noise field. Thus, determination of actual signal-to-noise ratio (SNR) enhancement requires power spectral analyses of the two pure noise fields, investigation of the degree of coherence of the noise fields, and an understanding of the earth response transfer function.

The principal contribution to the microbarometric noise field is wind-generated pressure variations. Thus, it is necessary to study the microbarometric noise field under a variety of wind conditions. Further, correlation studies of random wind noise on microbarographs and seismographs require both data segments to be uncontaminated by infrasonic signals or seismic signals from earthquakes. In addition, the data segments must be of adequate length to ensure proper spectral and coherence estimations via available computer techniques. Finally, there must be sufficient numbers of samples to be a statistically meaningful set. In practice, samples meeting all of the above criteria are surprisingly difficult to obtain.

The sample selection procedure we followed was first to examine the analog develocorder film for time segments which were visually uncontaminated by obvious infrasonic or seismic signals. The transit time across the microbarograph array could be used relatively successfully to screen out microbarometric record segments with signals traveling at approximately 300 m/sec. Once a data segment was selected from the analog records, the corresponding time period on the digital tape was isolated in a computer file. The digital data then were plotted to ensure that the digital sample segment corresponded to the chosen analog data and was free of undesirable defects such as glitches or data digitization errors. Power spectra, corrected for calibrated instrument response, then were computed from the time series data via a conventional Fourier analysis technique. The spectra were examined for obvious signal contamination effects and were discarded if contamination was suspected. Following this procedure, although laborious, yielded a suite of uncontaminated noise samples which covered a wide variation of wind velocities.

Two typical microbarometric noise power spectra are illustrated in figure 6. One corresponds to a mean wind velocity of approximately one mile per hour and illustrates spectral characteristics under low wind conditions. The other spectrum illustrated is for a time period of moderate wind conditions. Comparing these two noise spectra illustrates several interesting characteristics of the barometric noise field. The low wind condition power spectrum decreases relatively constantly as the frequency increases at a rate of approximately 25 dB/decade for the frequency range from 0.008 hertz to 1.0 hertz. The spectrum is generally featureless indicating little preference

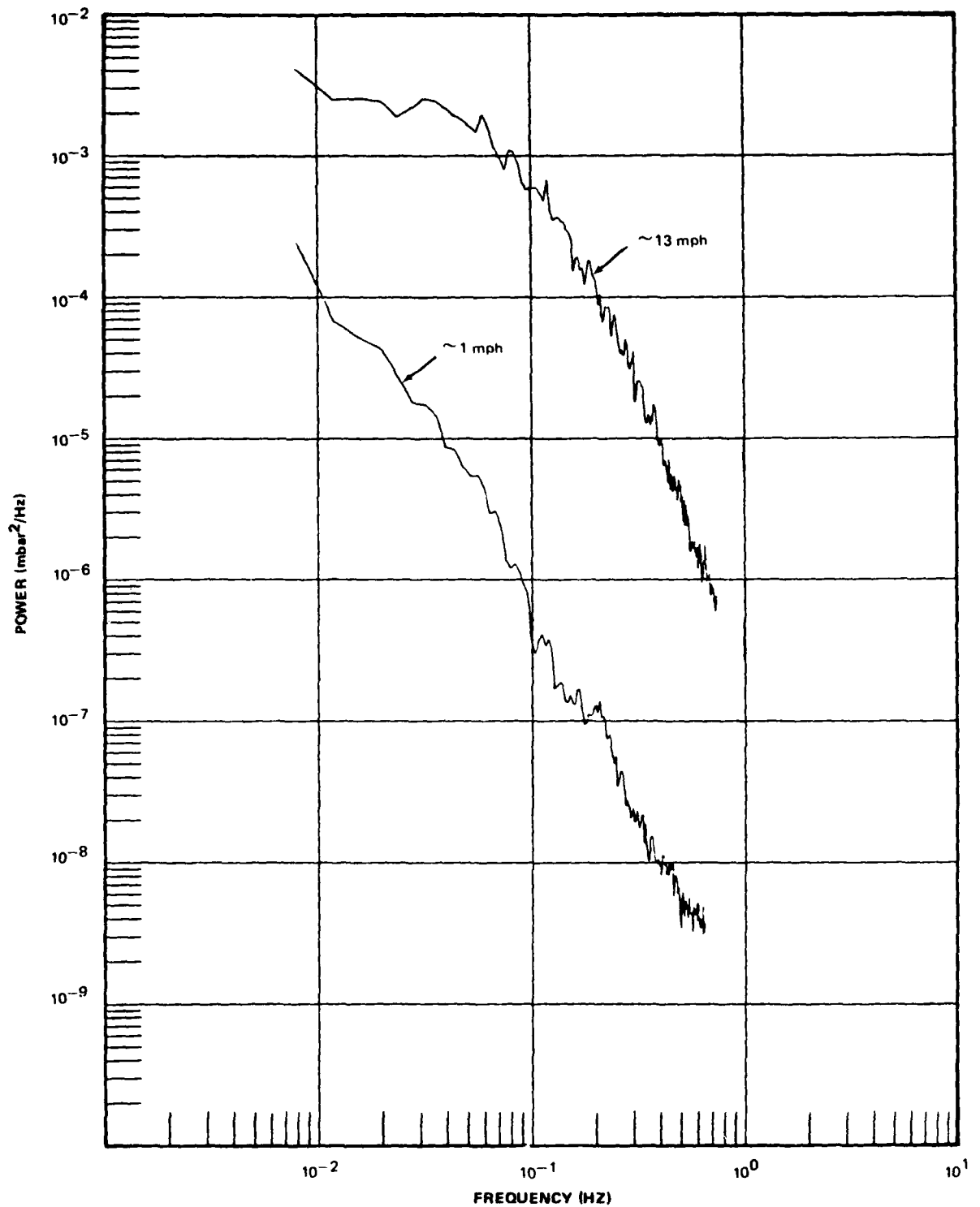


FIGURE 6. POWER SPECTRAL DENSITIES OF CALIBRATED MICROBAROMETRIC DATA CORRECTED FOR INSTRUMENT RESPONSE (MKB NO. 1) FOR TWO WIND CONDITIONS

G 12970

for convection cells of a specific dimension. The spectrum for the thirteen miles-per-hour wind condition, on the other hand, displays a continuously variable attenuation gradient over the frequency range 0.008 hertz to 1.0 hertz. The frequencies between 0.008 hertz and .08 hertz display power attenuation as a function of increasing frequency of approximately 3 db/octave, whereas the frequencies higher than 0.2 hertz have an attenuation rate of at least 24 dB/octave. Thus, as the velocity of the wind increases, not only is there an increase in the integrated RMS barometric noise power level, but there is also a trend to excite preferentially the lower frequencies more dominantly than the higher frequencies. Unfortunately, the infrasonic-acoustic signals to be discriminated also lie in the spectral band with periods greater than ten seconds. Therefore, as the wind velocity increases from low to moderate conditions, the ability to discriminate low-amplitude infrasonic signals from the ambient barometric noise significantly degrades. Furthermore, the degradation is a nonlinear function of increasing wind velocity.

The displacement power spectra (corrected for instrument response) in nanometers²/hertz for the three components (vertical, north-south, and east-west) of the seismic noise field contemporaneous with the periods of low and moderate wind conditions illustrated in figure 6 are illustrated in figures 7 (vertical) 8 (north-south), and 9 (east-west). Comparing figures 6 and 7, for example, illustrates that the seismic noise field in the frequency band from 0.008 hertz through 0.3 hertz is actually dominated by noise which is uncorrelated with the local microbarometric noise field. In fact, only at frequencies less than 0.02 hertz ($T = 50$ sec) is there a significant correspondence between the microbarometric and the vertical seismic noise fields. Comparing figures 7, 8, and 9, it is obvious that the horizontal seismometers are affected more dramatically by increasing wind velocity than is the vertical seismometer. In section 2.4.2, it will be shown that there is also a corresponding apparent increased sensitivity of the horizontal seismometers to infrasonic signals than would be predicted theoretically. The reason for this phenomenon is under continued investigation. To demonstrate the coherence of the two noise fields in a more robust manner, ordinary coherences between the microbarometric data and the three orthogonal components of the seismic data were computed. Figures 10 and 11 illustrate these coherences under low and moderate wind conditions, respectively. Under low wind conditions, there is little coherence between the microbarometric noise field and any of the components of the seismic noise field. There is a higher degree of coherence with the horizontal components (figures 10 b and c) than with the vertical component (figure 10a). This apparent lack of correlation may itself be erroneous because the background digital RMS count and variance for these low wind conditions are very small. Thus, rather than reflecting true independence of the microbarometric and seismic noise fields, this figure may only be a measure of the correlation of the random system noise with superimposed, extremely low resolution data. The coherences exhibited by the moderate wind condition of figure 11 are more definitive. For these analyses, the digital RMS count was sufficiently large to ensure that it was well above the system noise level. In this case, the microbarometric and vertical mode seismic noise is relatively incoherent. The horizontal mode seismic noise, on the other hand, exhibits high correlation with the microbarometric noise in two frequency

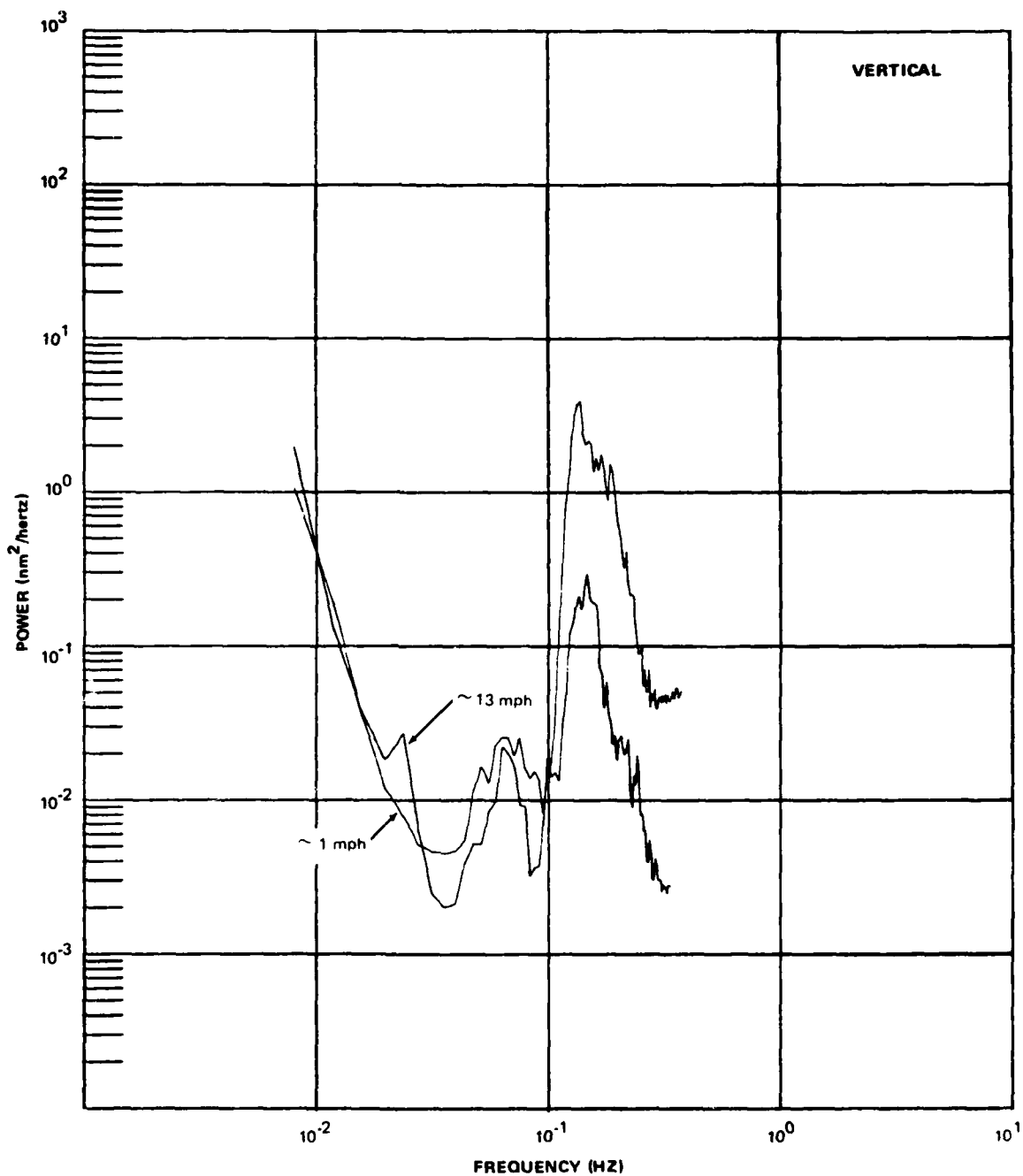


FIGURE 7. POWER SPECTRAL DENSITIES OF CALIBRATED VERTICAL SEISMIC DATA CORRECTED FOR INSTRUMENT RESPONSE DURING TWO WIND CONDITIONS

G 12971

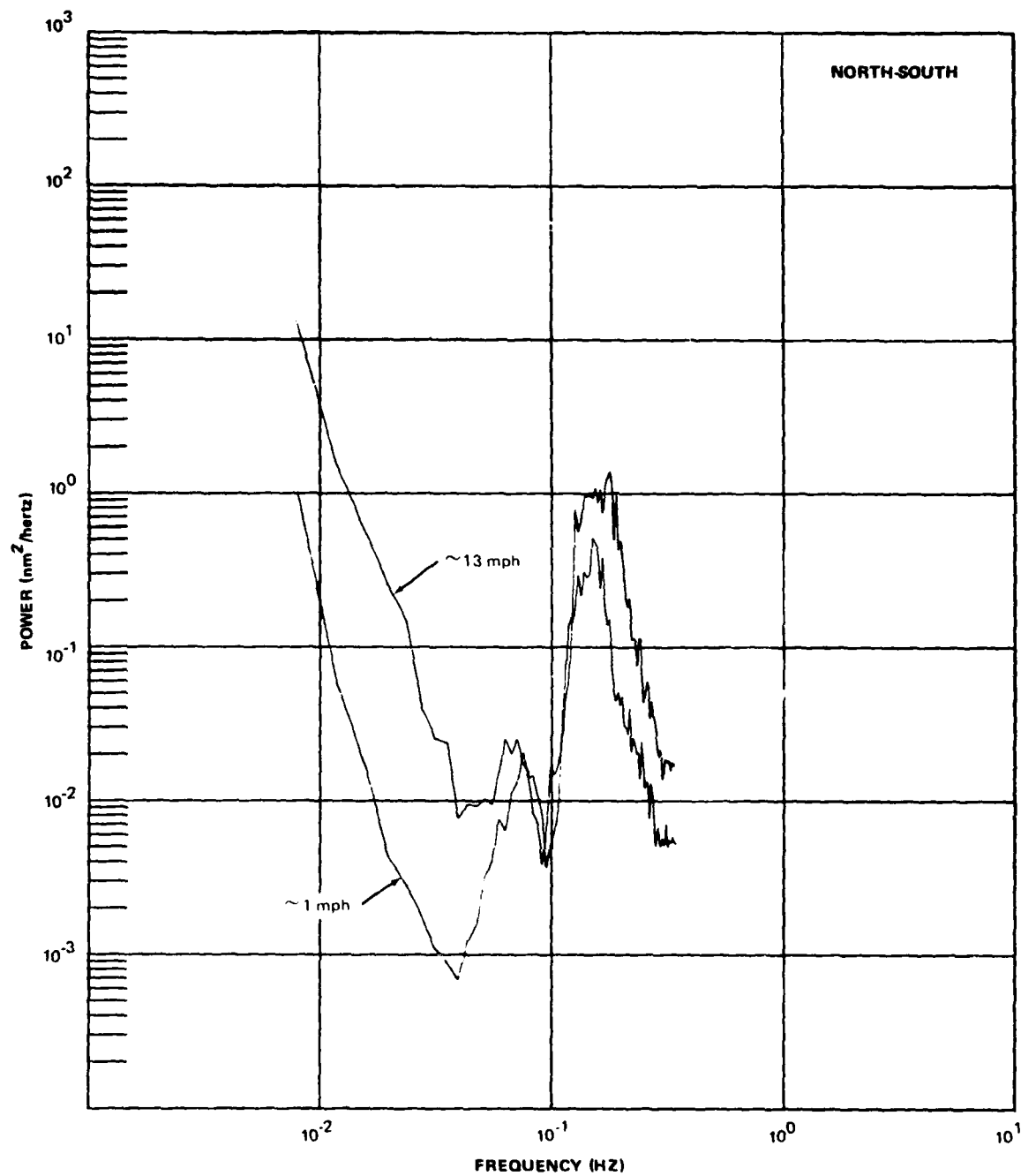


FIGURE 8. POWER SPECTRAL DENSITIES OF CALIBRATED NORTH-SOUTH SEISMIC DATA CORRECTED FOR INSTRUMENT RESPONSE DURING TWO WIND CONDITIONS

G 12972

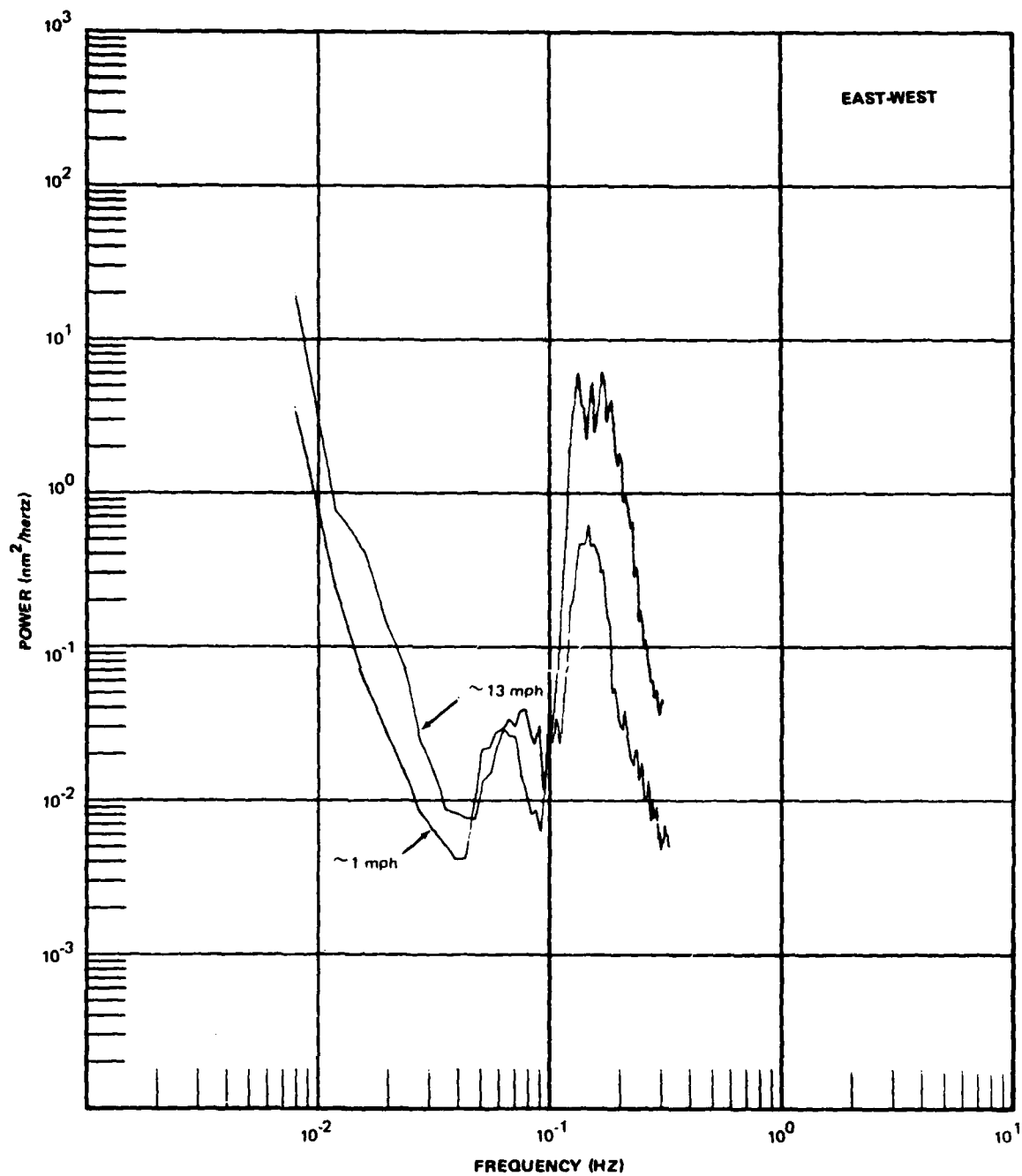


FIGURE 9. POWER SPECTRAL DENSITIES OF CALIBRATED EAST-WEST SEISMIC DATA CORRECTED FOR INSTRUMENT RESPONSE DURING TWO WIND CONDITIONS

G 12973

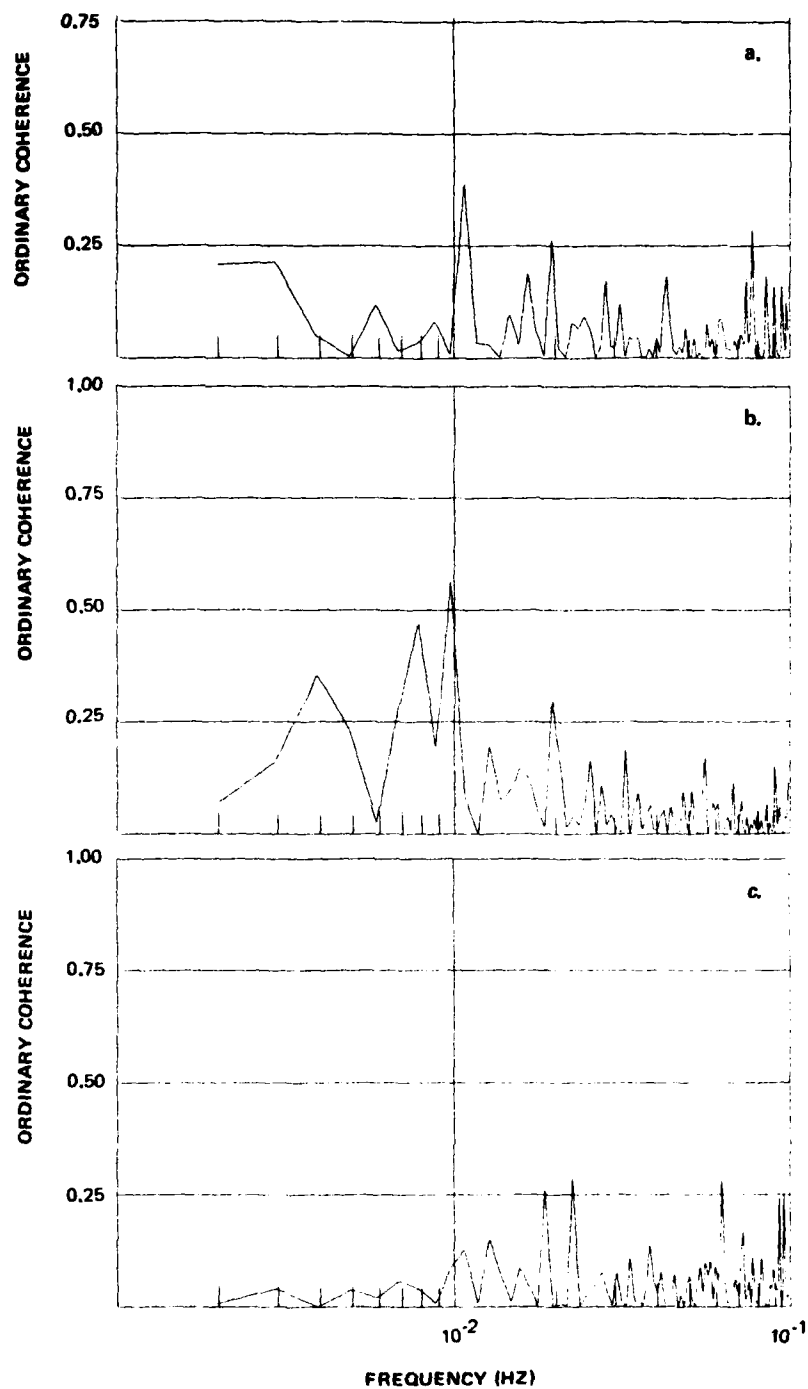


FIGURE 10. ORDINARY COHERENCE ESTIMATES BETWEEN MICROBAROMETRIC AND SEISMIC NOISE FIELDS UNDER LOW WIND CONDITIONS. (a) MICROBAROMETRIC AND VERTICAL SEISMIC COMPONENT (b) MICROBAROMETRIC AND NORTH-SOUTH SEISMIC COMPONENT. (c) MICROBAROMETRIC AND EAST-WEST SEISMIC COMPONENT.

G 12974

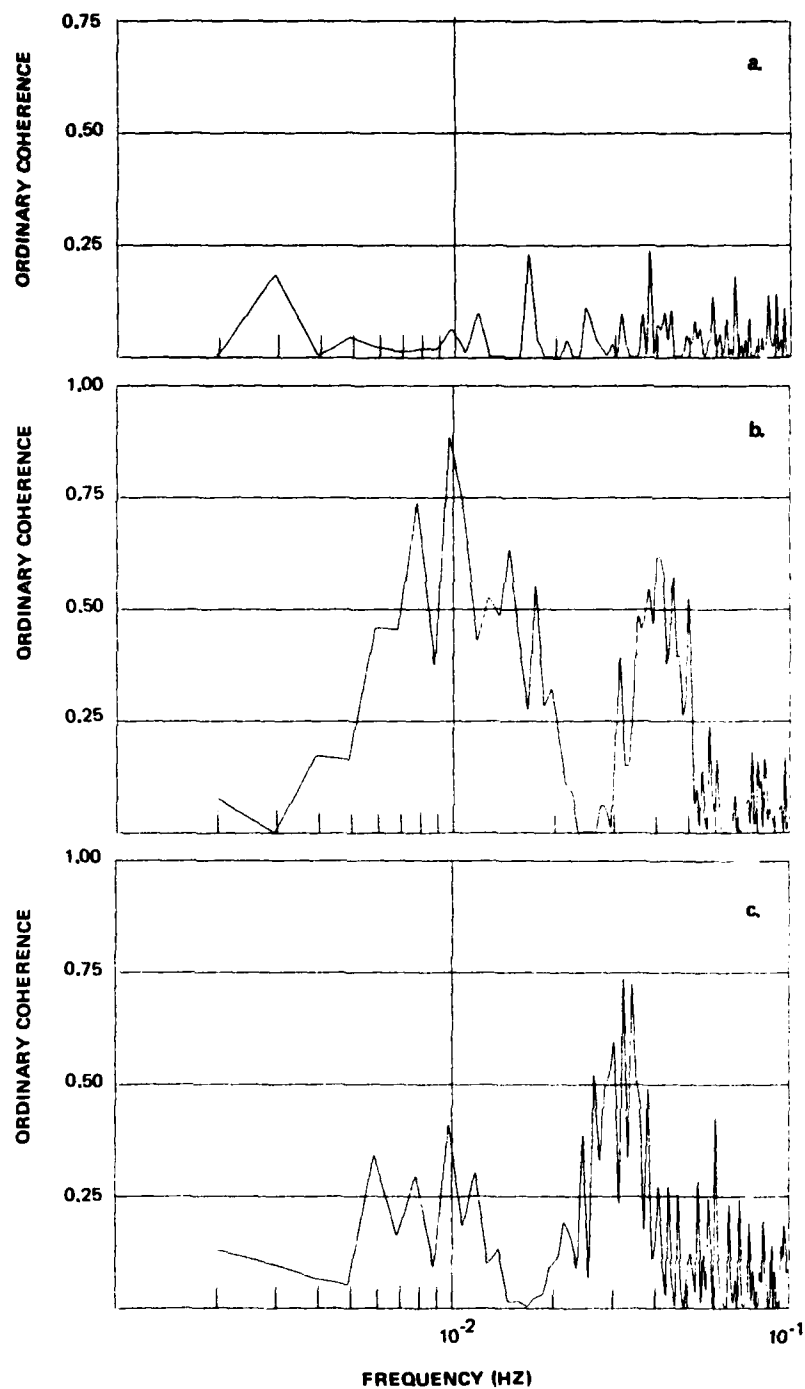


FIGURE 11. ORDINARY COHERENCE ESTIMATES BETWEEN MICROBAROMETRIC AND SEISMIC NOISE FIELDS UNDER MODERATE WIND CONDITIONS. (a) MICROBAROMETRIC AND VERTICAL SEISMIC COMPONENT (b) MICROBAROMETRIC AND NORTH-SOUTH SEISMIC COMPONENT. (c) MICROBAROMETRIC AND EAST-WEST SEISMIC COMPONENT.

bands; 0.006 hertz to 0.018 hertz and 0.035 hertz to 0.05 hertz. These correlations clearly illustrate that the long-period, horizontal seismic noise field is dominated by local microbarometric fluctuations. Furthermore, these noise fields are composed of preferred convection cell dimensions for given wind conditions and are definitely non-white in character.

Having examined the characteristics of the microbarometric and seismic noise fields, we shall next quantitatively assess the limiting nature of the SNR for detection of infrasonic signals using seismic data. Following the method of Sorrells (1981) which is detailed in appendix A, the infrasonic SNR observed on the seismogram recorded by a long-period, vertical seismograph installed at moderately shallow depths, relative to that observed on a microbarogram recorded on the surface, is given by

$$\frac{SNR_z}{SNR_m} = |G_z(f)|^2 \frac{|N_z(f)|^2}{|N_m(f)|^2} \quad (1)$$

where SNR_z and SNR_m are the vertical seismic and microbarometric infrasonic SNR's, $|N_z(f)|^2$ and $|N_m(f)|^2$ are the estimated power spectra of the vertical seismic noise and the microbarometric noise corrected for instrument responses, and $G_z(f)$ is the transfer function relating infrasonic atmospheric pressure variations to vertical earth movements. $G_z(f)$ can be calculated if the local distribution of elastic constants is approximated (Sorrells and Goforth, 1973), or, alternatively, it can be measured experimentally. The theoretical vertical and horizontal transfer functions computed for McKinney, Texas, using a seventeen-layer earth model are illustrated in figure 12. Utilizing the theoretical vertical transfer function illustrated with the observed low and moderate wind condition microbarometric and vertical seismic noise fields, we shall next examine the relative infrasonic signal detection capabilities from vertical seismic versus microbarometric data.

A quantity useful in the comparison of SNR gain of the vertical seismogram to the microbarogram is I_{zm} , which measures the difference between the infrasonic SNR observed on a vertical seismogram and on a microbarogram expressed in dB. I_{zm} is defined as,

$$I_{zm} = 10 \cdot \log_{10} \left(\frac{SNR_z}{SNR_m} \right)$$

Estimated values of I_{zm} for low and moderate wind conditions as a function of frequency are shown in figure 13. During times characterized by low wind conditions, the microbarograph has a superior SNR throughout the spectral band from 0.005 to 0.5 hertz except for a small window from 0.015 hertz through 0.033 hertz where the vertical seismograph is moderately better. During times of moderate wind conditions, however, the SNR of the vertical seismometer is significantly better than that of the microbarograph. Several important spectral limit points are worth noting on the moderate wind condition curve illustrated in figure 13. The 0 dB points are at wave periods of 143 seconds and 9 seconds respectively. Infrasonic waves with periods between these limits will be recorded better with the vertical seismometer

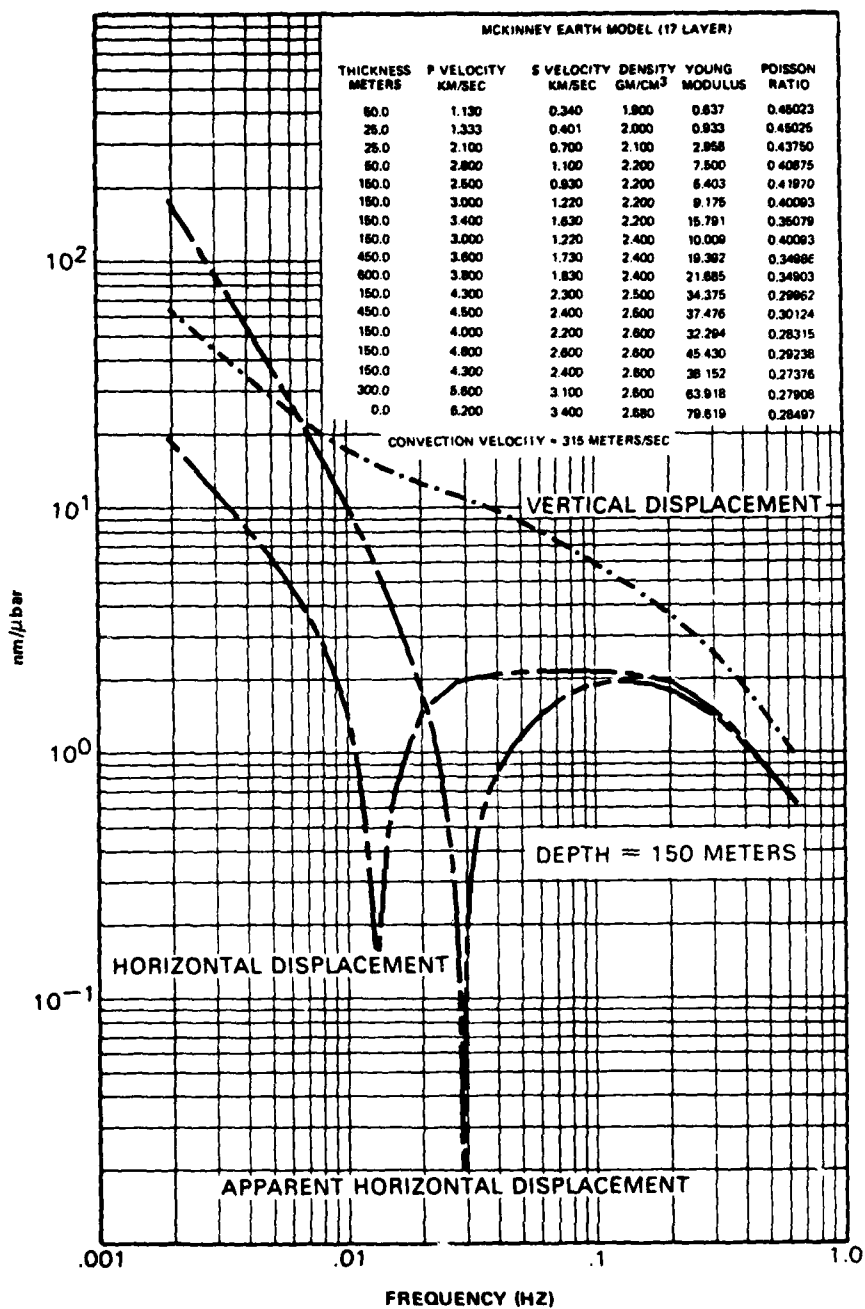


FIGURE 12. THEORETICAL RESPONSE OF AN ELASTIC LAYERED HALF SPACE TO ATMOSPHERIC LOADING

G 12349

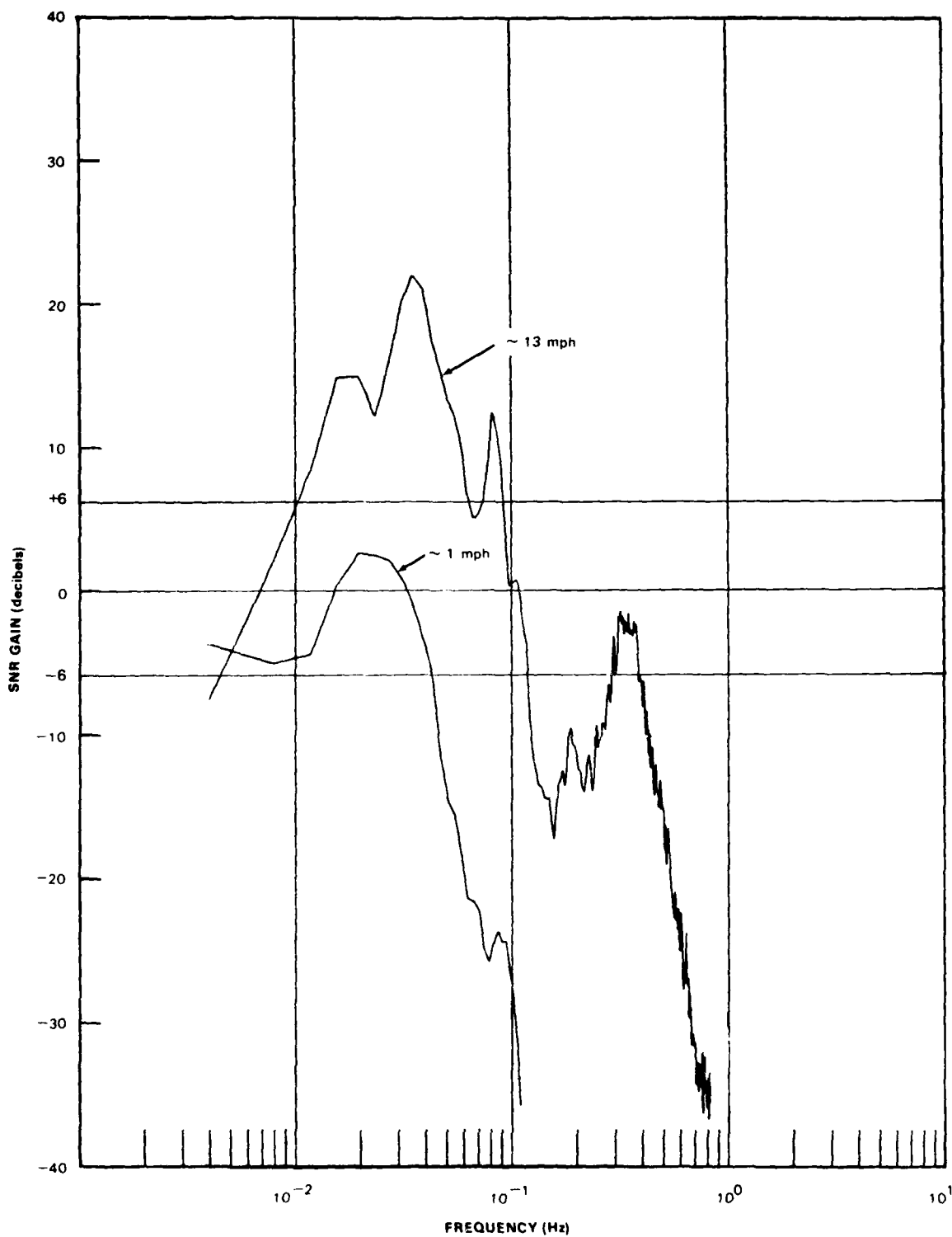


FIGURE 13. THE DIFFERENCE BETWEEN SIGNAL-TO-NOISE RATIOS OF VERTICAL SEISMIC AND MICROBAROMETRIC DATA UNDER LOW AND MODERATE WIND CONDITIONS

G 12910

than the microbarograph. Outside these limits, the microbarograph remains the instrument with the better SNR. The ± 6 dB points are at wave periods between 100 seconds and 11 seconds. For this spectral band, the vertical seismometer has a SNR at least twice that of the microbarograph under moderate wind conditions. The notches in the moderate wind condition SNR gain curve are obviously related to the well-known microseismic noise bands. Since this curve was developed from one empirical data set, the significances of these notches to the SNR gain curve must be considered variable. At times of high microseismic storms, the SNR gains for infrasonic signals are undoubtedly degraded significantly. It is worth noting, however, that the time periods of both the low and moderate wind condition records are times when microseisms were moderately high; thus, the curves illustrated in figure 13 can be considered as relatively mean rather than optimum conditions.

The previous SNR analysis was dependent upon a theoretical transfer function for earth response. Before discussing observed signals, we will compare the theoretical and empirically derived earth response functions. The method used to obtain the experimentally derived values for $G_z(f)$ is outlined in appendix B. The methodology for horizontal components is similar and is not given. Comparison of the theoretical and observed vertical component transfer functions for McKinney, Texas, is illustrated in figure 14. The extremely small residual between the observed and predicted vertical-component earth response functions indicates that the computed values of $G_z(f)$ may be used with a high degree of confidence in estimating the ratio SNR_z/SNR_m .

Unlike the vertical-component earth response transfer function, the theoretical and observed horizontal component earth response transfer functions have relatively large residuals. This is apparent in figure 15 which is a comparative plot of theoretical and observed horizontal transfer functions from signals produced by explosions of El Chichon volcano. The theoretical calculations consistently underestimate the amplitude of the observed horizontal displacements as a function of frequency by a factor of at least three. The exact reason for this departure of theory from what is observed is not clear. One explanation may be that there are significant anisotropic differences between the vertical and horizontal component elastic parameters. This explanation is relatively unsatisfying, however, because it requires the differences in the elastic parameters to be unreasonably large to account for the observed differences. An alternative explanation may be that one or more of the assumptions in the calculation of theoretical displacements is incorrect and that a significant contribution to the total horizontal displacement field is being made by a component assumed to have insignificant contribution. Considering that all of the observed infrasonic signals were from one source at one azimuth, it is also possible that the differences between theoretical and observed curves may be azimuth dependent. Further analysis is obviously required to definitely state the reason for this departure of theory and observation.

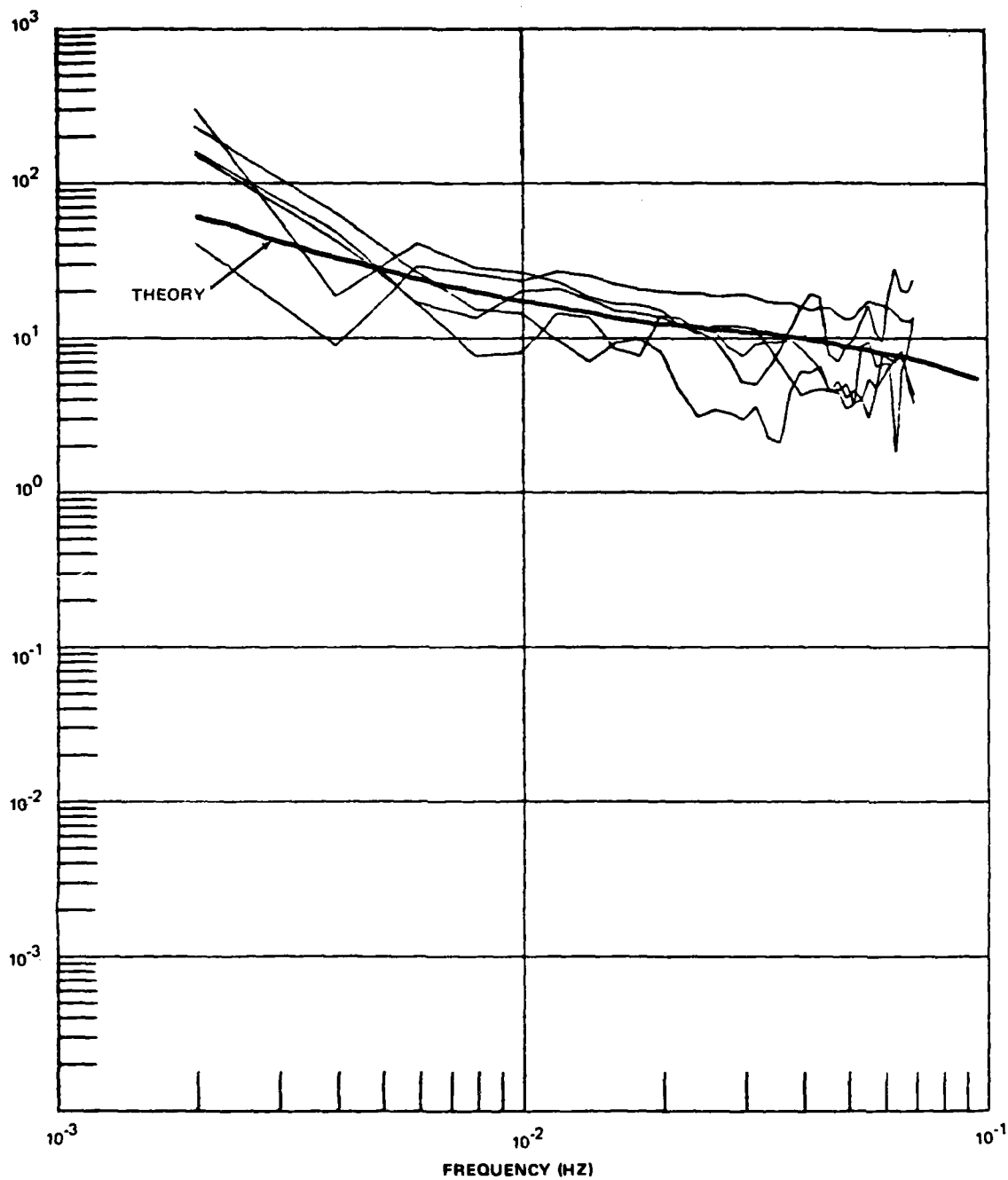


FIGURE 14. COMPARISON OF OBSERVED AND CALCULATED VERTICAL DISPLACEMENT EARTH RESPONSE FUNCTIONS FOR AN INFRASONIC SIGNAL. THE DATA SHOWN ARE APPROPRIATE FOR OBSERVATIONS MADE AT A DEPTH OF 150 METERS AT MCKINNEY, TEXAS.

G 12976

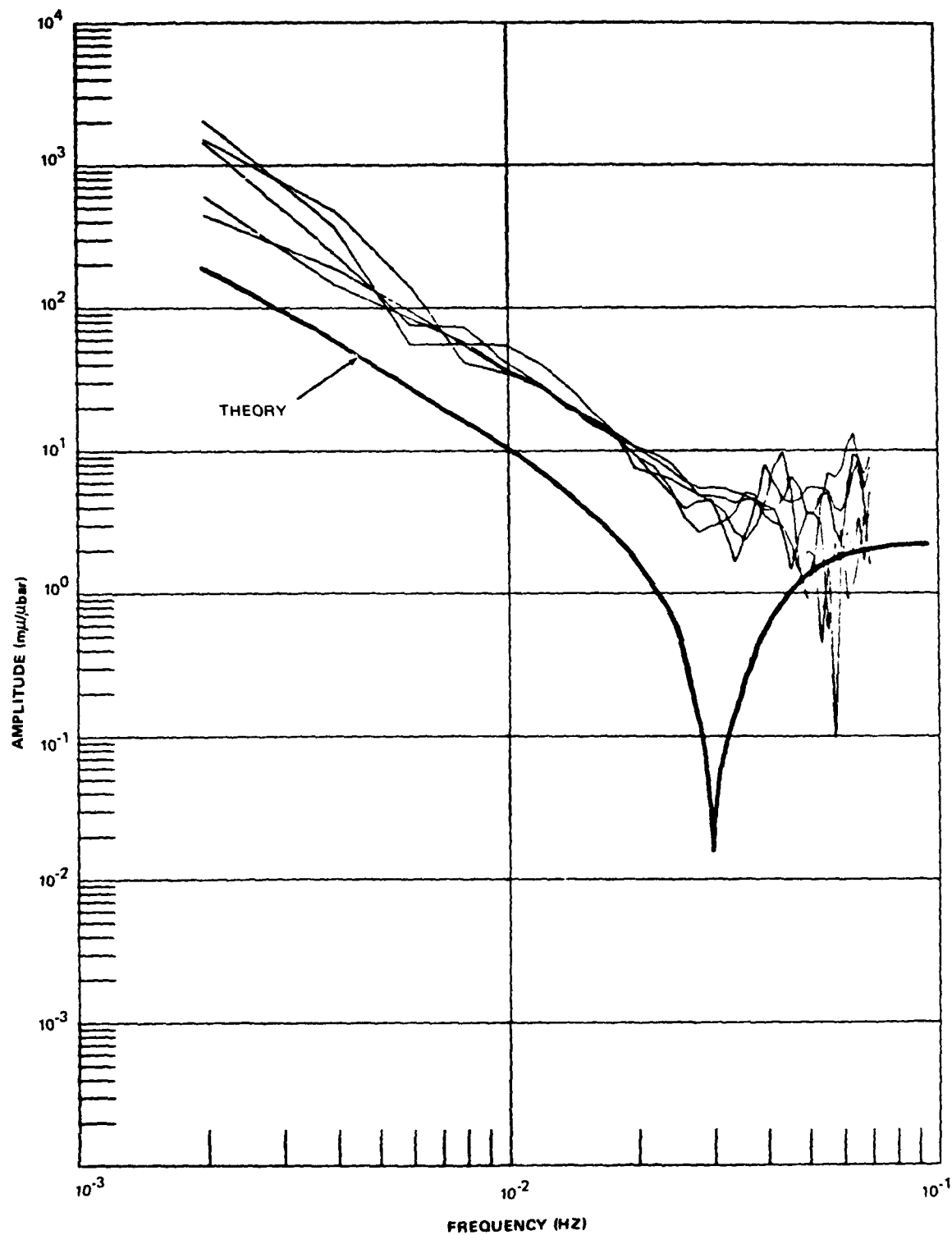


FIGURE 15. COMPARISON OF OBSERVED AND CALCULATED NORTH-SOUTH HORIZONTAL DISPLACEMENT EARTH RESPONSE FUNCTIONS FOR INFRASONIC SIGNALS. THE DATA SHOWN ARE APPROPRIATE FOR OBSERVATIONS MADE AT A DEPTH OF 150 METERS AT MCKINNEY, TEXAS.

2.4 COMPARATIVE ANALYSIS OF RECORDED INFRASONIC SIGNALS

2.4.1 The eruption sequence of El Chichon volcano 29 March - 6 April 1982

The most-significant infrasonic signals to be recorded during the data collection phase of this research program were produced by a sequence of explosive eruptions of El Chichon volcano in southern Mexico. This eruptive sequence provided an excellent opportunity to record and analyze the infrasonic signatures of explosion-like sources. In addition, individual events in the sequence had energy releases which varied over several orders of magnitude. Thus, these events also provided the opportunity to estimate the approximate yield threshold for discrimination of seismically recorded infrasonic signals from atmospheric detonations.

The El Chichon volcanic complex is located at 17.33°N, 93.20°W in the state of Chiapas, Mexico. The principal volcano is approximately 700 km southeast of Mexico City and 16.16° (1797 km) south of the McKinney, Texas, experimental recording site. The elevation of the central vent is 1350 meters above sea level. A NOAA weather satellite infrared image (see figure 16) produced on 29 March at 0730 UCT (universal coordinated time) clearly illustrates the extent of the initial eruption cloud two hours after the eruption began. The location is indicated on figure 16 by the white arrow.

Prior to the eruption sequence which began abruptly on 29 March 1982, there were no records of previous activity. Information about the eruption sequence which continued from 29 March through 6 April 1982 has been published in the SEAN Bulletins of the Smithsonian Institution. To ensure that this information is available with this technical report, we have included the El Chichon reports from SEAN Bulletin, volume 7, numbers 3, 4, 5, and 6 as appendix C. Origin times of five identifiable eruption phases, extracted from the SEAN reports, are listed in table 1. The Volcanic Explosivity Index (VEI) number assigned by the Smithsonian Institution (Tom Simkin, personal communication) is also included in table 1. Criteria used to estimate the VEI are listed in table 2 from Newhall and Self (1982). The events listed in table 1 yielded infrasonic signals which were discriminated easily on the developocorder film records. These are the initial events on Julian date 088, the two events on 093, and the two events on 094. Time frames of the digital data corresponding to these developocorder film locations then were isolated and processed further.

The signals from the five microbarographs were delayed appropriately and summed to create an array beam for the location of MKB#1 oriented at an azimuth of 168° (the great circle back azimuth from McKinney, Texas, to El Chichon). These array beam microbarographs for the five events are illustrated on figures 18-32 as red lines. Because the spatial dimensions of the array were not significantly different from the ambient wind convection cell dimensions at low frequencies, the noise reduction potential of beam-forming was not optimized. The beam forming procedure did improve the higher frequency resolution of the microbarograph data, however, and, therefore, is considered to be justifiable.

Processing of the seismic data was also relatively simple. Because the raw, long-period data were dominated by six-second microseismic noise, it was

↑ 07:30 29MR82 17A-Z 0006-1640 FULL DISC IR

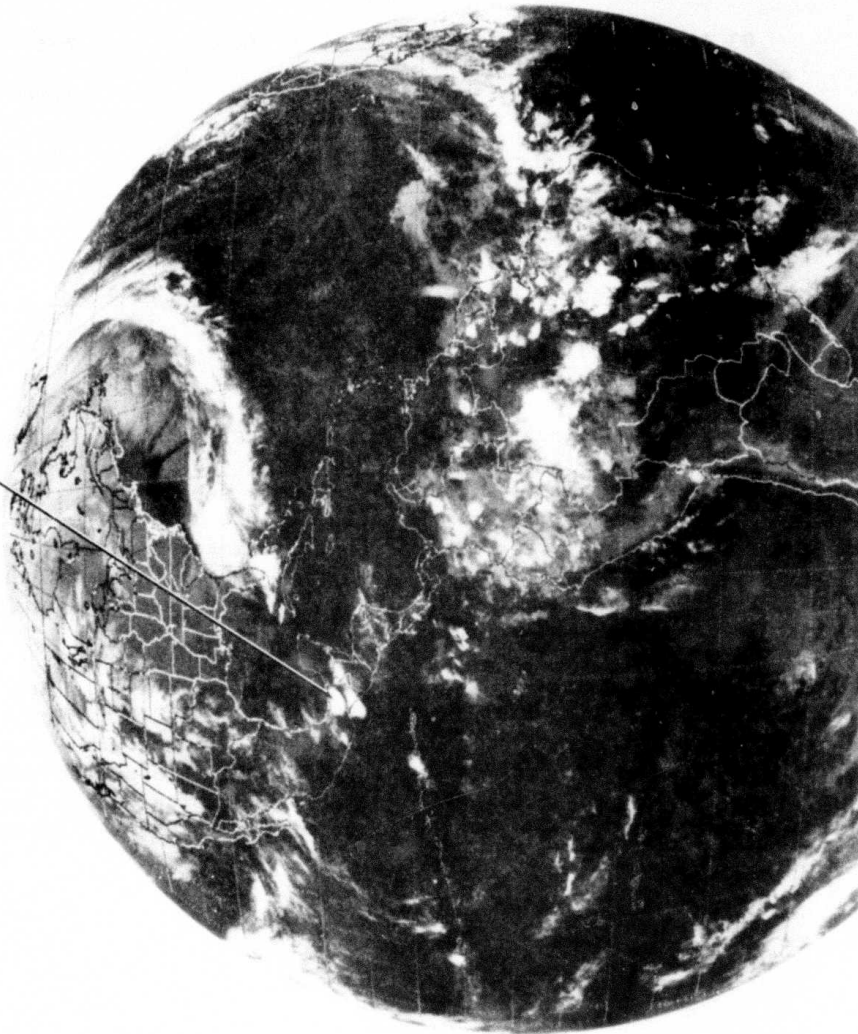


FIGURE 16. NOAA SATELLITE INFRARED IMAGE OF THE EL CHICHON ERUPTION 29 MARCH 1982. THIS IMAGE WAS TAKEN APPROXIMATELY TWO HOURS AFTER THE INITIATION OF THE ERUPTION.

P21053

TABLE 1. ORIGIN TIMES OF TEN IDENTIFIABLE ERUPTION PHASES

<u>Date</u>	<u>Julian date</u>	<u>Time (UCT)</u>	<u>VEI</u>
29 March 1982	088	05:32	4
03 April 1982	093	08:50	2-3†
03 April 1982	093	09:12	2-3†
04 April 1982	094	02:00	U
04 April 1982	094	11:22	4

† Estimation by Mauk

U Unassigned VEI

necessary to apply a low-pass filter to the digital data to improve the signal-to-noise ratio in the infrasonic signal frequency band. We applied a low-pass filter with corner at 0.0417 hertz ($T=24$ seconds) and high-frequency roll off of 24 dB/octave (-4) to all seismic data. The effect of this filter on the displacement response of the seismometer is illustrated in figure 17. The filtered horizontal seismograms were rotated computationally from a NS, EW orthogonal pair to a radial and transverse orthogonal pair oriented at 168° and 78° respectively.

The filtered, vertical seismograms for each of the five events are illustrated as black lines on figures 18, 21, 24, 27 and 30. The filtered, radial seismograms for each of the five events are illustrated as black lines on figures 19, 22, 25, 28, and 31, and the filtered, transverse seismograms are on figures 20, 23, 26, 29, and 32. An ambient noise sample having wind conditions equivalent to those at the times of the El Chichon infrasonic

TABLE 2. CRITERIA FOR ESTIMATION OF THE VOLCANIC EXPLOSIVITY INDEX (VEI) [FROM NEWHALL AND SELF (1982)]

CRITERIA	VEI:	0	1	2	3	4	5	6	7	8
DESCRIPTION		NON-EXPLOSIVE	SMALL	MODERATE	MOD-LARGE	LARGE	VERY LARGE			
VOLUME OF EJECTA (M ³)		10 ⁴	10 ⁴ -10 ⁶	10 ⁶ -10 ⁷	10 ⁷ -10 ⁸	10 ⁸ -10 ⁹	10 ⁹ -10 ¹⁰	10 ¹⁰ -10 ¹¹	10 ¹¹ -10 ¹²	>10 ¹²
(TSUYA CLASSIFICATION)		(I)	(II-III)	(IV)	(V)	(VI)	(VII)	(VIII)	(IX)	
COLUMN HEIGHT (KM)		0.1	0.1-1	1-5	3-15	10-25	>25			
QUALITATIVE DESCRIPTION		-- GENTLE EFFUSIVE --		---- "EXPLOSIVE" ----				"CATACLYSMIC, PAROXYSMAL, COLOSSAL"		
								"SEVERE, VIOLENT, TERRIFIC"		
CLASSIFICATION			---- STROMBOLIAN ----							
		---- HAWAIIAN ----		---- "VULCANIAN" ----						
DURATION (HOURS)										
OF CONTINUOUS BLAST										
CAVW MAX EXPLOSIVITY**		-- LAVA FLOWS --		EXPLOSION OR NUÉE ARDENTE						
				PHREATIC						
		-- DOME OR MUDFLOW --								
TROPOSPHERIC INJECTION		NEGLIGIBLE	MINOR	MODERATE	SUBSTANTIAL					
STRATOSPHERIC INJECTION		NONE	NONE	NONE	POSSIBLE	DEFINITE	SIGNIFICANT			

* IF ALL ERUPTIVE PRODUCTS WERE PYROCLASTIC EJECTA
 * FOR VEI'S 0-2 USES KM ABOVE CRATER, FOR VEI'S 3-8 USES KM ABOVE SEA LEVEL
 ** THE MOST EXPLOSIVE ACTIVITY INDICATED FOR THE ERUPTION IN THE CATALOGUE OF ACTIVE VOLCANOES

CRITERIA ARE LISTED IN DECREASING ORDER OF RELIABILITY.

signals was filter-processed in an equivalent manner as the signals for comparison. The horizontal components were not rotated for the noise sample. Plots of the vertical, the north-south and the east-west seismic components are illustrated as black lines on figures 33, 34 and 35 respectively. The contemporaneous microbarogram is illustrated on these figures as a red line. The equivalent displacement amplitude is nanometers for a wave period of thirty seconds is illustrated for the seismograms in figures 18-35 as a vertical black bar. The equivalent pressure amplitude in microbars of the microbarograms at a wave period of fifty seconds is illustrated on the figures as a vertical red bar. To facilitate comparison, figures 18-35 have all been reproduced at the same scale.

Before discussing the quantitative analysis of these data, it is useful to examine some of the qualitative aspects of figures 18-35, since these aspects offer some insight into the potential discrimination capabilities of both the microbarometric and seismic data. First, we will compare the microbarometric signals recorded during a typical background period and those recorded at the arrival times of the A_1 signals from the indicated El Chichon eruption periods. The nomenclature and symbols used to identify infrasonic signals throughout this report have been tabulated at the beginning of the report. Comparing the microbarometric trace of figure 33 with those of figures 18, 21, 24, 27, and 30 clearly demonstrates the complexity of the discrimination problem. The typical random noise on the microbarograph is large and complex. In fact, highly complex signals like those exhibited in figures 18, 27, and 30 could easily be misidentified as a high-level noise if there were not significantly different ambient data surrounding the A_1 train. Observers at El Chichon have reported that the 088 and 094 eruptions were quite complex with repeated injections into the plinian column over periods of thirty to sixty minutes. Thus, the infrasonic acoustic signal could be expected to be similarly complex. On the other hand, the events on 093 were explosive eruptions of short duration without significant repeated injections. The signature of the A_1 wave trains for these events (figures 21, 24) are correspondingly much simpler and, in fact, are more representative of atmospheric nuclear detonations previously reported (Donn and Ewing, 1962; Wexler and Hass, 1962; Bhartendu and Currie, 1963; Harkrider, 1964; Donn and Shaw, 1967). Note that the A_1 signals for the 093 events can be discriminated relatively easily from the ambient background because of the dispersed character of the S_n modes ($0 \leq n < 10$). The overall amplitudes of the signal and noise, however, are nearly equivalent; thus, discrimination is possible only because of the defined complex character of the A_1 wave train as opposed to the relatively random nature of the noise. It is concluded from qualitative examination of the microbarometric data that simple explosive sources can be discriminated relatively easily from the noise even though the signal-to-noise ratio may be 1:1 because of the excitation of dispersed infrasonic acoustic modes. Furthermore, for volcanic explosions, the complexity of the A_1 train is a direct consequence of the complexity of the injections into the plinian column. Therefore, by examining the infrasonic acoustic, A_1 , train at observatories quite distant from a volcanic eruption, a great deal may be learned about the temporal characteristics of the eruption sequence. In addition, by examining the complexity of the A_1 trains produced by erupting volcanoes, it would be possible to separate a suite of simple volcanic explosion signatures of differing energy release with which to compare the yield of atmospheric nuclear detonations.

For brevity, qualitative discussion of the seismically recorded infrasonic signals will be restricted primarily to the El Chichon eruption on 093 with origin time approximately 09:12 UCT (figures 24, 25, 26). Comparing the filtered seismograms (black lines) with the microbarograms (red lines), it is obvious that the low-order atmospheric acoustic modes ($0 < n < 2$) are recorded as well on the seismograph systems as on the microbarographs. Because of the required low-pass filtering to remove the microseismic noise, however, the higher order acoustic mode signals are also lost. Although this loss may not be important in quantification of energy and yield since higher order modes are notorious for displaying significant multipath effects, nevertheless, it does make positive identification of the A_1 train less reliable than with the microbarograph data. If extraction of the higher order modes as well as the low-order modes is significant to the discrimination and yield determination process, alternative filter operators, such as an adaptive prediction error operator, would have to be used to suppress the effects of microseisms. Additional or alternative processing techniques will be discussed further in section 3 of this report.

Further examination of the three-component seismic data from the 093 explosion reveals other interesting aspects of the data which could play important roles in the problems of detection and discrimination of infrasonic-acoustic signals from explosive sources. Some components of the A_1 train, for example, are equivalently prominent on the radial and transverse seismic channels. Thus, the relative horizontal versus vertical signatures of these components could be an aid to extraction of the infrasonic signals from the seismic noise field. Additional insight into this aspect of quantitative signal analysis will be discussed later. Another feature of the seismic data which may assist in the discrimination of the infrasonic signals is the presence of typical seismic surface waves appropriately preceding the A_1 train. For example, Rayleigh wave arrivals are apparent at the beginning of figures 24, 25 and 26. Since there are no earthquakes listed in the PDE (Preliminary Determination Epicenters) with which these Rayleigh waves could be related, it is logical to assume that they were also generated by the El Chichon explosion. The fact that the Rayleigh waves persist on the transversely rotated, horizontal seismogram is clear evidence that the arrivals are from multiple paths other than the great circle route. Since the Rayleigh waves are not from a direct route, the origin time cannot be determined uniquely. However, the combined seismic and infrasonic acoustic signal pattern on the seismograms is strong evidence for a near-surface explosive source. Thus, certain infrasonic signals which are not "explosive-like" (Chimonas and Hines, 1970; Larson et al, 1971) may be discriminated effectively from further consideration; while others with both seismic and infrasonic acoustic signatures would be highly suspect as weapons tests.

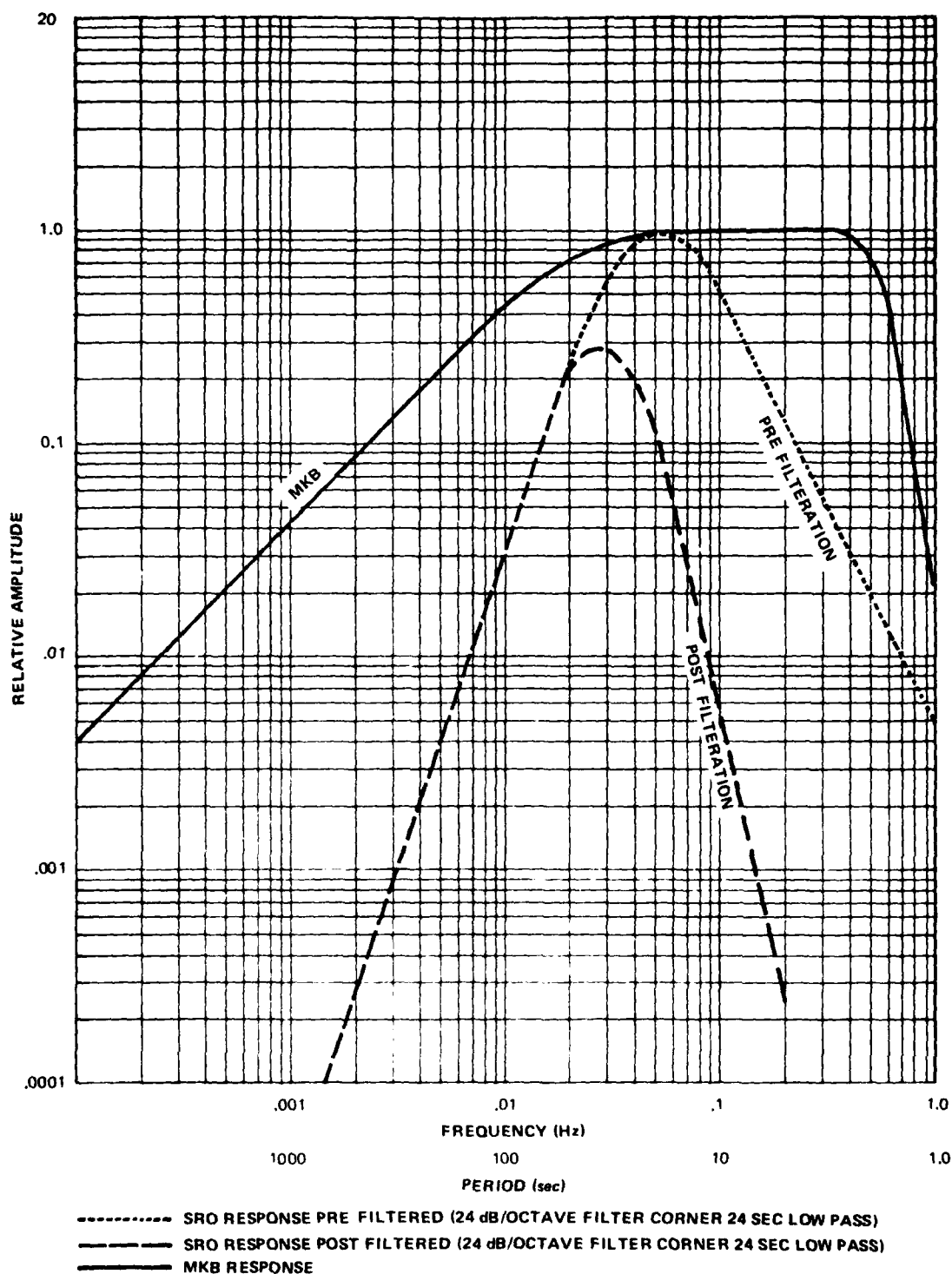
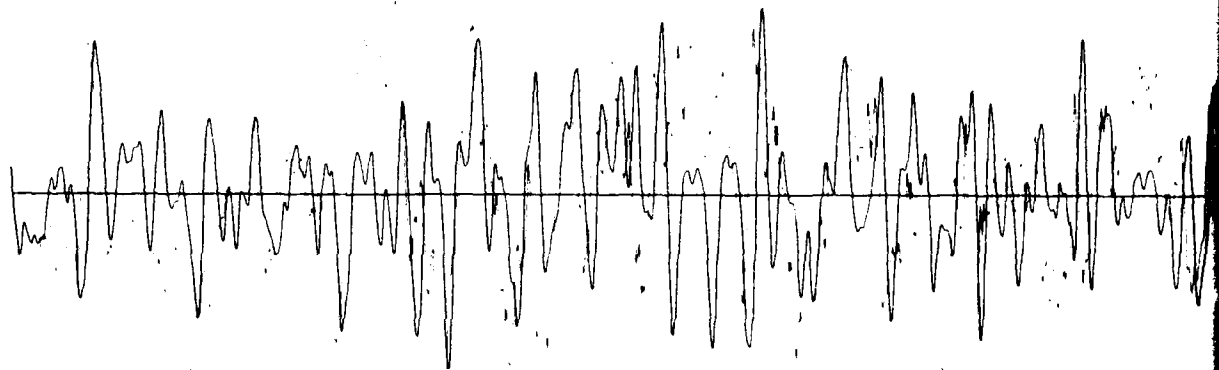
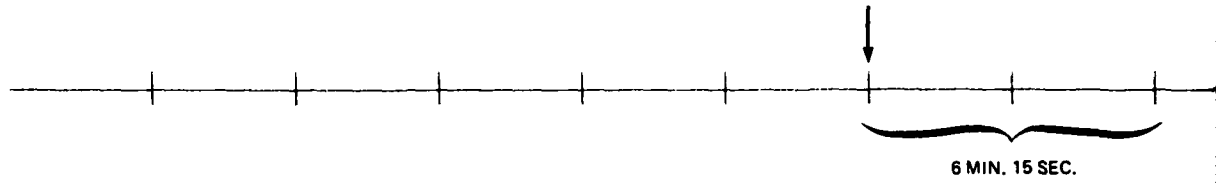


FIGURE 17. RELATIVE RESPONSES OF THE SEISMOGRAPHS TO DISPLACEMENT PRIOR TO AND POST FILTRATION (LOW-PASS FILTER CORNER 24 SECONDS, 24 DB/OCTAVE ROLL OFF). RESPONSE OF THE MICROBAROGRAPH TO PRESSURE IS SHOWN FOR COMPARISON.

G 13031

088 07:29:49 UCT



UCT

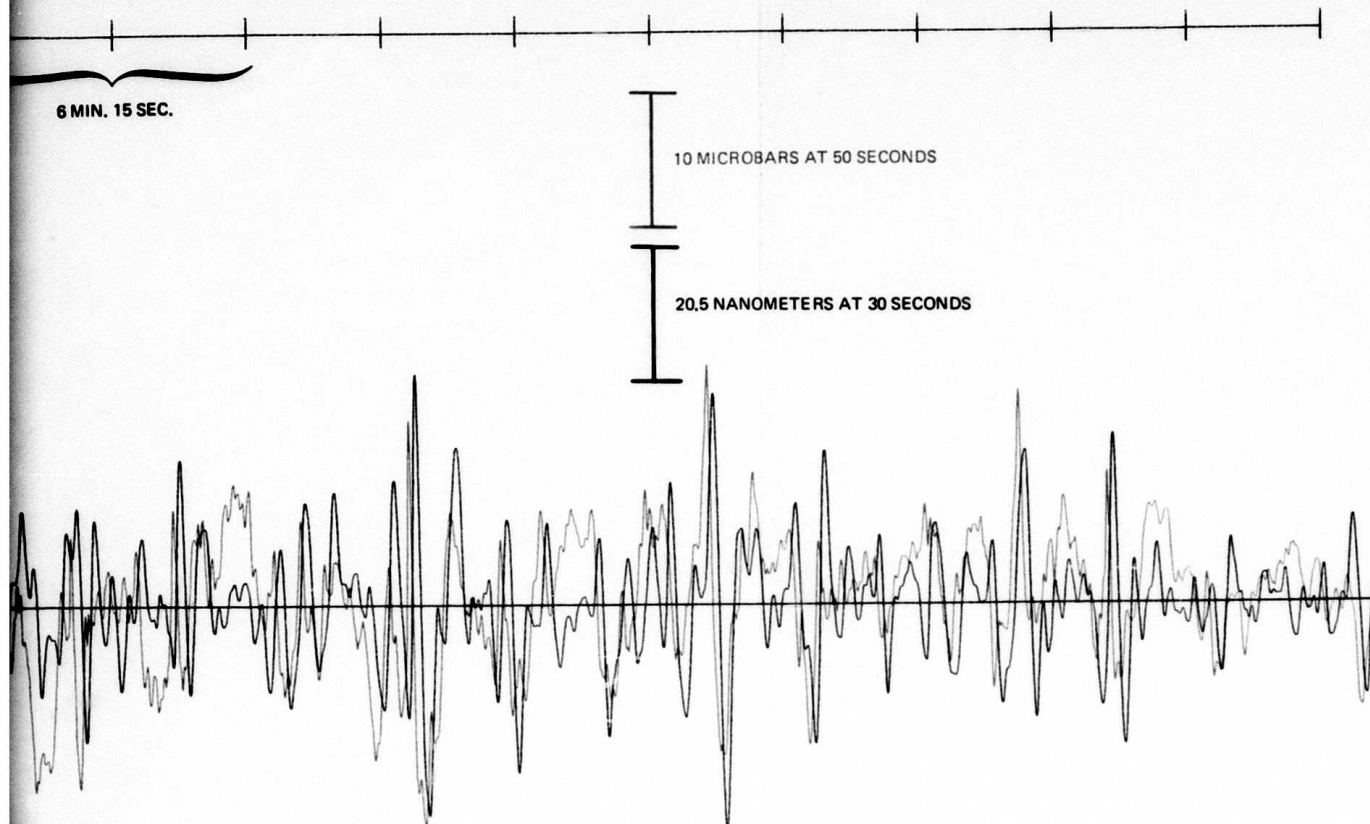


FIGURE 18. EL CHICHON ERUPTION ORIGIN TIME 088 ~ 05:32 UCT. BLACK LINE - LOW-PASS FILTERED VERTICAL SEISMOGRAM. RED LINE - MICRO-BAROGRAPH ARRAY BEAM STEERED AT AZIMUTH 168°

G 12978

-31/32-

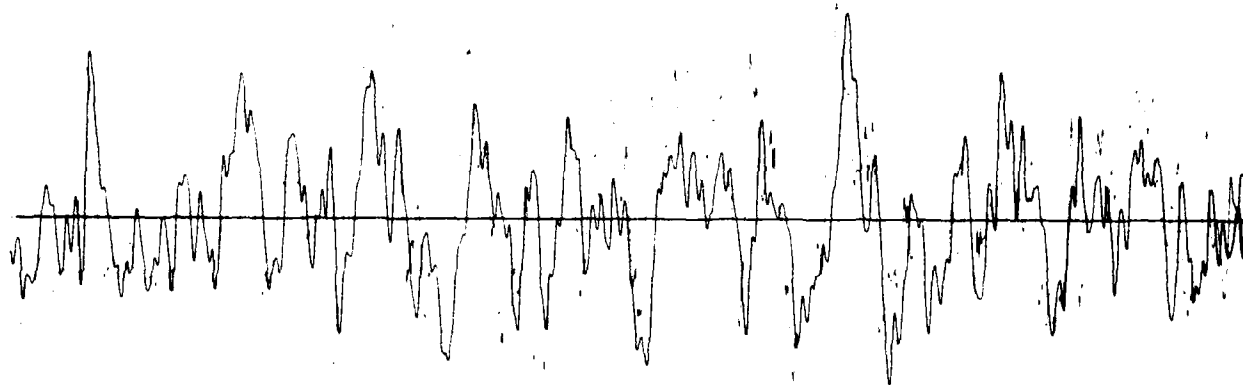
TR 82-5

12

088 07:29:49 UCT



6 MIN. 15 SEC.



6 MIN. 15 SEC.

10 MICROBARS AT 50 SECONDS

20.5 NANOMETERS AT 30 SECONDS

FIGURE 19. EL CHICHON ERUPTION ORIGIN TIME 088 ~
05:32 UCT. BLACK LINE - LOW-PASS FILTERED
RADIAL (168°) SEISMOGRAM. RED LINE -
MICROBAROGRAPH ARRAY BEAM STEERED
AT AZIMUTH 168°

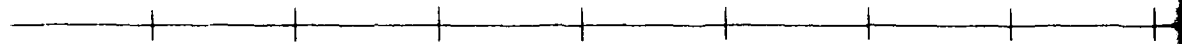
G 12979

-33/34-

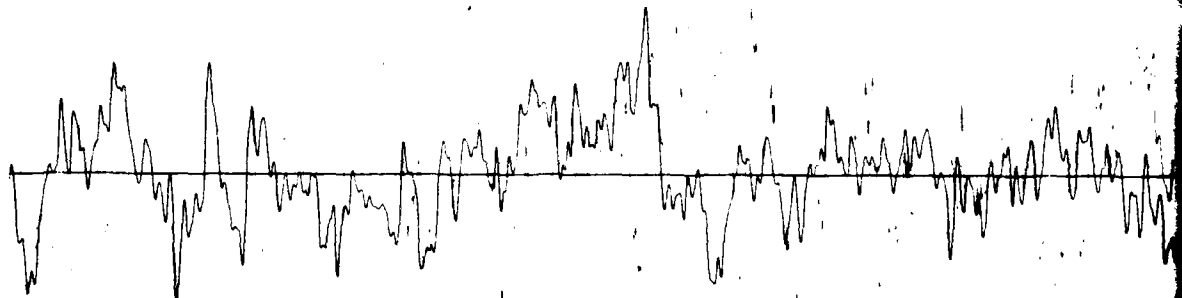
TR 82-5

1 2

088 07:29:49 UCT



6 MIN. 15 SEC.



UCT

6 MIN. 15 SEC.

10 MICROBARS AT 50 SECONDS

20.5 NANOMETERS AT 30 SECONDS

FIGURE 20. EL CHICHON ERUPTION ORIGIN TIME 088 ~
05:32 UCT. BLACK LINE - LOW-PASS FILTERED
TRANSVERSE (78°) SEISMOGRAM. RED LINE -
MICROBAROGRAPH ARRAY BEAM STEERED
AT AZIMUTH 168°

G 12980

-35/36-

TR 82-5

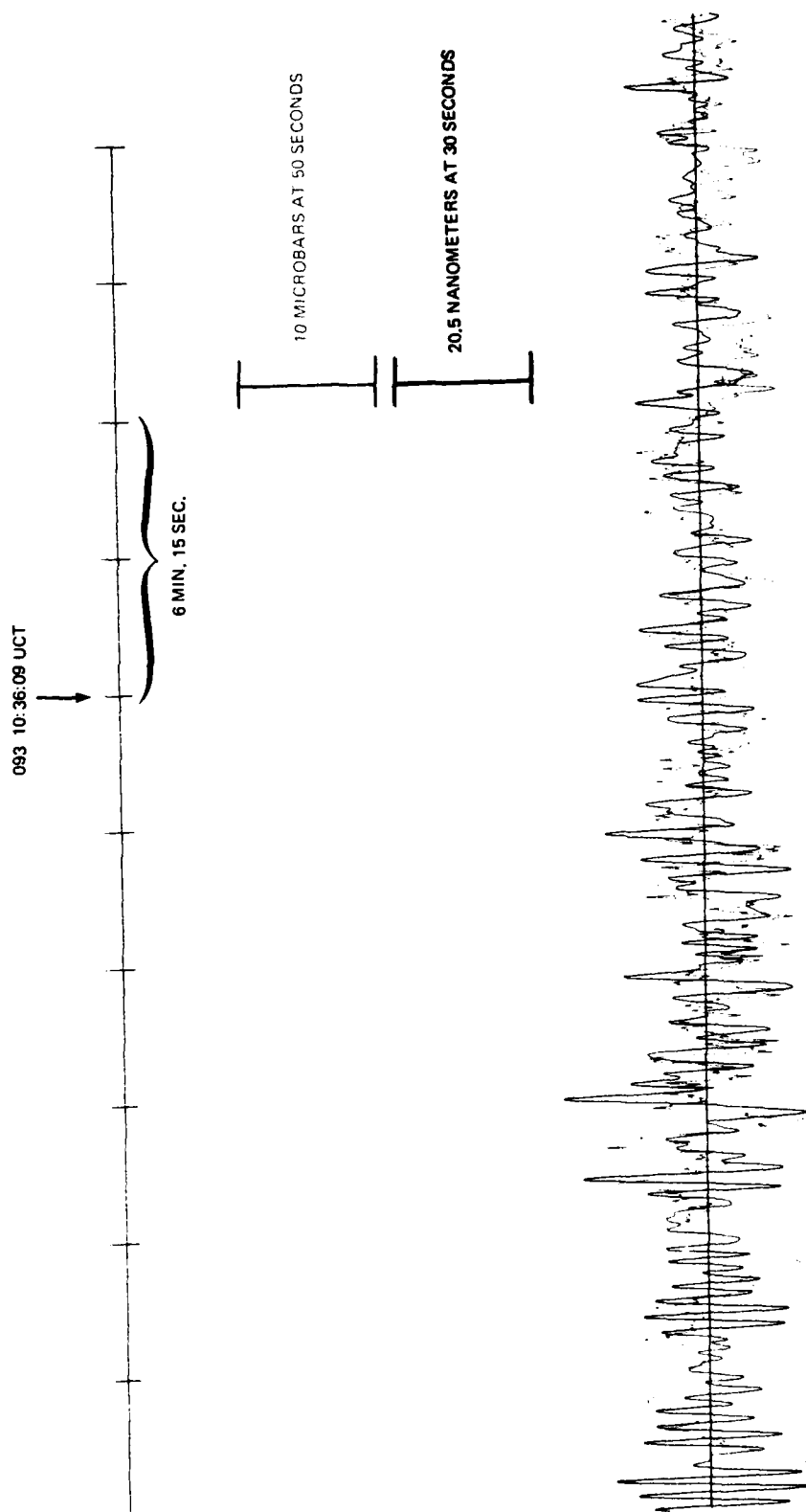


FIGURE 21. EL CHICHON ERUPTION ORIGIN TIME 093 ~ 08:50 UCT. BLACK LINE - LOW-PASS FILTERED VERTICAL SEISMOGRAM.
RED LINE - MICROBAROGRAPH ARRAY BEAM STEERED AT AZIMUTH 168°

G 12981

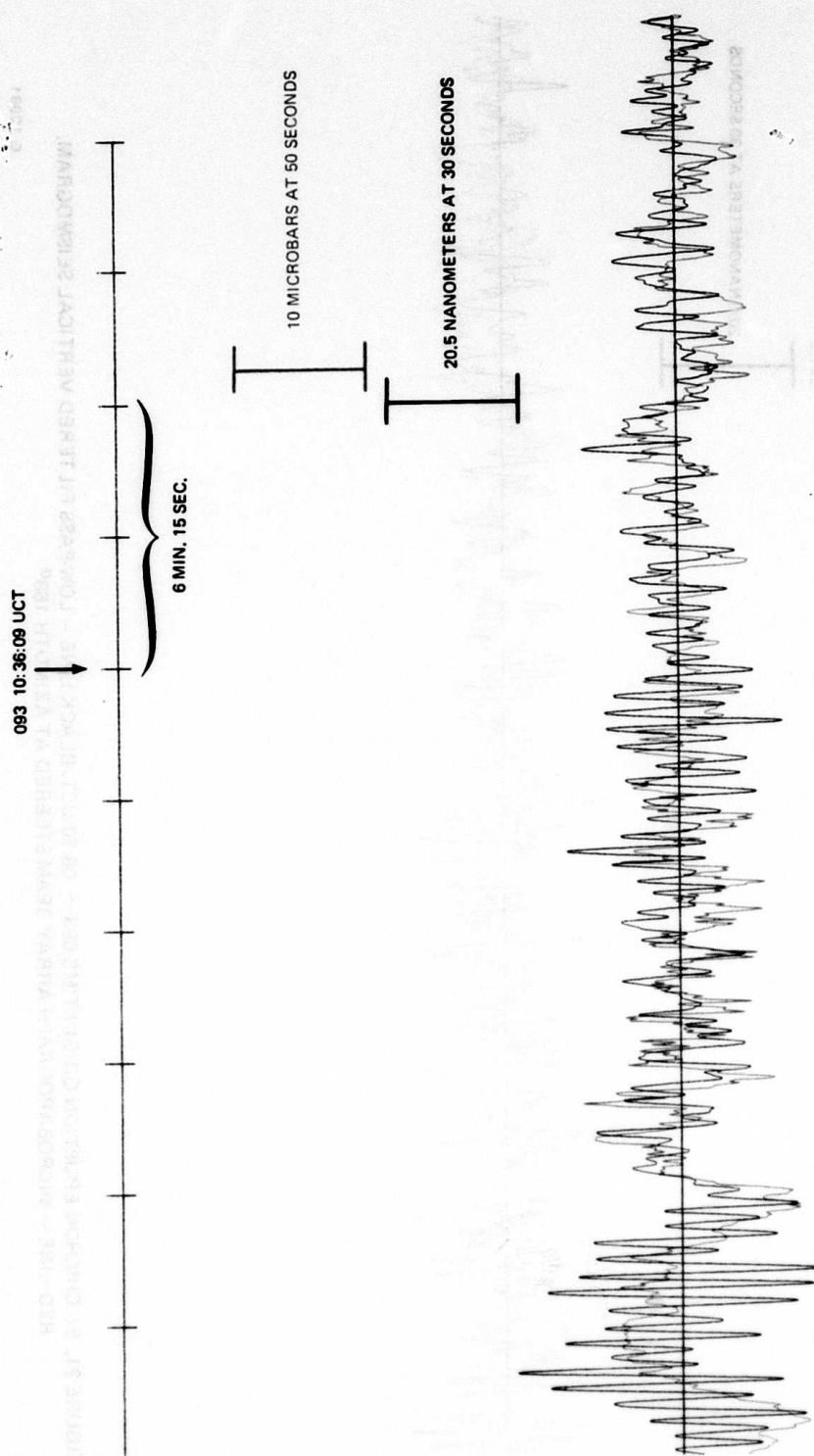
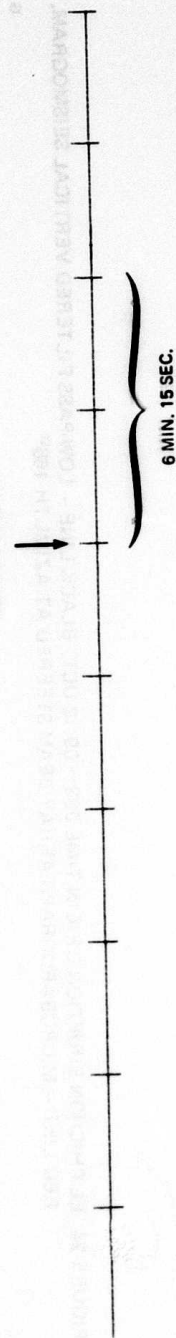


FIGURE 22. EL CHICHON ERUPTION ORIGIN TIME 093 ~ 08:50 UCT. BLACK LINE - LOW-PASS FILTERED RADIAL (168°) SEISMOGRAM.
RED LINE - MICROBAROGRAPH ARRAY BEAM STEERED AT AZIMUTH 168°

G 12982

093 10:36:09 UCT



10 MICROBARS AT 50 SECONDS

20.5 NANOMETERS AT 30 SECONDS

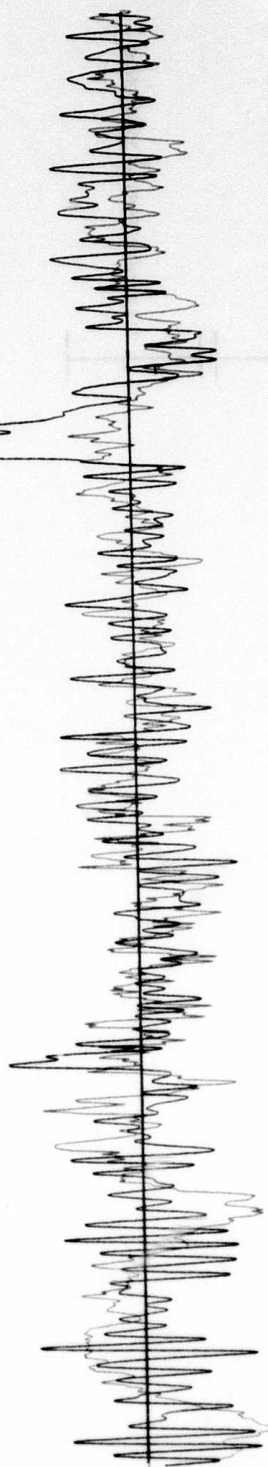


FIGURE 23. EL CHICHON ERUPTION ORIGIN TIME 093 ~ 08:50 UCT. BLACK LINE - LOW-PASS FILTERED TRANSVERSE (78°) SEISMOGRAM.
RED LINE - MICROBAROGRAPH ARRAY BEAM STEERED AT AZIMUTH 168°

G 12983

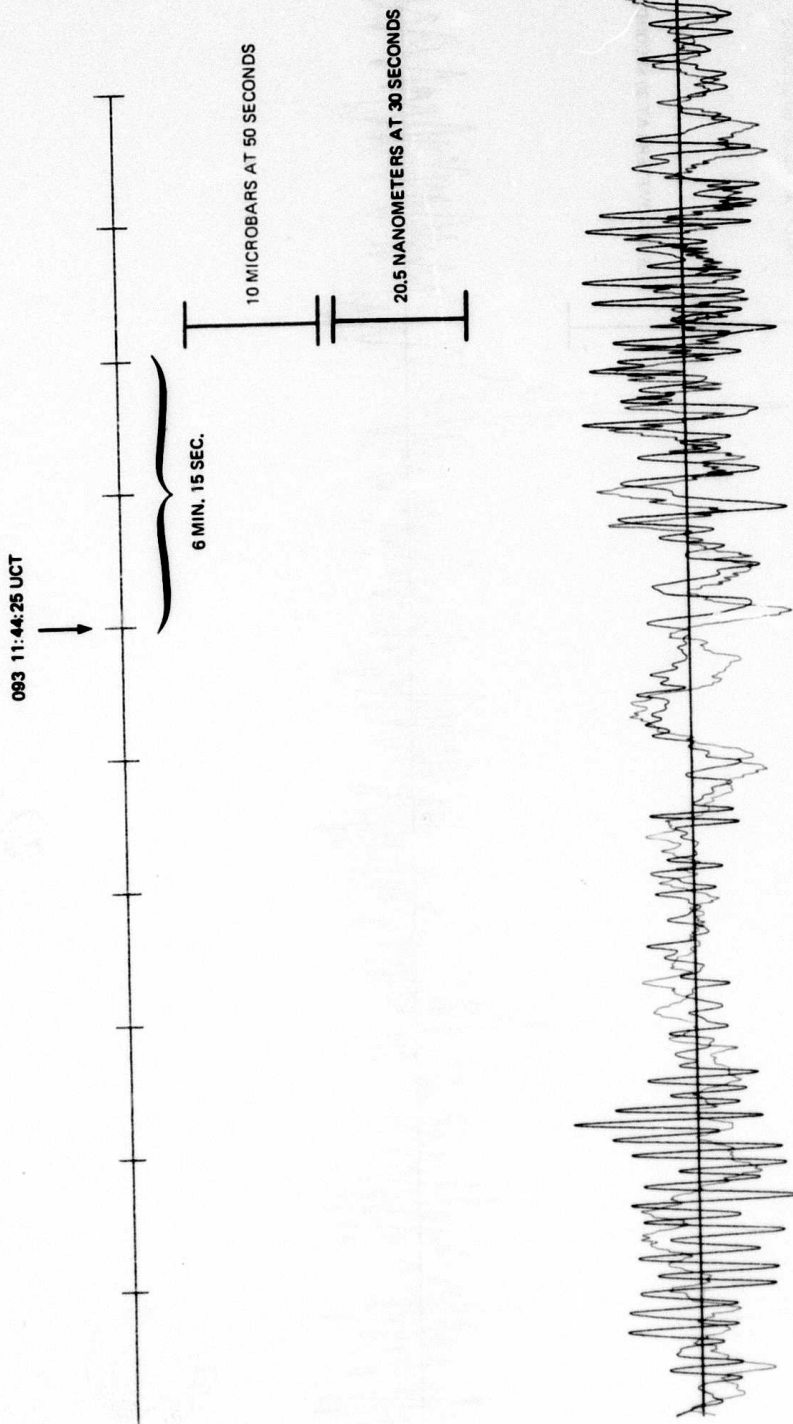


FIGURE 24. EL CHICHON ERUPTION ORIGIN TIME 093 ~ 09:12 UCT. BLACK LINE - LOW-PASS FILTERED VERTICAL SEISMOGRAM.
RED LINE - MICROBAROGRAPH ARRAY BEAM STEERED AT AZIMUTH 168°

G 12984

093 11:44:25 UCT



6 MIN. 15 SEC.



10 MICROBARS AT 50 SECONDS



20.5 NANOMETERS AT 30 SECONDS

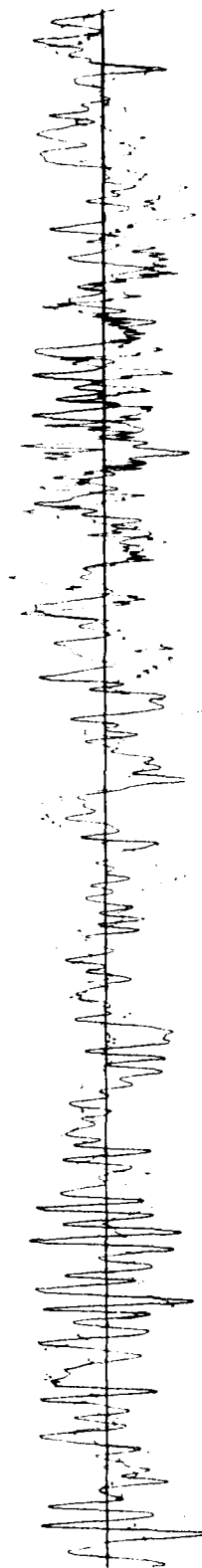


FIGURE 25. EL CHICHON ERUPTION ORIGIN TIME 093 ~ 09:12 UCT. BLACK LINE - LOW-PASS FILTERED RADIAL (168°) SEISMOGRAM.
RED LINE - MICROBAROGRAPH ARRAY BEAM STEERED AT AZIMUTH 168°

G 12985

093 11:44:25 UCT

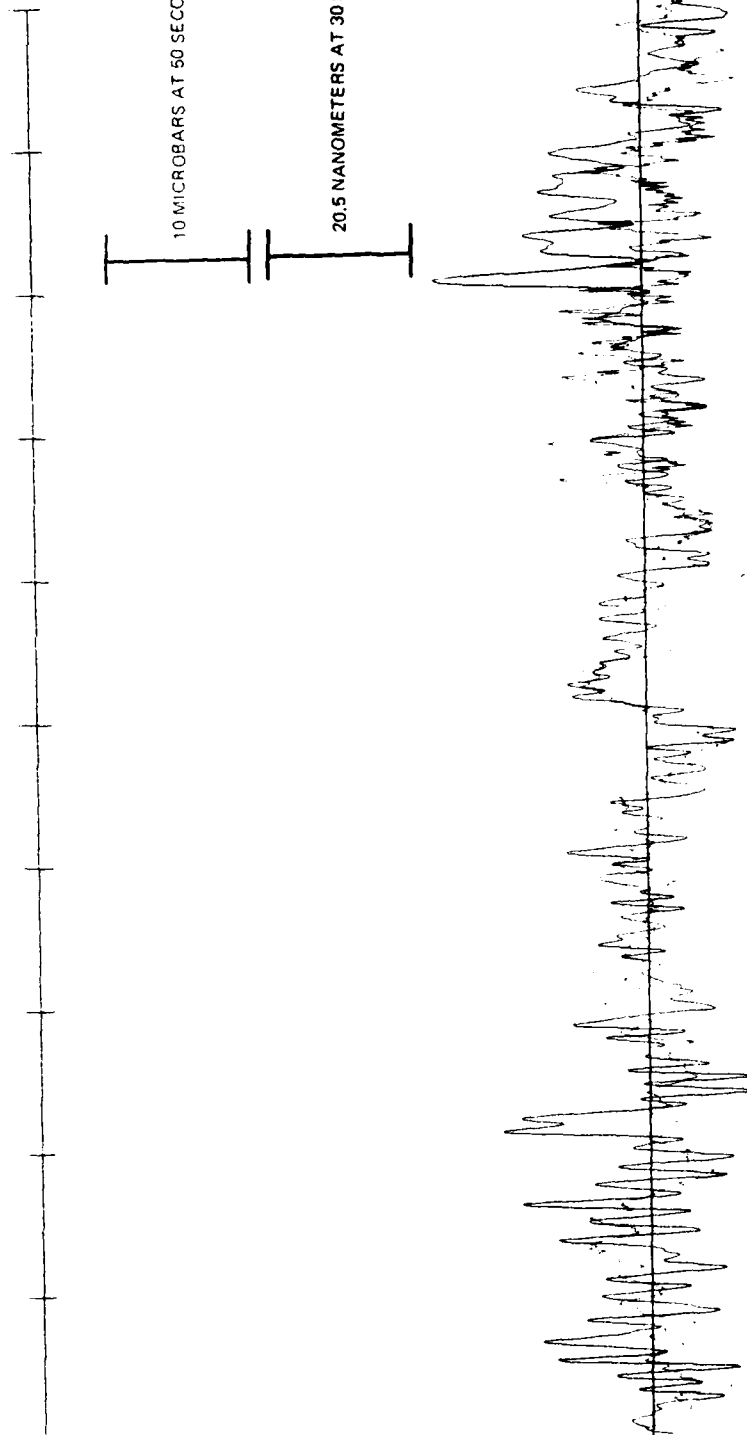


FIGURE 26. EL CHICHON ERUPTION ORIGIN TIME 093 ~ 09:12 UCT. BLACK LINE - LOW-PASS FILTERED TRANSVERSE (78°) SEISMOGRAM.
RED LINE - MICROBAROGRAPH ARRAY BEAM STEERED AT AZIMUTH 168°

G 12986

094 03:52:33 UCT

6 MIN. 15 SEC.

10 MICROBARS AT 50 SECONDS

20.5 NANOMETERS AT 30 SECONDS

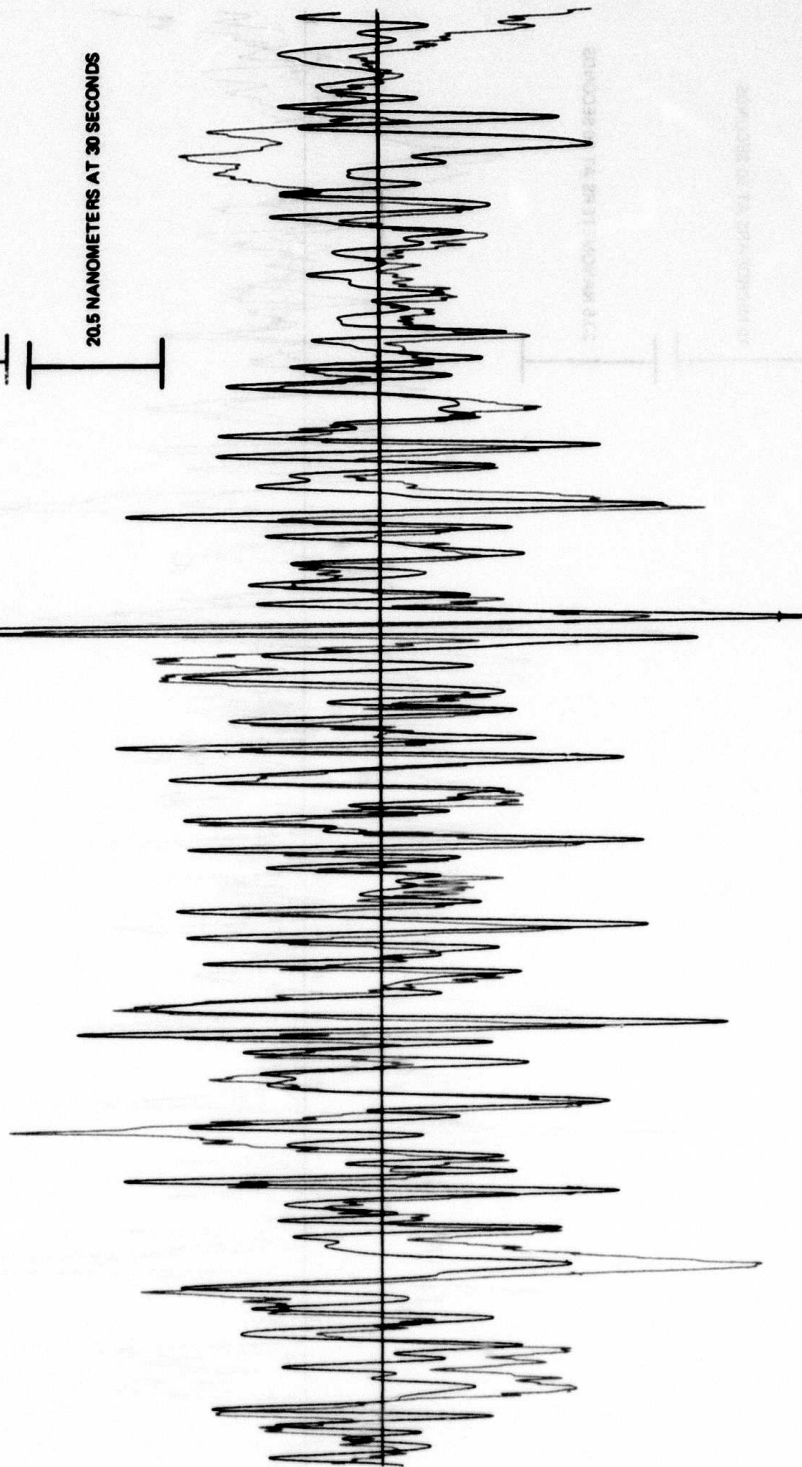


FIGURE 27. EL CHICHON ERUPTION ORIGIN 094 ~ 02:00 UCT. BLACK LINE - LOW-PASS FILTERED VERTICAL SEISMOGRAM. RED LINE - MICROBAROGRAPH ARRAY BEAM STEERED AT AZIMUTH 168°

G 12987

094 03:52:33 UCT

6 MIN. 15 SEC.

10 MICROBARS AT 50 SECONDS

20.5 NANOMETERS AT 30 SECONDS

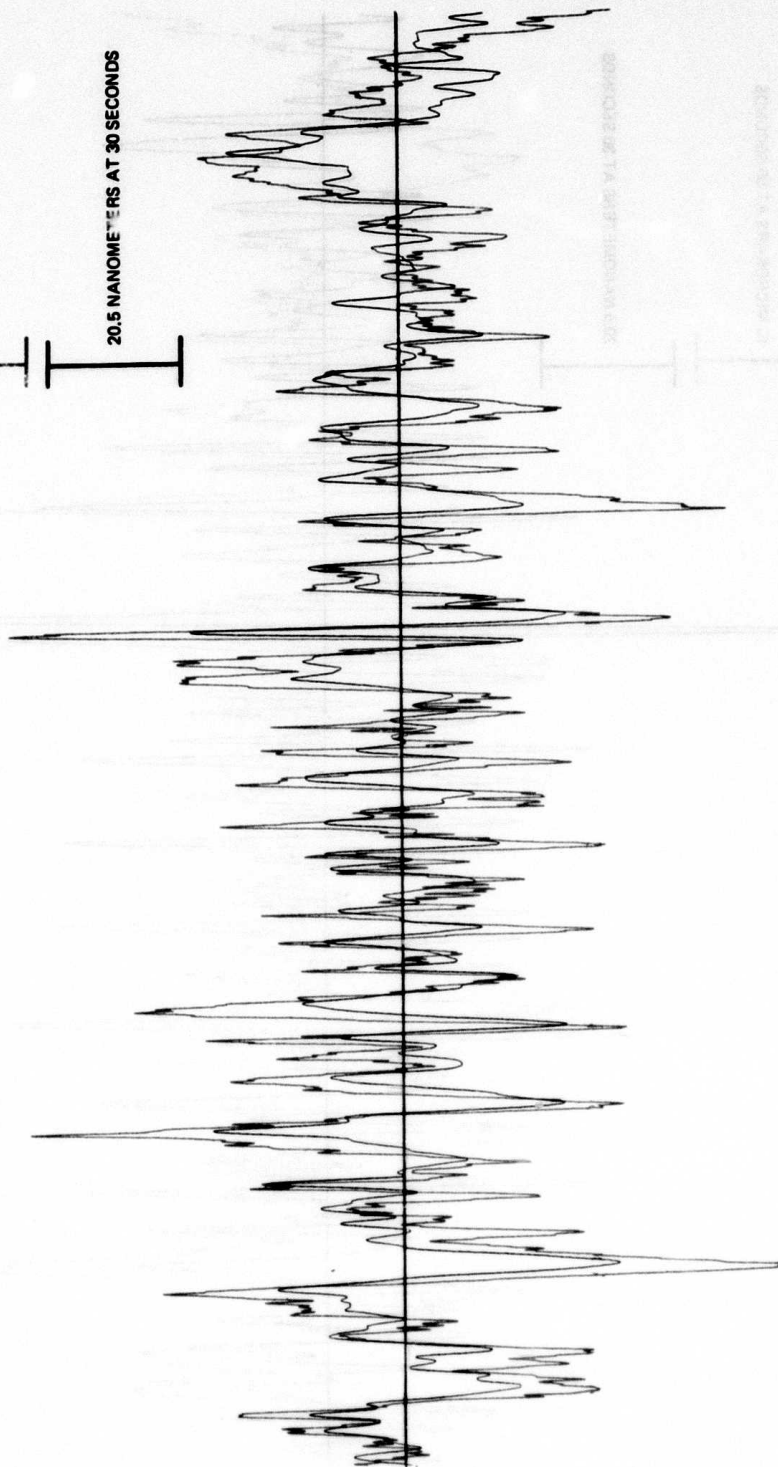


FIGURE 28. EL CHICHON ERUPTION ORIGIN TIME 094 ~ 02:00 UCT. BLACK LINE - LOW-PASS FILTERED RADIAL (168°) SEISMOGRAM. RED LINE - MICROBAROGRAPH ARRAY BEAM STEERED AT AZIMUTH 168°

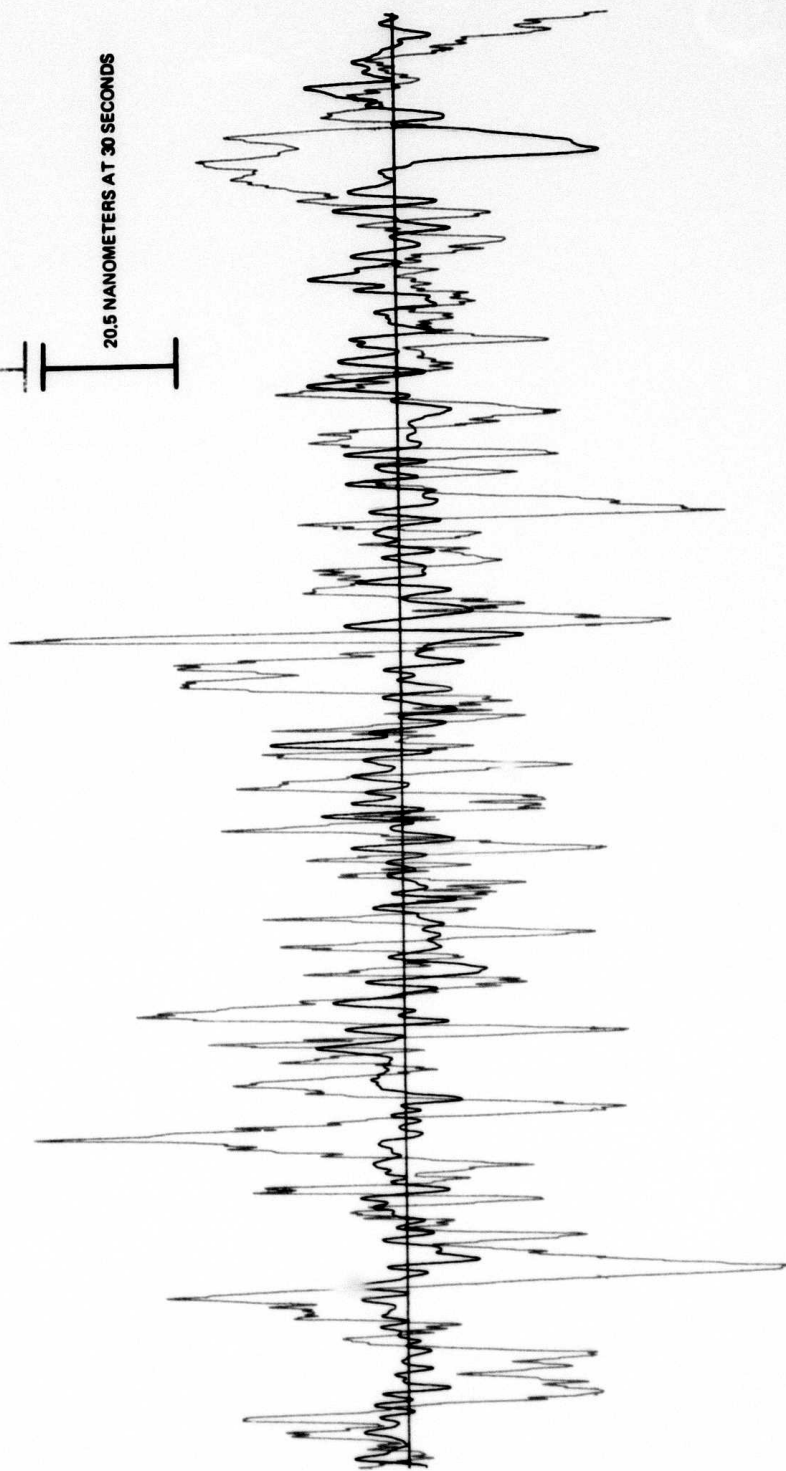
G 12988

094 03:52:33 UCT

6 MIN. 15 SEC.

10 MICROBARS AT 50 SECONDS

20.5 NANOMETERS AT 30 SECONDS

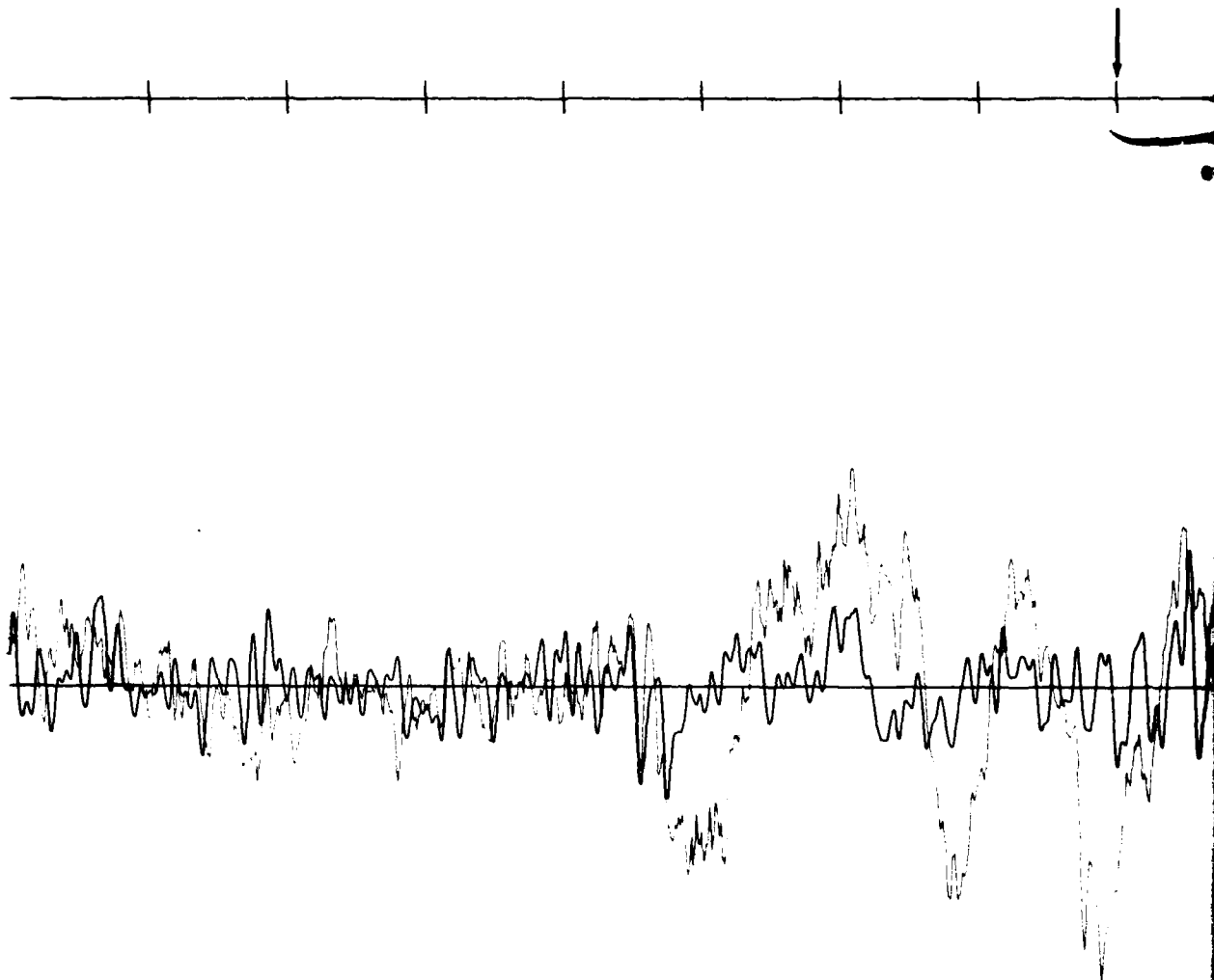


-45/46-

FIGURE 29. EL CHICHON ERUPTION ORIGIN TIME 094 ~ 02:00 UCT. BLACK LINE - LOW-PASS FILTERED TRANSVERSE (78°) SEISMOGRAM.
RED LINE - MICROBAROGRAPH ARRAY BEAM STEERED AT AZIMUTH 168°

G 12989

084 13:03:56 UCT



004 13:03:56 UCT

6 MIN. 15 SEC.

20.5 NANOM

10 MICROBA

1 2

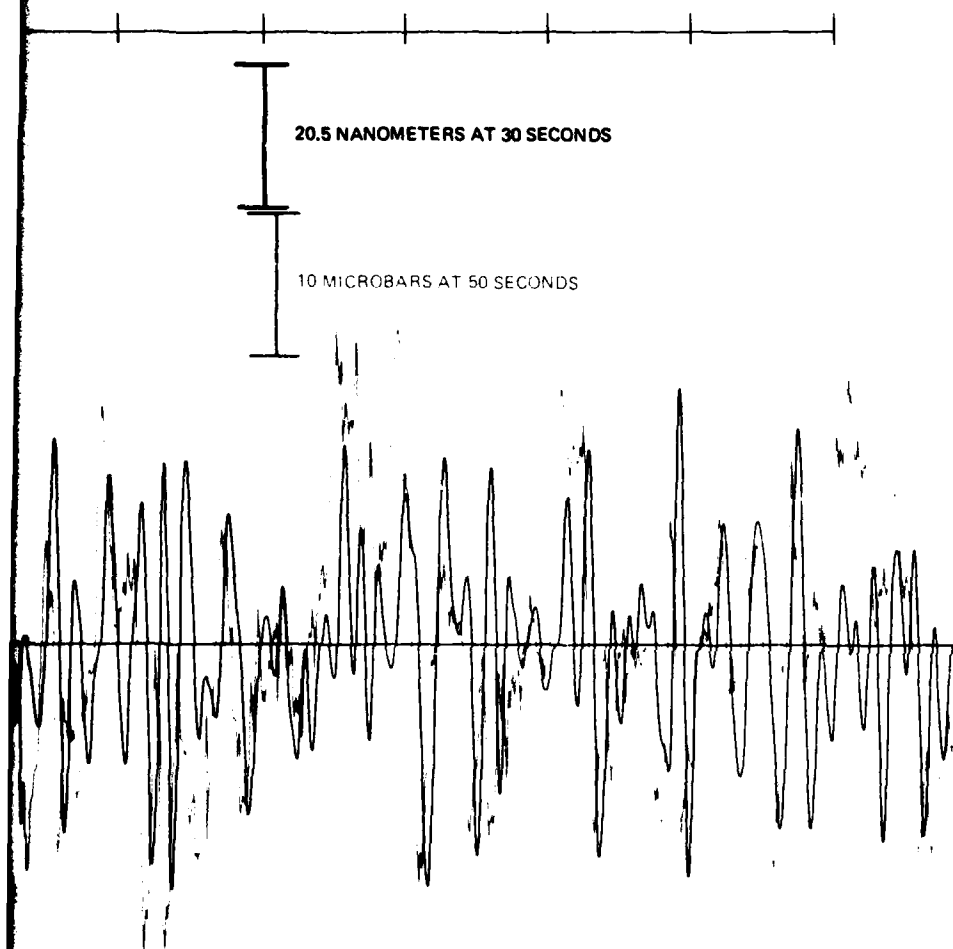
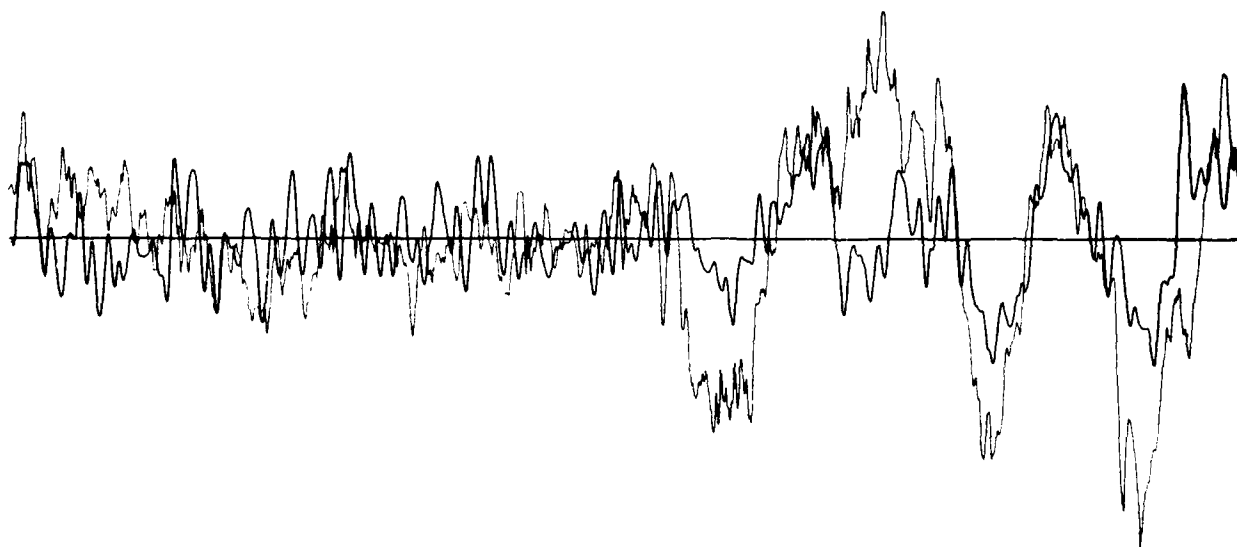
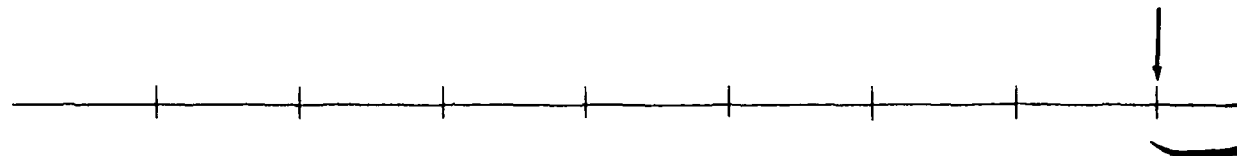


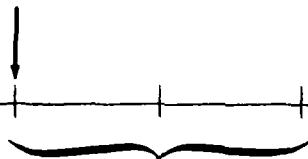
FIGURE 30. EL CHICHON ERUPTION ORIGIN TIME 094 ~
11:22 UCT. BLACK LINE - LOW-PASS FILTERED
VERTICAL SEISMOGRAM. RED LINE -
MICROBAROGRAPH ARRAY BEAM STEERED
AT AZIMUTH 168°

G 12990

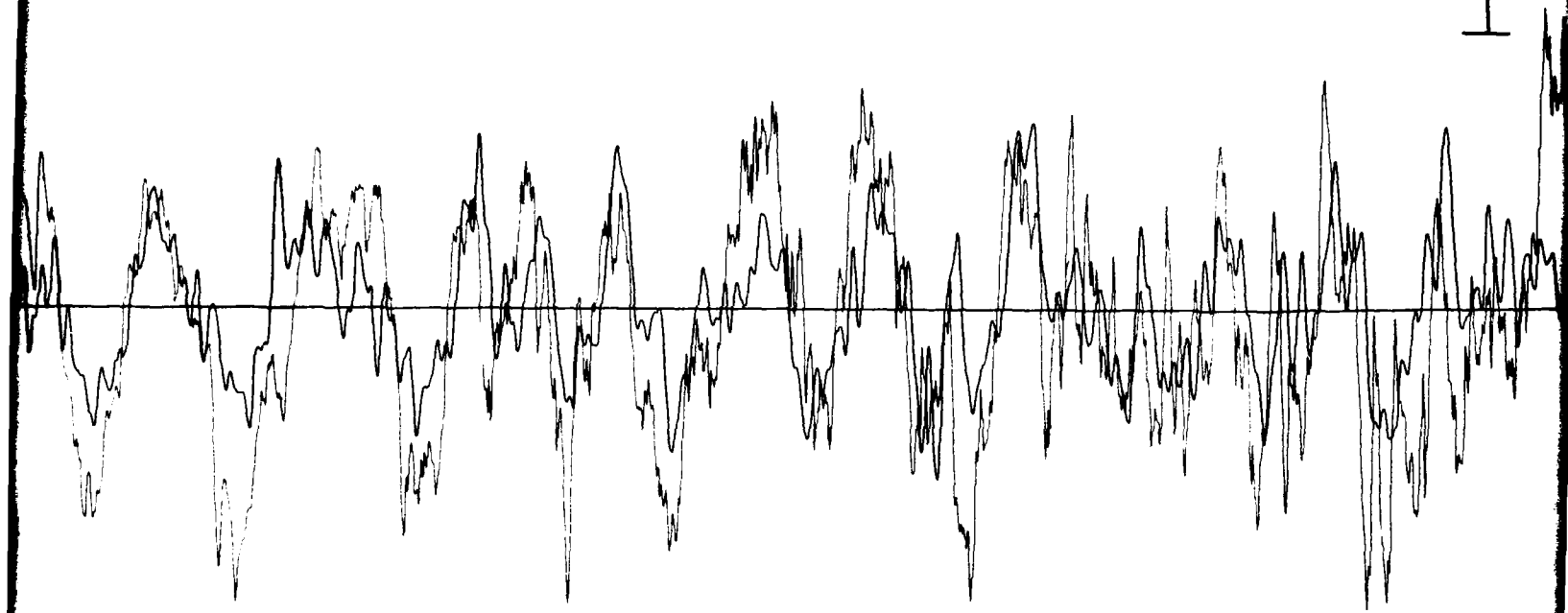
094 13:03:56 UCT



094 13:03:56 UCT



6 MIN. 15 SEC.



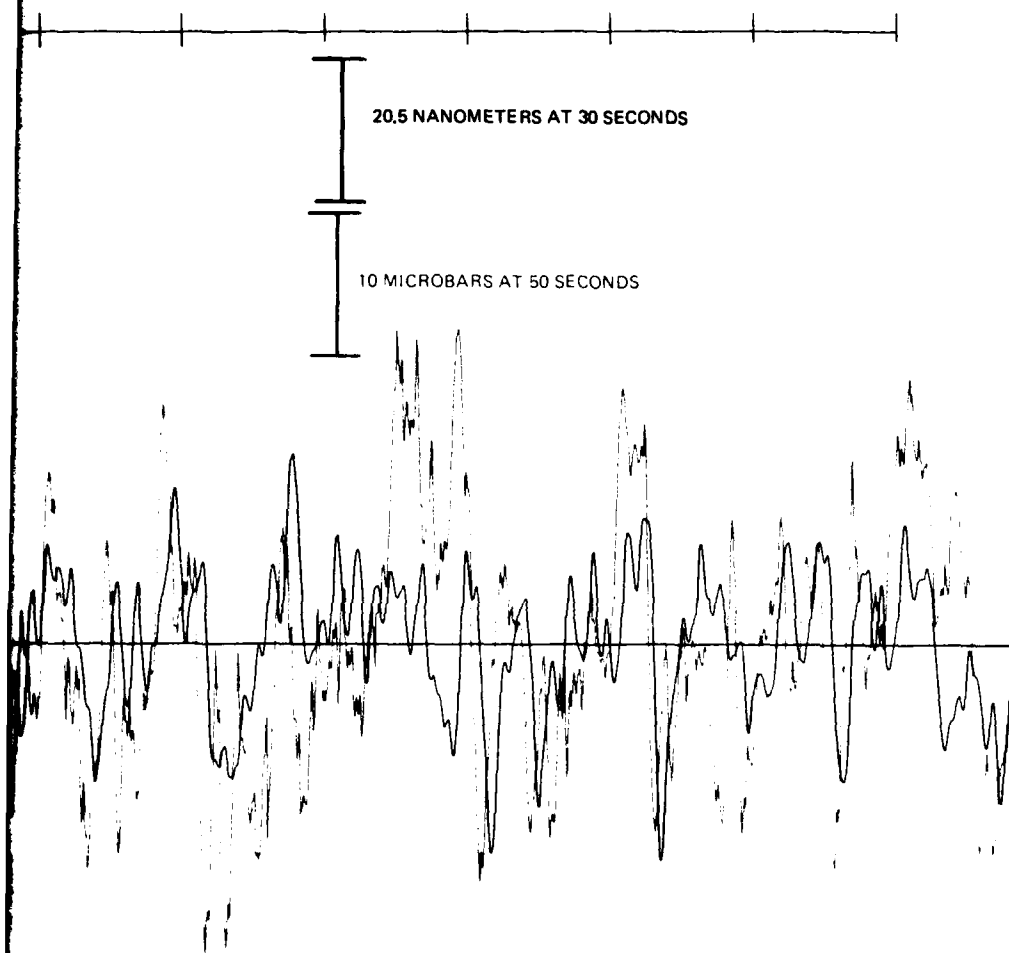
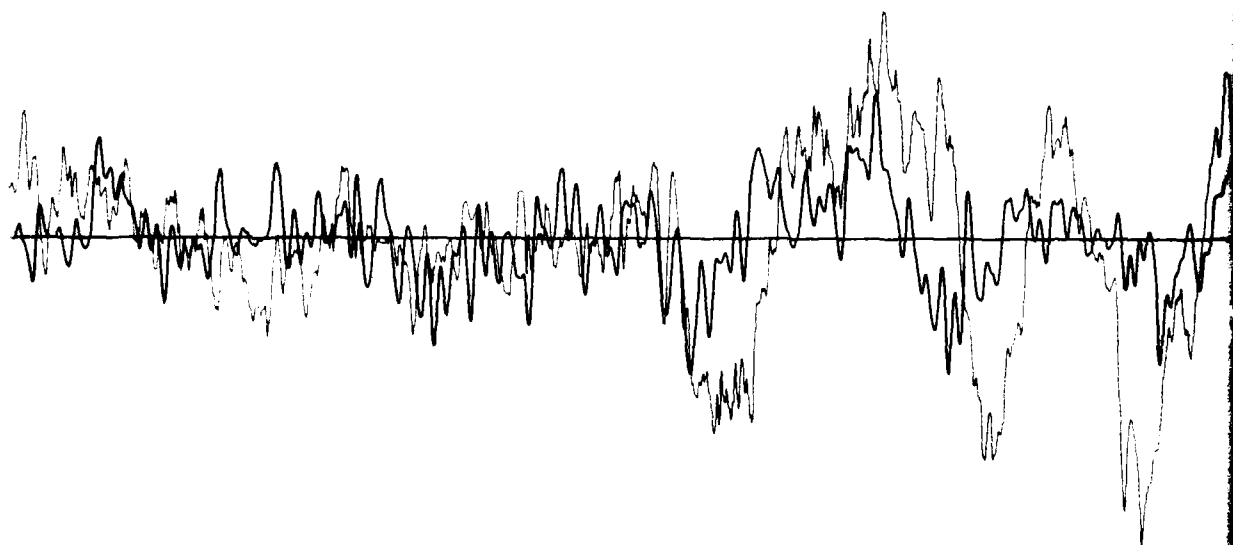
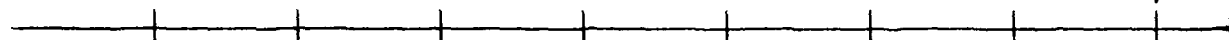


FIGURE 31. EL CHICHON ERUPTION ORIGIN TIME 094 ~
11:22 UCT. BLACK LINE - LOW-PASS FILTERED
RADIAL (168°) SEISMOGRAM. RED LINE -
MICROBAROGRAPH ARRAY BEAM STEERED
AT AZIMUTH 168°

G 12991

094 13:03:56 UC



004 13:03:58 UCT

6 MIN. 15 SEC.

20.5

10 MIC

2



20.5 NANOMETERS AT 30 SECONDS

10 MICROBARS AT 50 SECONDS

**FIGURE 32. EL CHICHON ERUPTION ORIGIN TIME 094 ~
11:22 UCT. BLACK LINE - LOW-PASS FILTERED
TRANSVERSE (78°) SEISMOGRAM. RED LINE -
MICROBAROGRAPH ARRAY BEAM STEERED
AT AZIMUTH 168°**

G 12992

-51/52-

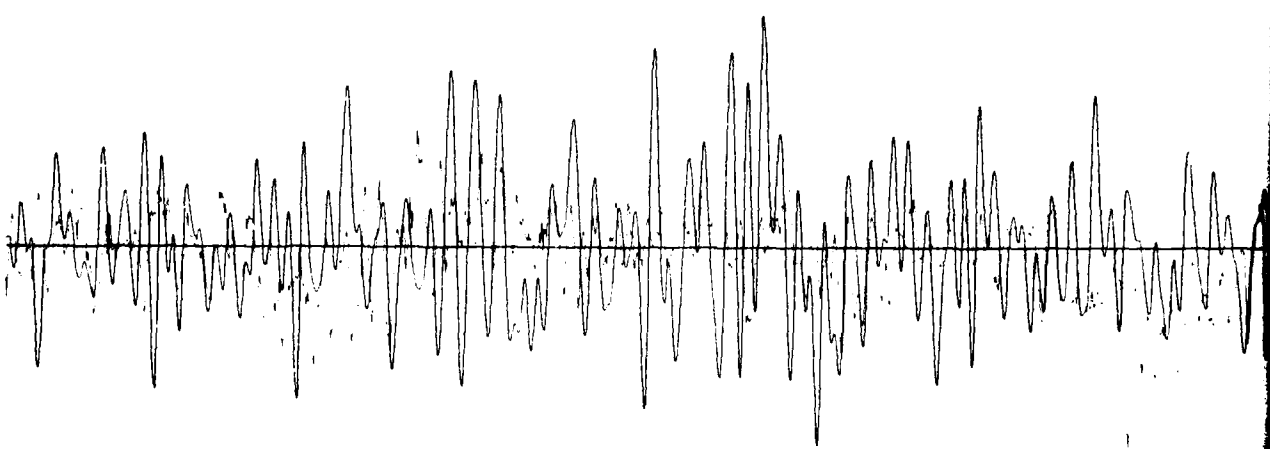
TR 82-5

3

094 12:15:01 UCT



6 MIN. 15 SEC.



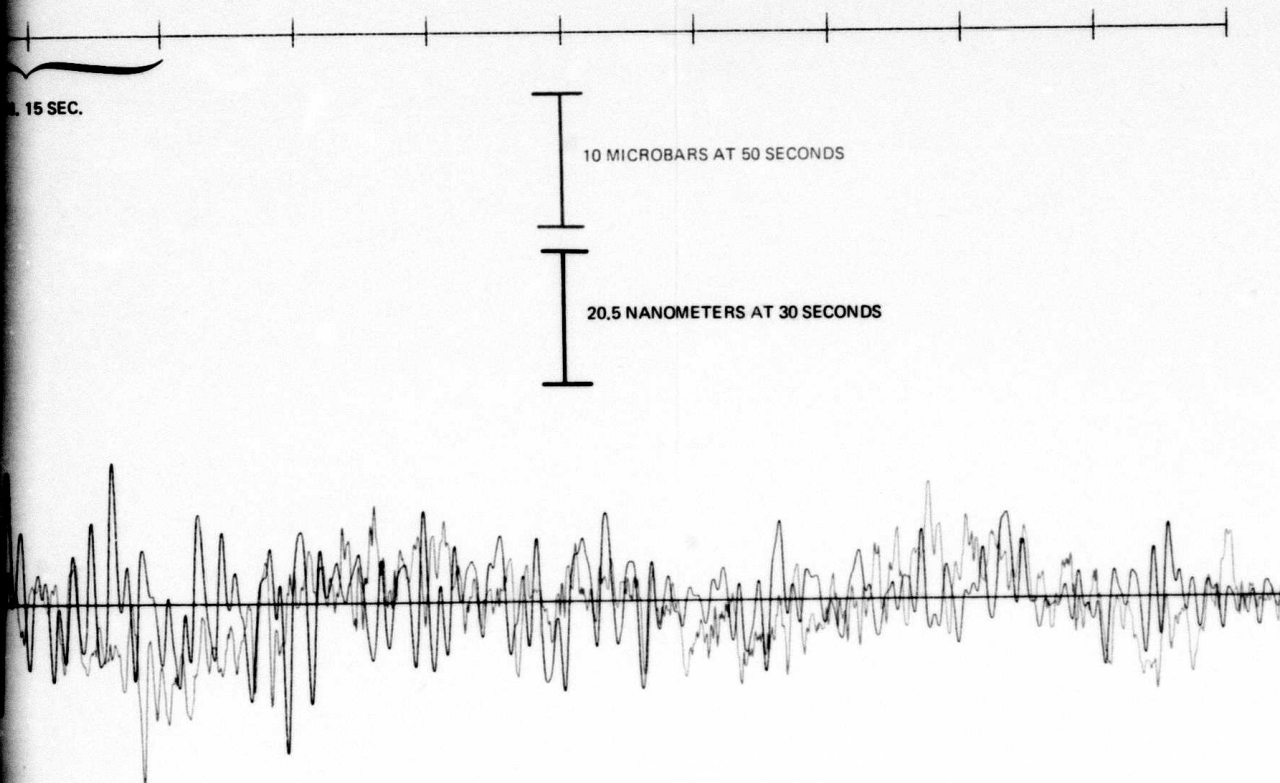


FIGURE 33. NOISE SAMPLE ORIGIN TIME 094 ~ 11:54 UCT.
BLACK LINE - LOW-PASS FILTERED VERTICAL
SIESMOGRAM, RED LINE - MICROBAROGRAPH
MKB NO. 1

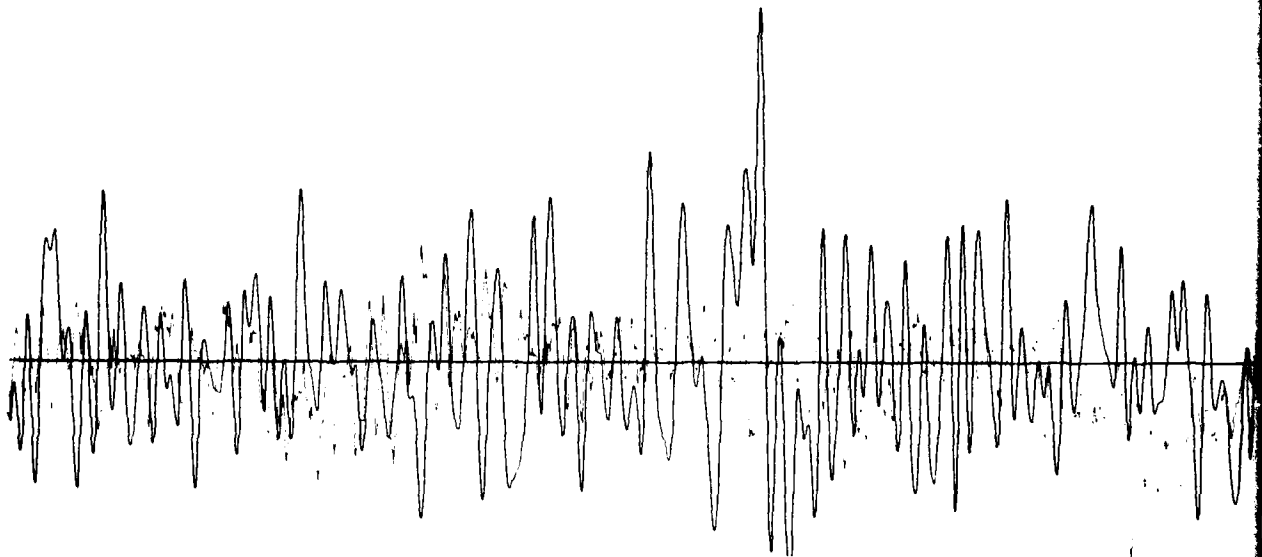
G 12993

1 2

094 12:15:01 UCT



6 MIN. 15 SEC.



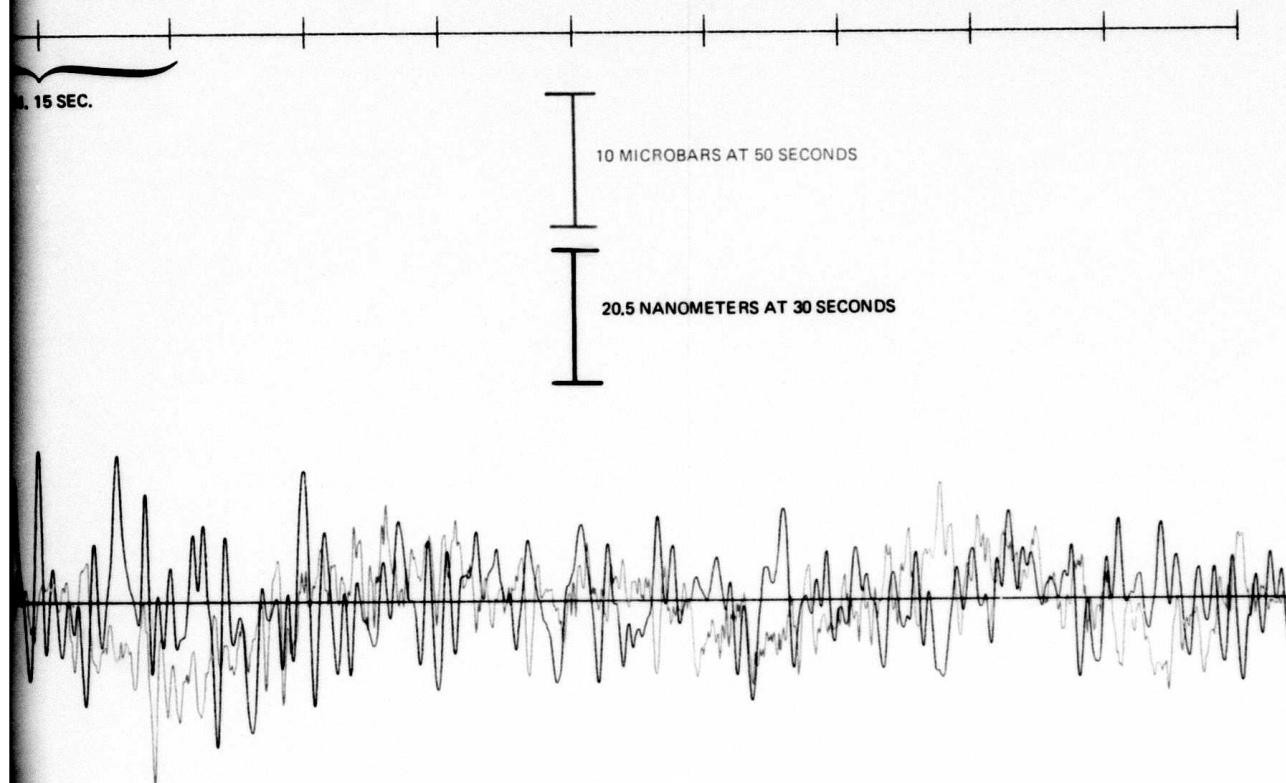
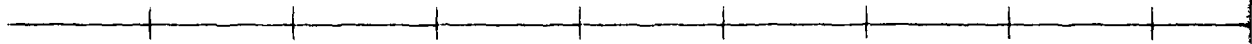


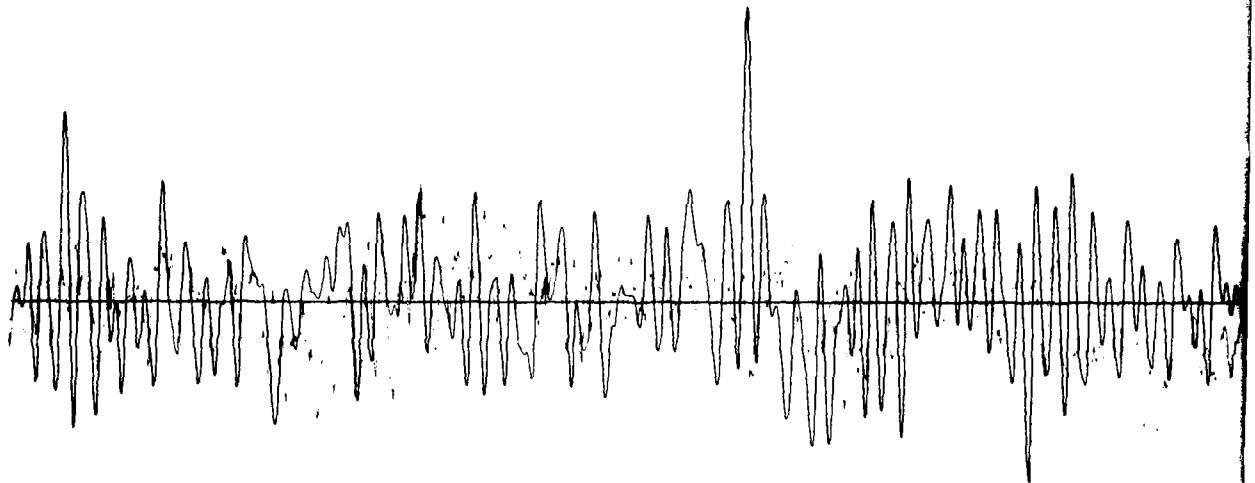
FIGURE 34. NOISE SAMPLE ORIGIN TIME 094 ~ 11:54 UCT.
BLACK LINE - LOW-PASS FILTERED NORTH-
SOUTH HORIZONTAL SEISMOGRAM. RED
LINE - MICROBAROGRAPH MKB NO. 1

G 12994

094 12:15:01 UCT



6 MIN. 15 SEC.



CT

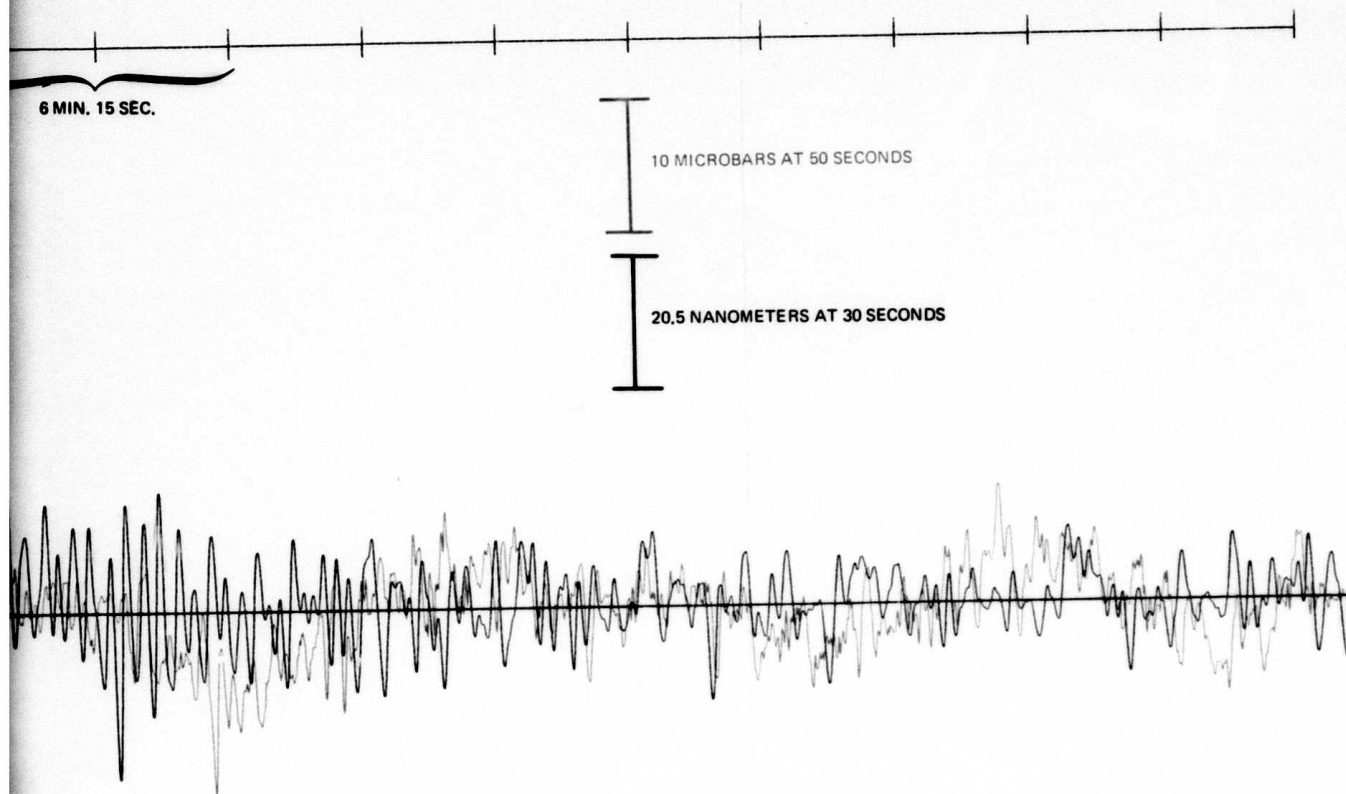


FIGURE 35. NOISE SAMPLE ORIGIN TIME 094 ~ 11:54 UCT.
BLACK LINE - LOW-PASS FILTERED EAST-
WEST HORIZONTAL SEISMOGRAM. RED LINE -
MICROBAROGRAPH MKB NO. 1

G 12995

2

2.4.2 Quantitative Analysis of the El Chichon Eruptions

In the previous section, we discussed some of the qualitative aspects of the recorded infrasonic-acoustic signals from five of the explosions in the El Chichon eruption sequence. This section will focus on more quantitative analyses of the El Chichon explosions. The coherences of the microbarograms and the seismograms for the five eruption periods are examined first. The measurements of the amplitudes and periods of various identified infrasonic-acoustic/gravity modes recorded on seismograms and microbarograms are discussed second. Specific emphasis is placed on the determination of the microbarometric amplitudes of infrasonic signals from seismic displacement measurements. Likelihood errors associated with such determinations also are discussed. The utilization of the infrasonic-acoustic data to estimate the energy release or approximately equivalent yield of the explosions will be discussed in section 2.4.3.

The ordinary coherence estimates of the microbarometric and seismic noise fields during two ambient wind conditions were discussed in section 2.3. The coherences of the noise fields for RMS wind velocities of one mile-per-hour and thirteen miles-per-hour are illustrated in figures 10 and 11. Utilizing the same algorithm, we have performed coherence estimates between the beam-steered microbarometric data and the vertical, radial and transverse components of the seismic data illustrated in figures 18-35. These coherence studies serve two important functions. First, they yield insight into cospectral power levels of the signals observed on different instruments. These can assist significantly in design of more complex detection algorithms. Second, they yield insight into the likely detection threshold spectrum. If the event studied can be related to a defined energy release, then this information can be related to the yield detection threshold.

The coherences between the microbarograms and the vertical, radial and transverse seismograms for the five El Chichon eruptions are illustrated in figures 36, 38, 40, 42, and 44. The coherences between the vertical and radial, vertical and transverse, and radial and transverse seismograms for these events are illustrated in figures 37, 39, 41, 43, and 45. The RMS wind velocities during the times of these recordings were generally in the range of seven miles-per-hour or less and, therefore, are representative of moderately low wind conditions. Comparing the coherences of the microbarograms with the three seismogram components results in several conclusions. The correlation of the transverse seismograms and the microbarograms is negligible for the spectral range from 0.1 hertz to 0.001 hertz for all eruptions studied. On the other hand, both the vertical and radial seismograms display well-defined spectral components which strongly correlate with the microbarograms. In addition, there is a slight tendency for a higher level of coherence between the radial seismogram and the microbarogram than between the vertical seismogram and microbarogram for nearly all events.

The coherences between the microbarograms and the vertical seismograms generally display three distinct spectral regions of high coherence separated by two spectral regions of low coherence. The high-coherence lobes are between 0.0025 and 0.0035 hertz (400 - 285 sec), 0.006 and 0.02 hertz (167 - 50 sec), and 0.04 and 0.06 hertz (25 - 17 sec). These three spectral bands

correspond well with the defined limits of the $GR_0 + S_0$, $S_1 + S_2$, and S_n ($n \geq 3$) infrasonic-acoustic modes defined by Pierce (1966). Comparing the two lower frequency spectral lobes of the events for which relative size has been estimated (088, 093-A, 093-B, and 094), there is a tendency for the centroids to be at higher frequencies for smaller events, and the spectral lobe to be of more limited extent. Finally, as the event size decreases, there is correspondingly less correlation between the microbarogram and the seismogram. This is a result of decreased signal-to-noise ratios.

Comparing the coherence of the vertical, radial and transverse seismograms (figures 37, 39, 41, 43, 45), there are no similar, obvious features. The coherence of the radial and transverse components generally is the lowest correlation for all events, while vertical and radial and vertical and transverse coherence generally appear to be approximately the same. The similarity of the two horizontal component coherences with the vertical component undoubtedly is related to the high level of Rayleigh mode microseismic noise which, without filtration, dominates the records. In fact, the only energy lobe from the infrasonic signal spectrum which is marginally coherent is the low-frequency lobe corresponding to the S_0 mode. The conclusion which can be drawn from these results is that filtration to remove the microseismic noise is required if seismic data are to be used without a collocated microbarograph for successful extraction of the infrasonic signal information.

Utilization of observed infrasonic-acoustic signals to determine reliably the yield of atmospheric nuclear detonations or energy release of volcanic explosions is a similar problem to estimation of the yield of underground nuclear explosions or magnitude of earthquakes from surface wave measurements. Analogous to surface wave quantitative analysis procedures, we measured the periods and amplitudes of the individual waves comprising the A_1 signals as well as the maximum amplitude in and duration of the A_1 wave trains from the five principal eruptions of El Chichon. All measurements were corrected for instrument response. The results of the five microbarometric record measurements are summarized in table 3 and illustrated in figure 46. To facilitate discussion of these results, the frequency limits of some of the infrasonic-acoustic modes and the gravity mode, GR_0 , are illustrated at the top of each period-amplitude graph in figure 46. The identification code for the event from which the data were derived is given in the lower right-hand corner of the individual diagrams. Measurement range bars are illustrated about most mean measurements. In general, these represent total ranges of measurements and are not related to a robust statistical uncertainty level. No range bars are indicated when a single wave of specific amplitude and period was measured. The dashed lines connecting separate observations or observation means on each diagram are to illustrate general period-amplitude trends of the data and are not indicative of a continuous wave dispersion. In fact, we will illustrate a standard moving window analysis (Landisman, Dziewonski and Sato, 1969) of the 093A event which clearly demonstrates the classical guided wave character of the infrasonic-acoustic wave train.

Comparing the period-amplitude graphs of the microbarometric signals from the five different explosive eruptions results in several interesting observations. With the exception of event 088 (figure 46a) which is known to

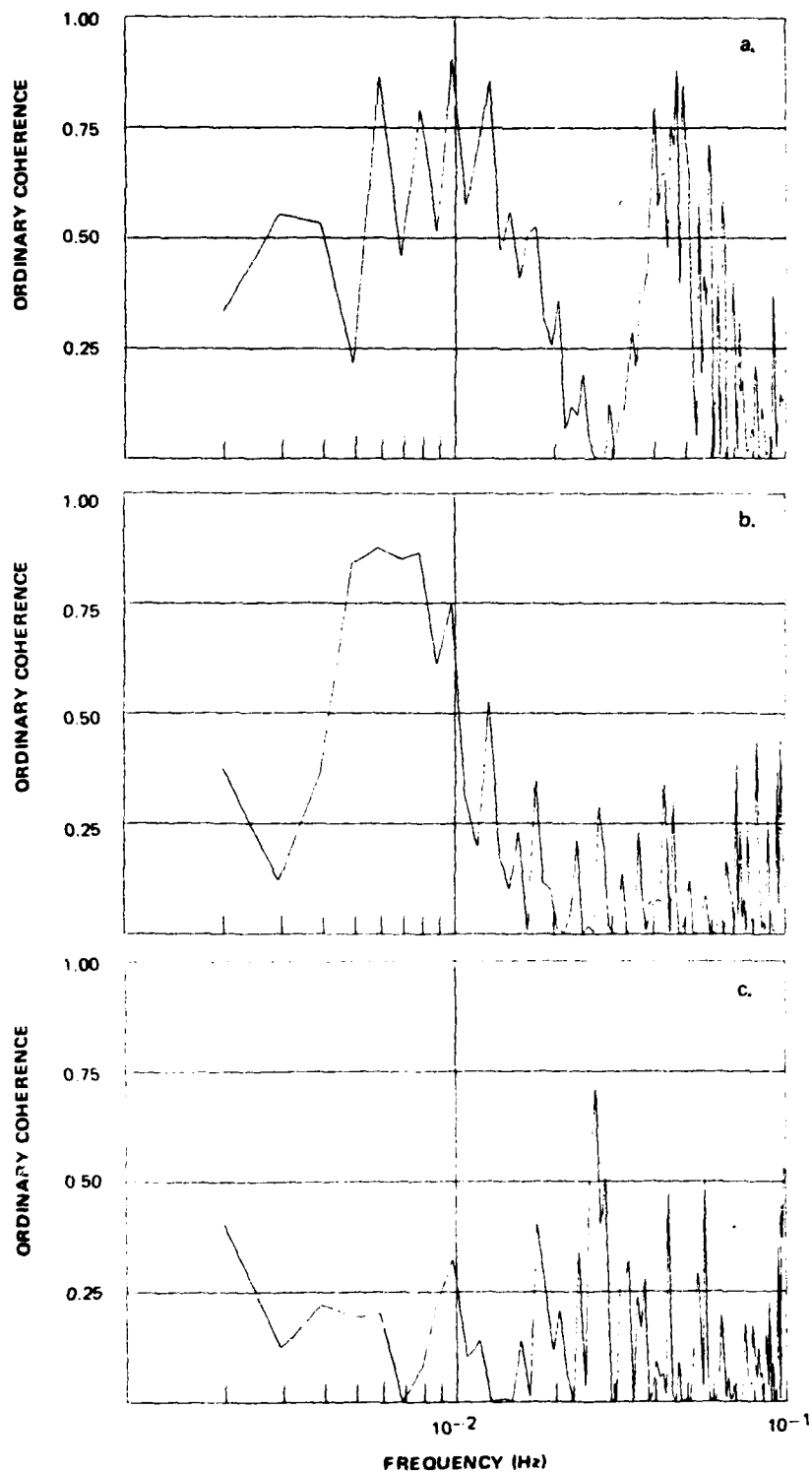


FIGURE 36. ORDINARY COHERENCE ESTIMATES FOR THE EL CHICHON ERUPTION 088 BETWEEN THE MICROBAROGRAPH ARRAY BEAM AND THE VERTICAL (a), RADIAL (b) AND TRANSVERSE (c) SEISMOGRAMS. (9 BLOCK SAMPLE/75% OVERLAP)

G 12996

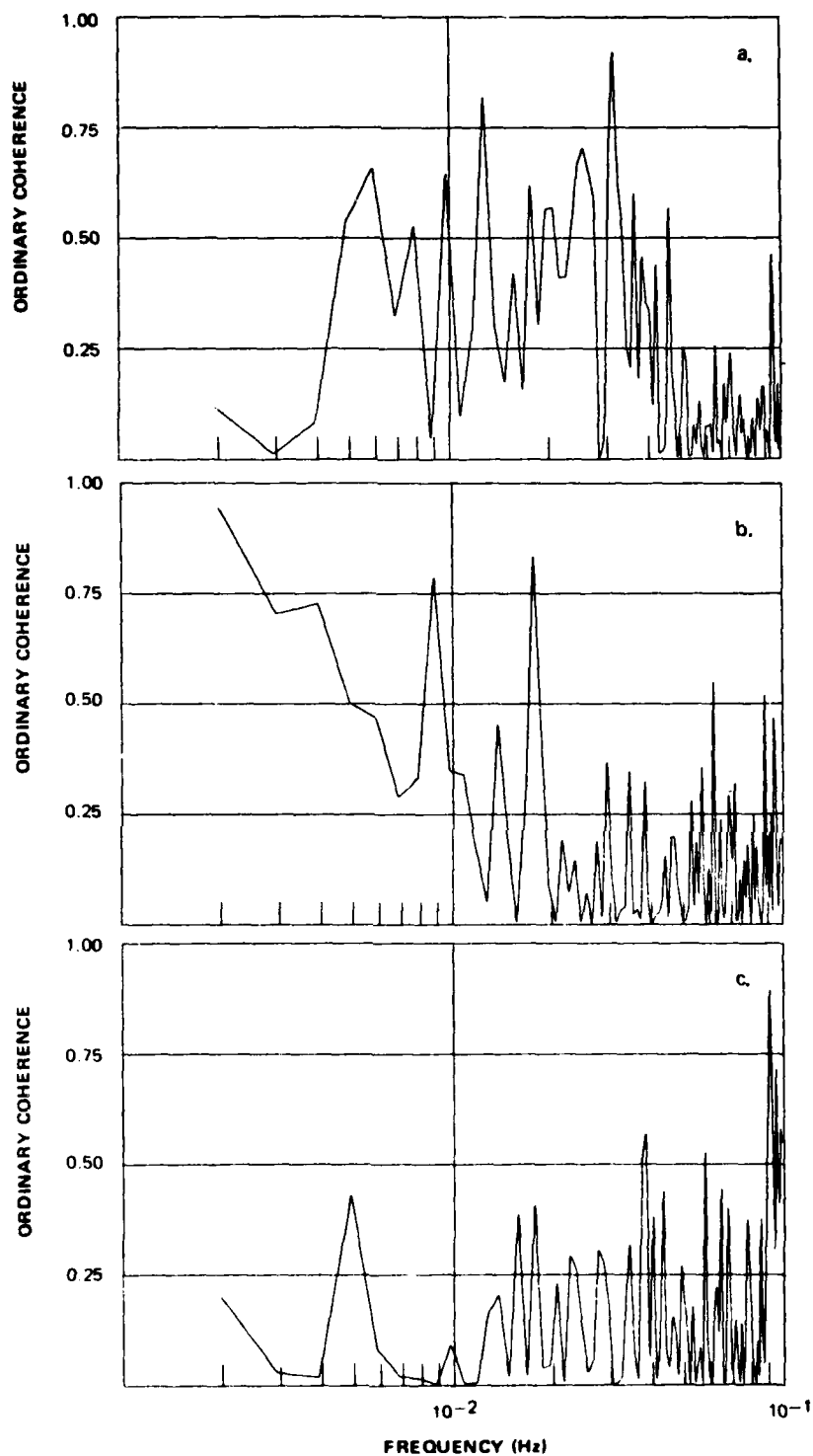


FIGURE 37. ORDINARY COHERENCE ESTIMATES FOR THE EL CHICHON ERUPTION 088 BETWEEN PAIRS OF THE THREE SEISMOGRAM COMPONENTS: (a) VERTICAL AND RADIAL, (b) VERTICAL AND TRANSVERSE, (c) RADIAL AND TRANSVERSE. (9 BLOCK SAMPLE/75% OVERLAP)

G 12997

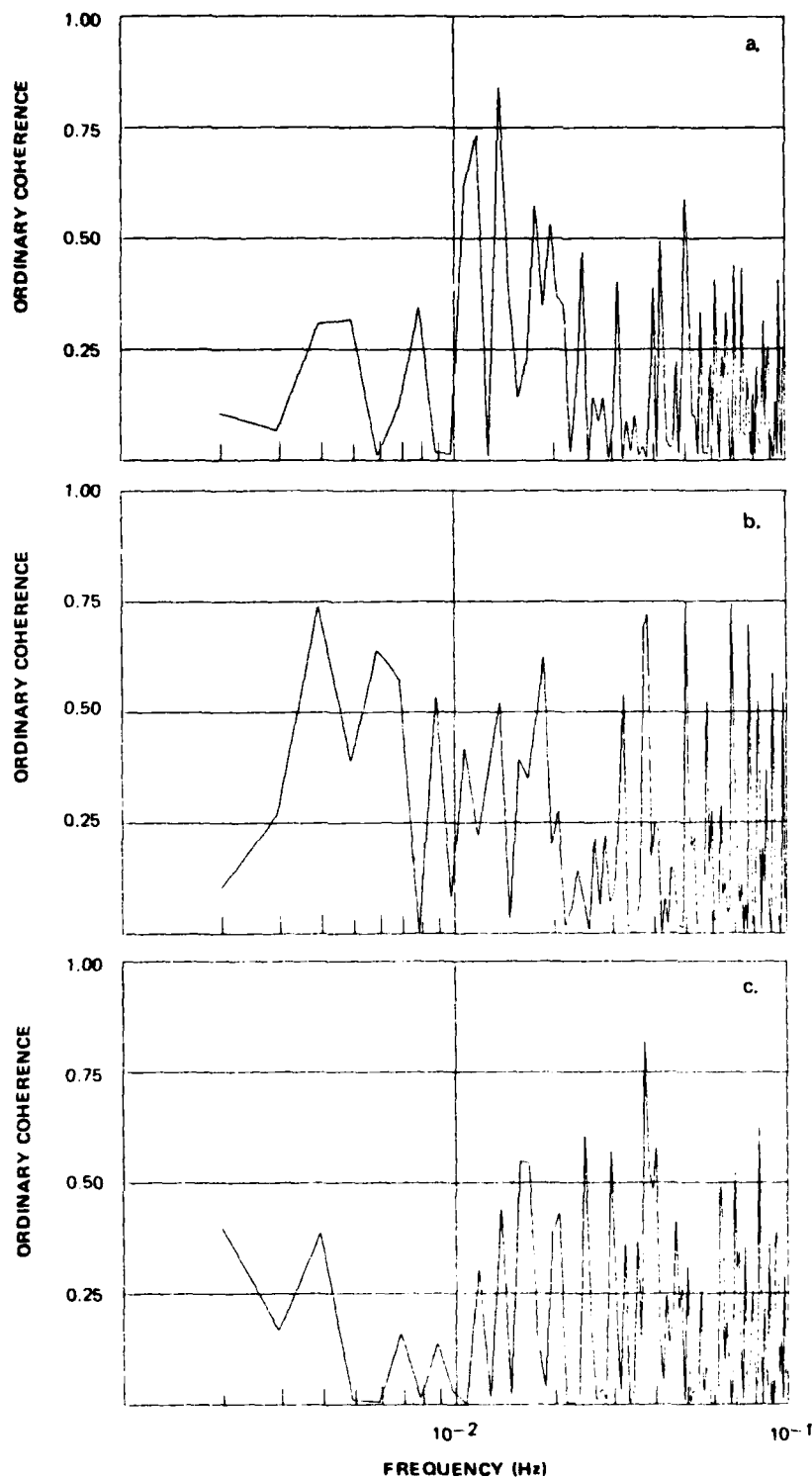


FIGURE 38. ORDINARY COHERENCE ESTIMATES FOR THE EL CHICHON ERUPTION 093-A BETWEEN THE MICROBAROGRAPH ARRAY BEAM AND THE VERTICAL (a), RADIAL (b) AND TRANSVERSE (c) SEISMOGRAMS. (9 BLOCK SAMPLE/75% OVERLAP)

G 12998

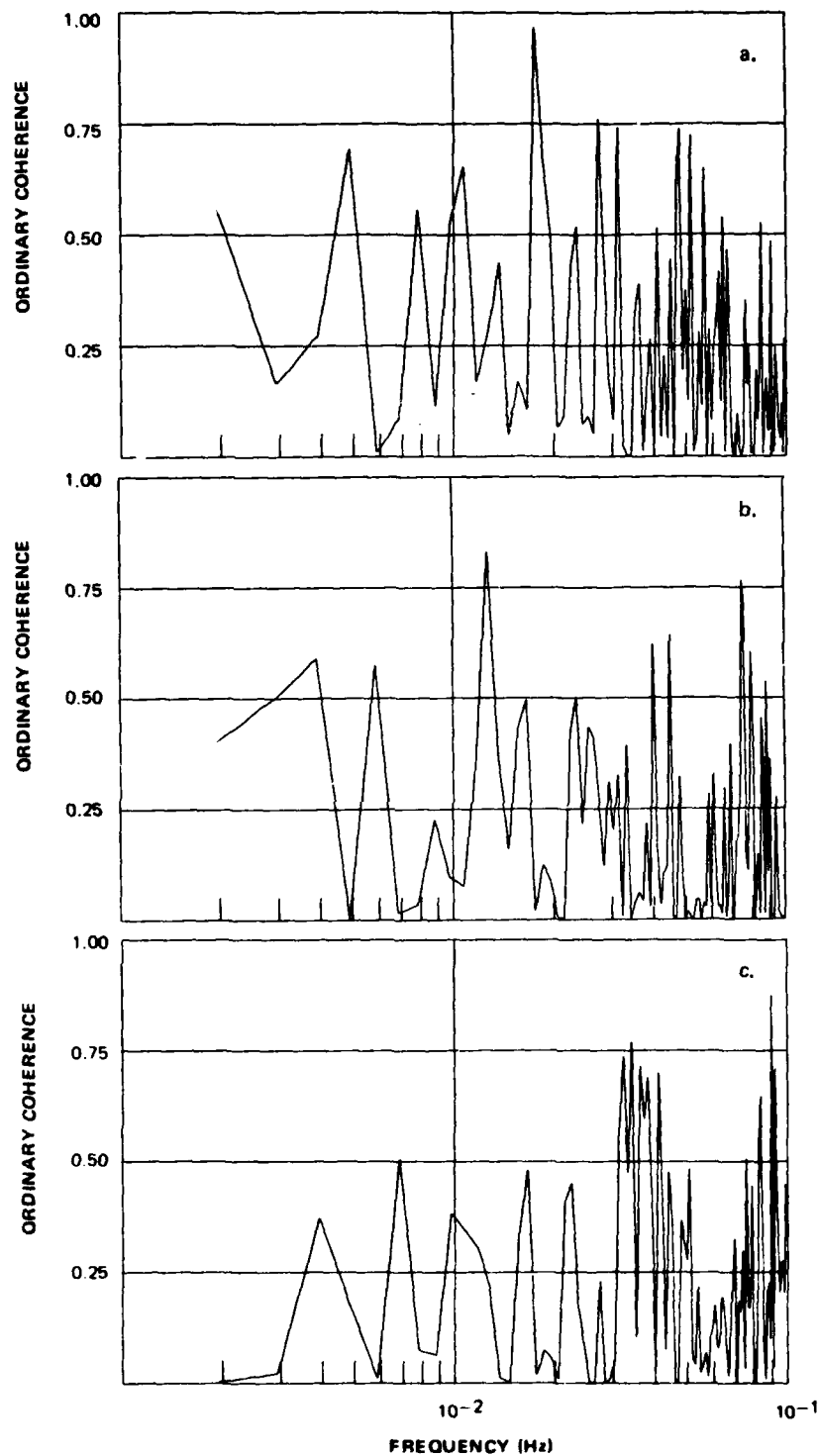


FIGURE 39. ORDINARY COHERENCE ESTIMATES FOR THE EL CHICHON ERUPTION 093-A BETWEEN PAIRS OF THE THREE SEISMOGRAM COMPONENTS: (a) VERTICAL AND RADIAL, (b) VERTICAL AND TRANSVERSE, (c) RADIAL AND TRANSVERSE. (5 BLOCK SAMPLE/75% OVERLAP)

G 12999

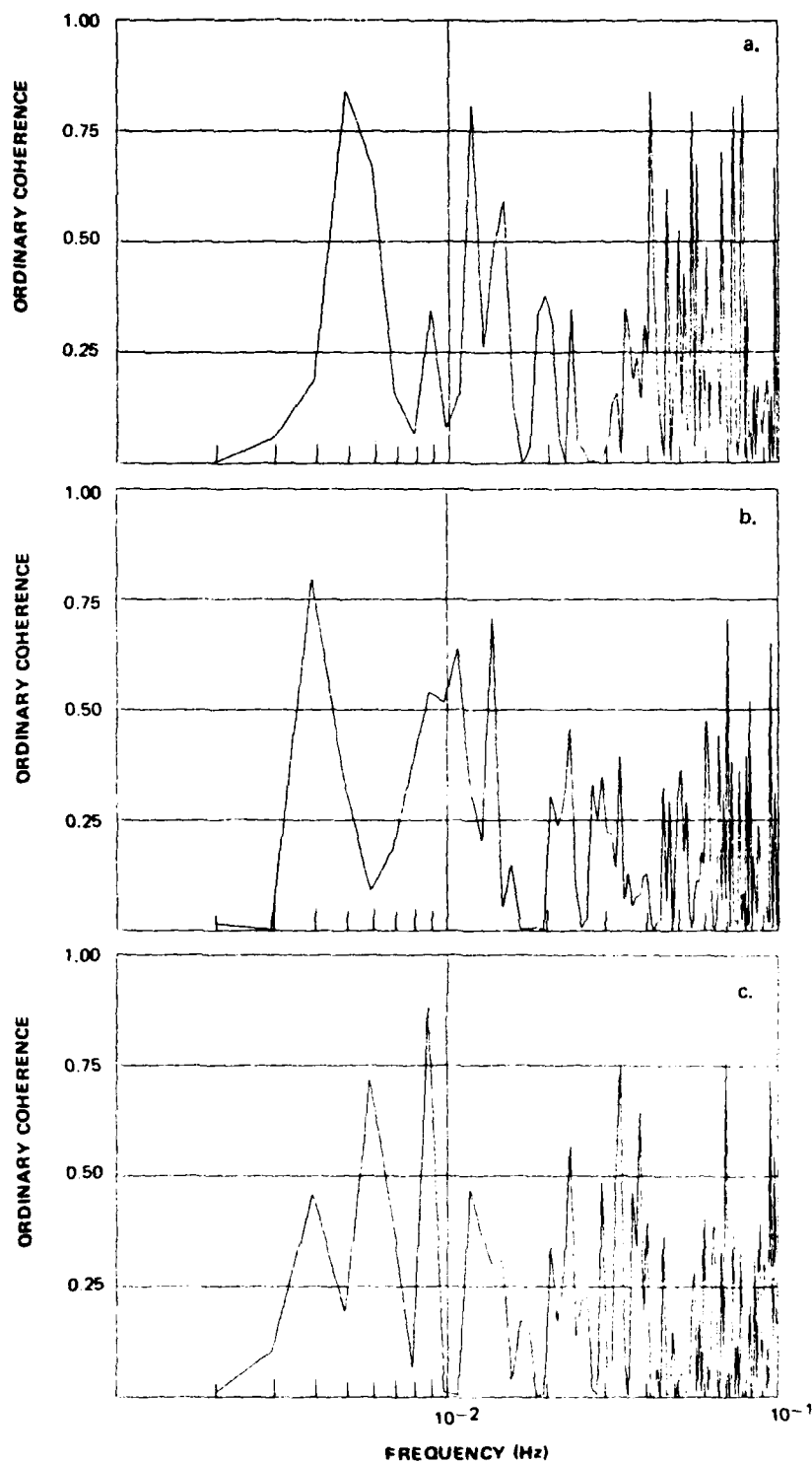


FIGURE 40. ORDINARY COHERENCE ESTIMATES FOR THE EL CHICHON ERUPTION 093-B BETWEEN THE MICROBAROGRAPH ARRAY BEAM AND THE VERTICAL (a), RADIAL (b) AND TRANSVERSE (c) SEISMOGRAMS. (5 BLOCK SAMPLE/75% OVERLAP)

G 13000

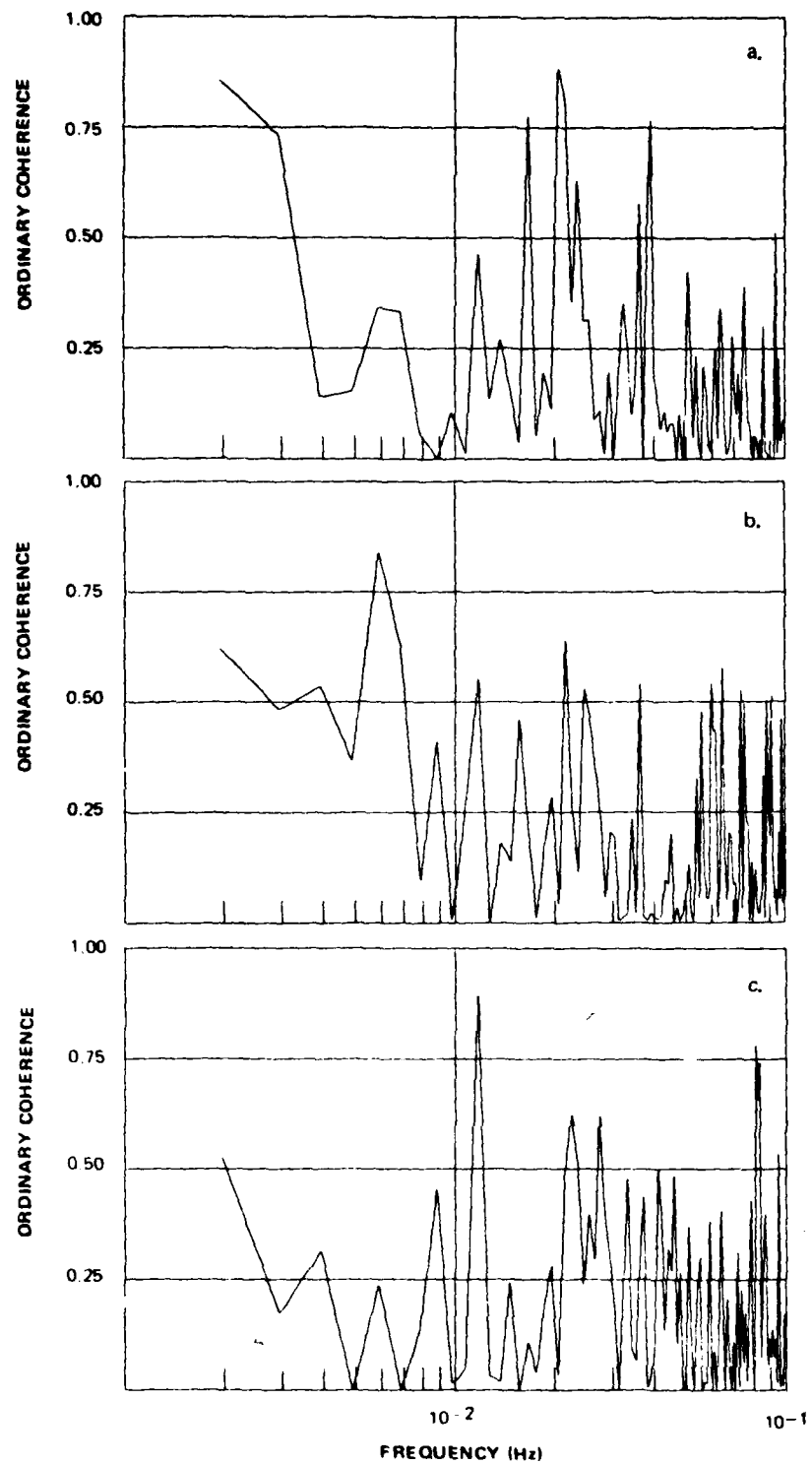


FIGURE 41. ORDINARY COHERENCE ESTIMATES FOR THE EL CHICHON ERUPTION 093-B BETWEEN PAIRS OF THE THREE SEISMOGRAM COMPONENTS: (a) VERTICAL AND RADIAL, (b) VERTICAL AND TRANSVERSE, (c) RADIAL AND TRANSVERSE. (5 BLOCK SAMPLE/75% OVERLAP)

G 13001

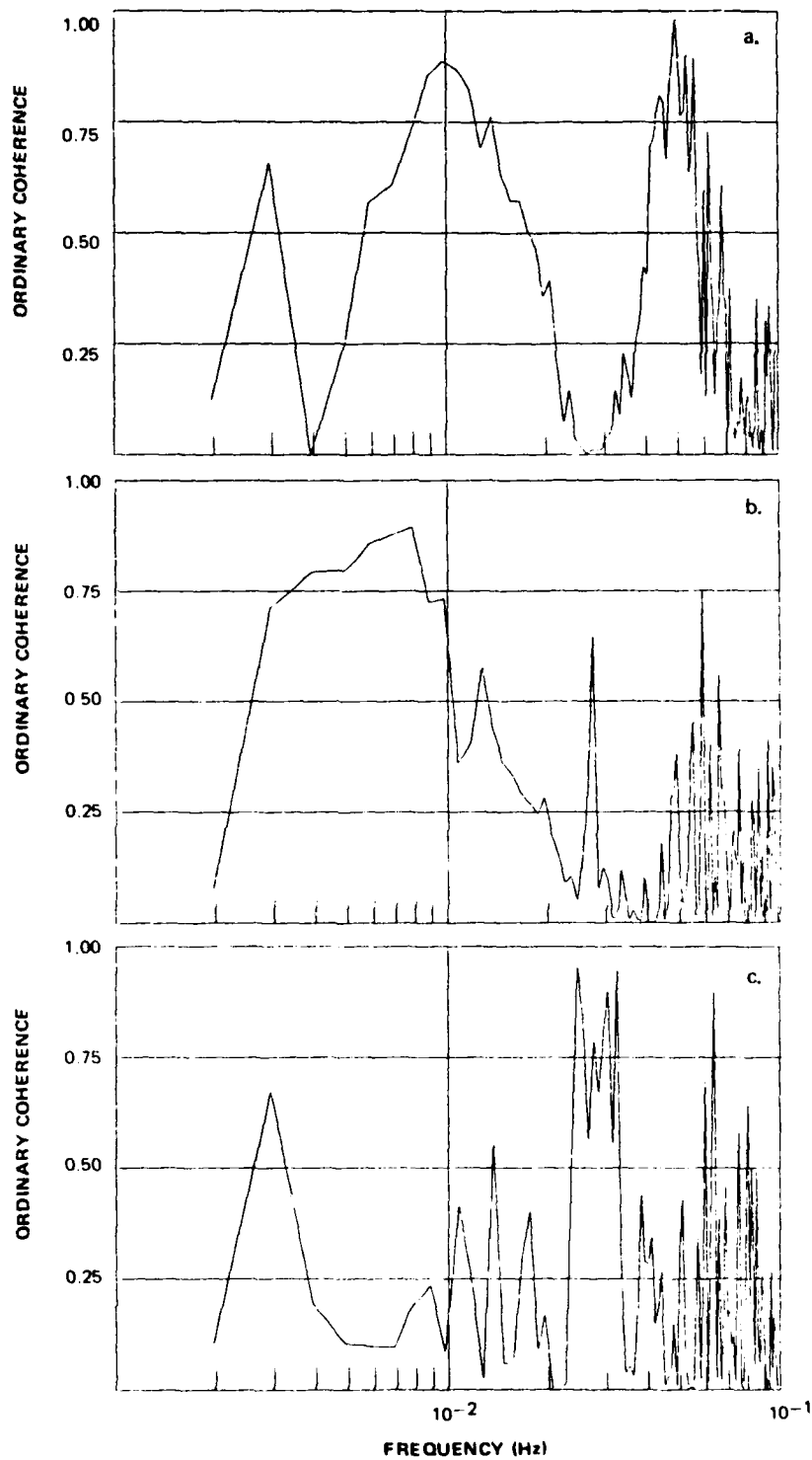


FIGURE 42. ORDINARY COHERENCE ESTIMATES FOR THE EL CHICHON ERUPTION 094-A BETWEEN THE MICROBAROGRAPH ARRAY BEAM AND THE VERTICAL (a), RADIAL (b) AND TRANSVERSE (c) SEISMOGRAMS. (5 BLOCK SAMPLE/75% OVERLAP)

G 13002

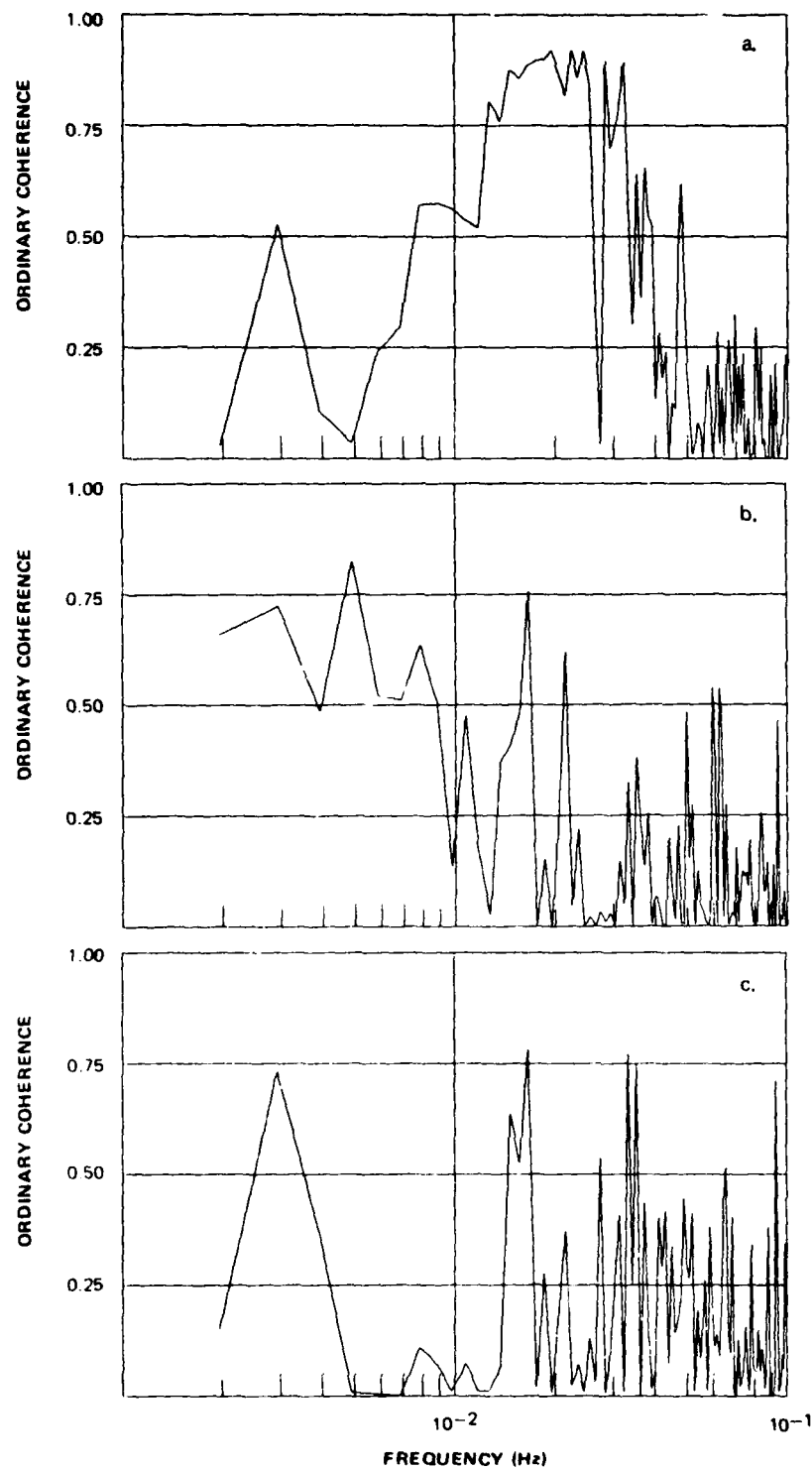


FIGURE 43. ORDINARY COHERENCE ESTIMATES FOR THE EL CHICHON ERUPTION 094-A BETWEEN PAIRS OF THE THREE SEISMOGRAM COMPONENTS: (a) VERTICAL AND RADIAL, (b) VERTICAL AND TRANSVERSE, (c) RADIAL AND TRANSVERSE. (5 BLOCK SAMPLE/75% OVERLAP)

G 13003

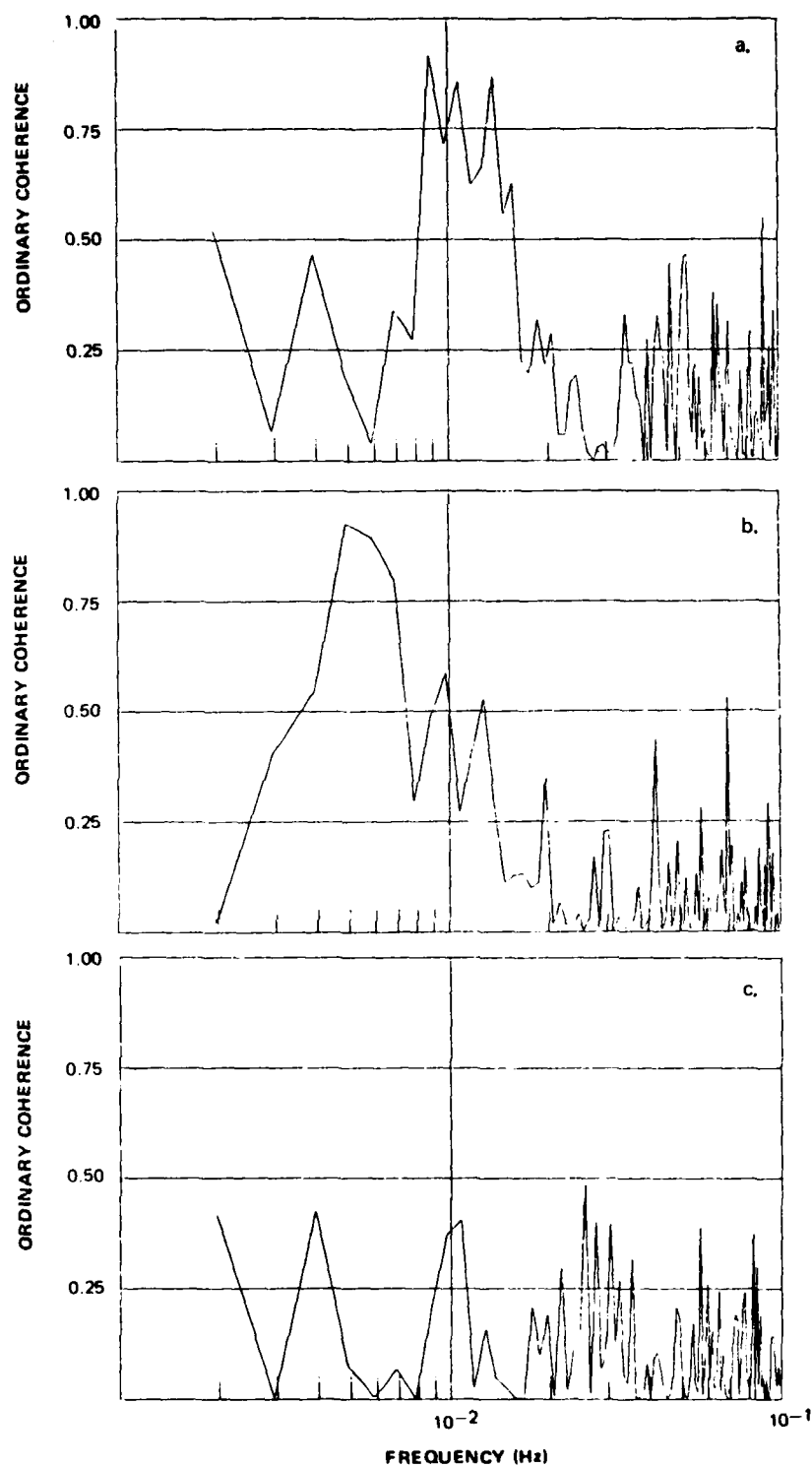


FIGURE 44. ORDINARY COHERENCE ESTIMATES FOR THE EL CHICHON ERUPTION 094-B BETWEEN THE MICROBAROGRAPH ARRAY BEAM AND THE VERTICAL (a), RADIAL (b) AND TRANSVERSE (c) SEISMOGRAMS. (13 BLOCK SAMPLE/75% OVERLAP)

G 13004

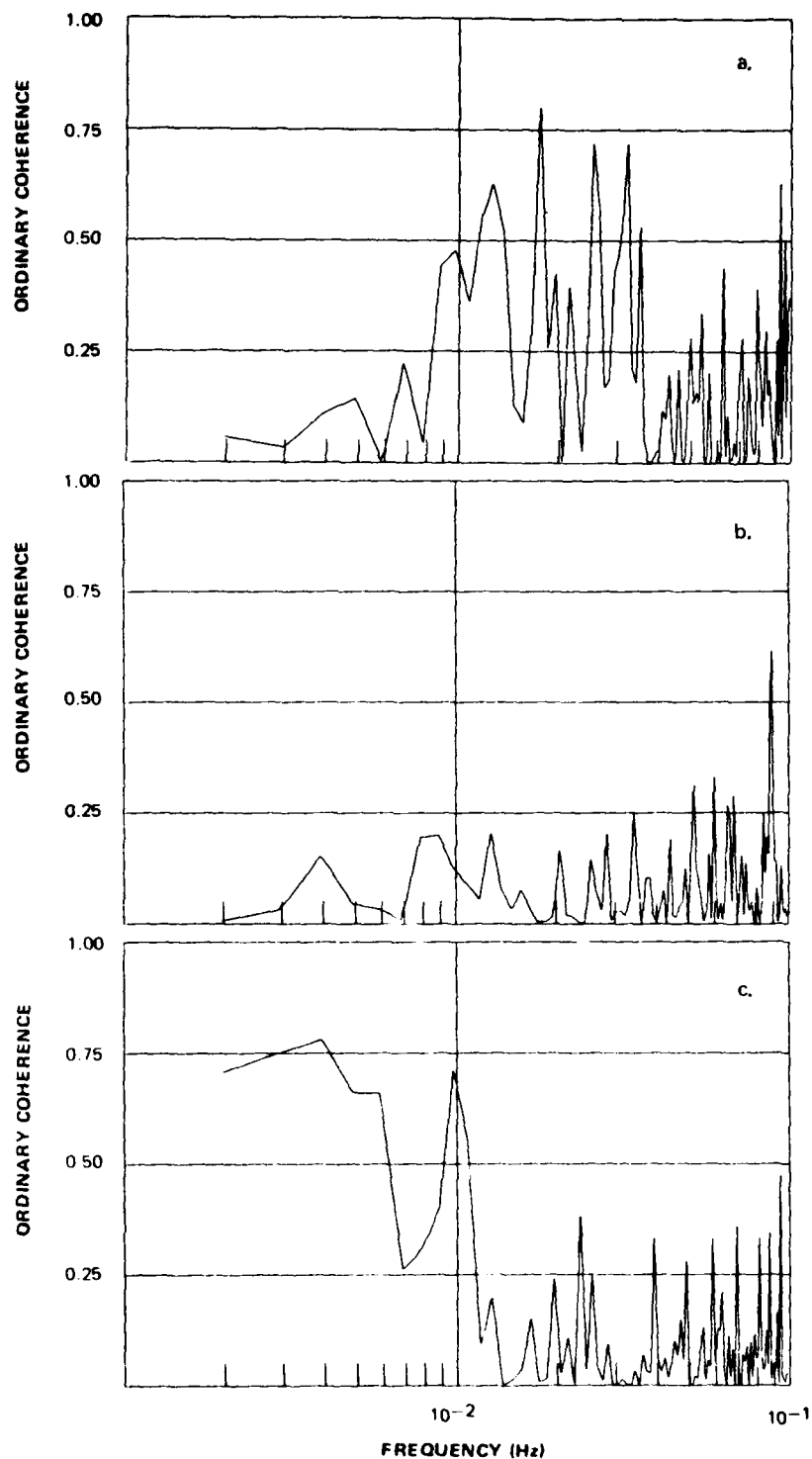


FIGURE 45. ORDINARY COHERENCE ESTIMATES FOR THE EL CHICHON ERUPTION 094-B BETWEEN PAIRS OF THE THREE SEISMOGRAM COMPONENTS: (a) VERTICAL AND RADIAL, (b) VERTICAL AND TRANSVERSE, (c) RADIAL AND TRANSVERSE. (13 BLOCK SAMPLE/75% OVERLAP)

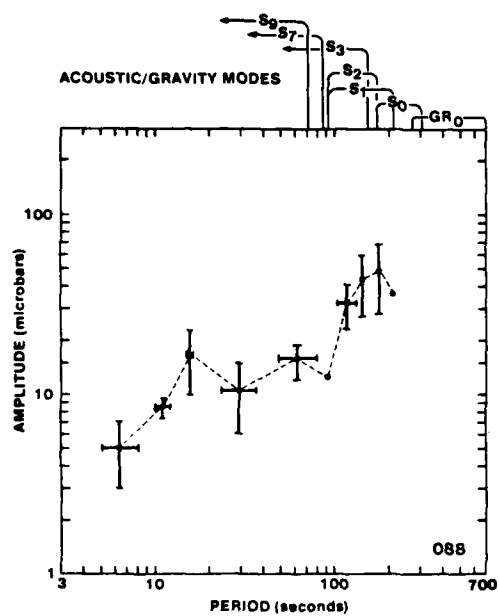
G 13005

Event No.	088			093A			Period (Seconds)
	Period (Seconds)	Amplitude (Microbars)	Phase	Period (Seconds)	Amplitude (Microbars)	Phase	
210 *		35.8	S ₀	312 *	81	GR ₀	180 ± 36
174		48.6 ± 20.5	S ₀ + S ₁ + S ₂	246 ± 66	60 ± 29.8	S ₀	63 ± 15
138		43.7 ± 16.8	S ₁ + S ₂ + S ₃	180 *	38 ± 4	S ₀ + S ₁ + S ₂	30 ± 6
117 ± 15		31.8 ± 9.2	S ₁ + S ₂ + S ₃	51 ± 3	6.6 ± 0.1	Sn n>3	7 ± 1
90 *		12.8	S ₂ + S ₃	27 ± 3	4.0 ± 0.1	Sn n>3	
63 ± 15		15.8 ± 4.3	Sn n>3	6	1.9 ± 3	Sn n>3	
30 ± 6		10.6 ± 4.3	Sn n>3				
15.5 ± 0.5		16.8 ± 6.4	Sn n>3				
11 ± 1		8.3 ± 1.2	Sn n>3				
7 ± 3		5.1 ± 2.1	Sn n>3				
174		48.6 ± 20.5	A ₁	312	81	A ₁	144
Duration A ₁ (minutes)			81			>81	

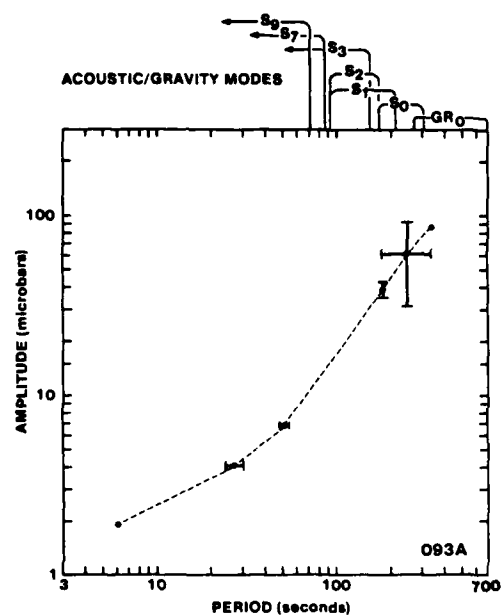
**Table 3. Amplitude and Period Measurements of Microbarometric Signals
from Five Eruptions of El Chichon Volcano**

093B			094A			094B		
Period (Seconds)	Amplitude (Microbars)	Phase	Period (Seconds)	Amplitude (Microbars)	Phase	Period (Seconds)	Amplitude (Microbars)	Phase
180 ± 36	17.3 ± 4.5	S ₀ + S ₁ + S ₂	276 *	104	GR ₀ + S ₀	348 *	165.2	GR ₀
63 ± 15	10.1 ± 0.6	Sn n>3	168 *	69	S ₀ + S ₁	225 ± 15	94.6 ± 21.4	S ₀
30 ± 6	4.8 ± 1.9	Sn n>3	71 ± 1	36 ± 8.9	Sn n>3	135 ± 9	60.2 ± 7.4	S ₁ + S ₂
7 ± 1	1.8 ± 0.6	Sn n>3	54 ± 6	27 ± 6.2	Sn n>3	99 ± 9	39.8 ± 11.2	S ₁ + S ₂ + S ₃
			37 ± 2	19 ± 7.3	Sn n>3	23 ± 1	15.4 ± 6.3	Sn n>3
			25 ± 5	12 ± 3.6	Sn n>3	15 ± 3	8.0 ± 6.5	Sn n>3
			7 ± 1	3 ± 2	Sn n>3	7 ± 3	4.5 ± 1.4	Sn n>3
144	22	A ₁	276	104	A ₁	348	165	A ₁
		26			30			>80

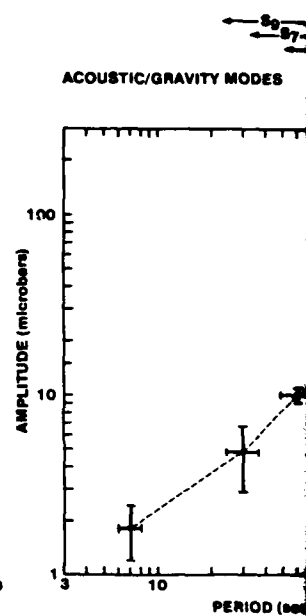
* Indicates single wave measurement



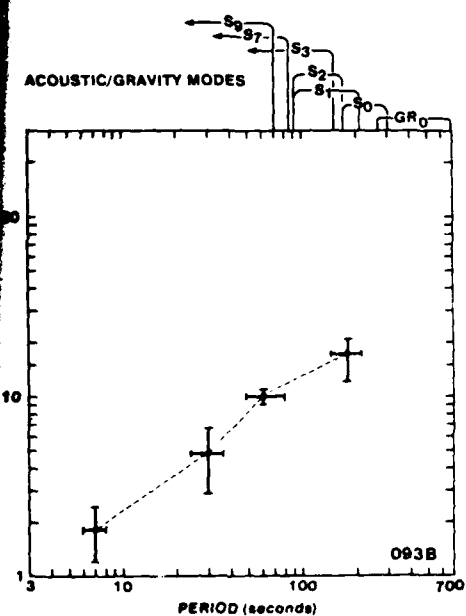
(a)



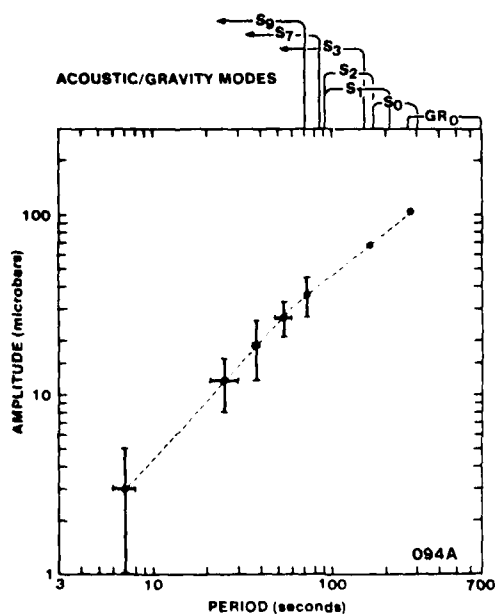
(b)



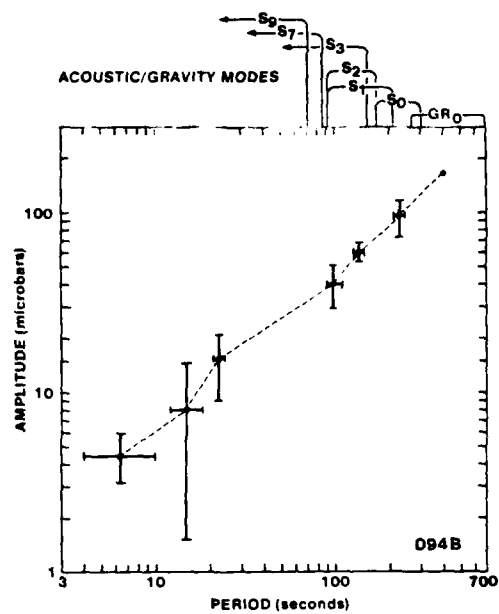
(c)



(c)



(d)



(e)

FIGURE 46. PERIOD AND PEAK-TO-PEAK AMPLITUDE (CORRECTED FOR INSTRUMENT RESPONSE) MEASUREMENTS OF ATMOSPHERIC GRAVITY/ACOUSTIC MODES EXCITED BY FIVE EXPLOSIVE ERUPTIONS OF EL CHICHON VOLCANO. MICROBAROMETRIC SIGNALS RECORDED AT MCKINNEY, TEXAS ($\Delta \approx 16.16^\circ$).

G 13026

-73/74-

TR 82-5

be a complex eruption with many injections into the plinian column over an extended period of time, all of the other eruptions display a logarithmic-linear relationship between period and peak-to-peak microbarometric amplitude with a slope nearly equal to one. Given the twenty amplitude-period measurements listed in table 3 (events 093A, 093B, 094A, 094B) for periods greater than fifteen seconds, a linear regression of the data pairs yielded an inverse frequency slope of 1.029 ± 0.277 at the 95% confidence level. This is an extremely good agreement between the observed and theoretically predicted relationship between microbarometric amplitude and wave frequency. All of the events have observable high-frequency ($T=5$ to 10 seconds), high-acoustic mode number waves which do not vary in amplitude by more than a factor of three, even though, from other observations (Silva, Cocheme, Canul, Duffield and Tilling, 1982; De La Cruz-Reyna, 1982; Harskov, De La Cruz-Reyna, Singh, Medina and Gutierrez, 1982), it is known that the difference in energy release between event 093B and 094B is at least two to three orders of magnitude. This suggests that the high-frequency data may be useful in analysis of event complexity, but the high mode number data will not be particularly sensitive as a yield determinant. On the other hand, there appears to be a reasonably clear relationship between the longest period, and therefore largest amplitude, wave in the A_1 train and the "magnitude" of the eruption. This hypothesis is supported by the sequence c, b, d, e of figure 46. Complex eruptions like that of 088 do not appear to follow this trend since it is known that the 088 and 094B events are of similar energy release. Since this data set is of limited extent, from a single distance and azimuth, additional analyses would be required to formulate a more definitive relationship among amplitude, period and distance. This will be discussed in greater detail in section 2.4.3.

The seismic period-amplitude data (corrected for instrument response) for the five eruptions of El Chichon are summarized in table 4 and illustrated in figures 47 (vertical) and 48 (radial). The peak-to-peak amplitudes are given in nanometers of displacement. The discussion of symbolism given previously for figure 46 also applies to these figures.

Comparing the five period-versus-amplitude graphs of the vertical component data (figure 47), it is apparent that the relatively well-behaved relationships between the microbarometric wave amplitudes and periods illustrated in figure 46 are not reproduced in the vertical component seismic data. All vertical component seismic data exhibit large amplitude noise contamination of the signals for wave periods shorter than forty to sixty seconds. The general shape of these displacement-amplitude spectra is similar to those illustrated by Fix (1972) for the vertical power spectra of ambient noise at a variety of sites. Thus, only at the long-period end of the observed vertical component spectra is there a sufficient signal-to-noise ratio to resolve infrasonic signal amplitudes with any confidence. From these data, there is a suggestion of an ω^{-2} relationship between wave frequency and amplitude as compared with the ω^{-1} relationship illustrated by the microbarometric data, as predicted by theory for a homogeneous isotropic half space.

The period-versus-amplitude relationship of seismically recorded infrasonic data is more apparent in the radial (figure 48) than the vertical (figure 47) components. Unlike the microbarometric data which displayed a definite

lengthening of the maximum measurable period in conjunction with the increase in amplitude as a function of source event energy release, the radial and vertical seismic data display only an increase in amplitudes of the observed waves. There appears to be a maximum wave period observed for all events, regardless of source dimension, of between 200 and 300 seconds. In fact, this is an observation limit imposed by the recording system. Wave periods longer than 200 seconds have so little amplification with respect to the center frequency of the McKinney recording system that the signal digital count begins to approach machine noise levels. Thus, it is likely that an extension to longer periods as a function of source dimensions as observed for microbarometric data also may exist for the seismic data. Because of instrumentation limitations, however, this period extension was not observed.

Given the twenty-six amplitude-period measurements listed in table 4 for radial component seismograms (events 093A, 093B, 094A, 094B), a linear regression of the data pairs (for periods greater than 24 seconds) yielded an inverse frequency slope of 2.86 ± 1.65 at the 95% confidence level. Theory predicts an inverse slope of three which is within the 95% confidence limit associated with these data. In fact, these data only fail correspondence with an ω^{-3} slope at a confidence level less than 50%.

There are several important conclusions to be drawn from these results. First, the infrasonic-acoustic signals observed for "simple" explosive eruptions of El Chichon volcano have microbarometric amplitude-versus-frequency spectra with slopes of nearly ω^{-1} . Second, all analytical microbarometric signals had high mode number infrasonic waves which were relatively the same amplitude and period regardless of significantly different source dimensions. GR_0 mode excitation occurred only with the largest explosions of the sequence, and both the amplitude and period of infrasonic waves in the period range of S_0 , S_1 and S_2 modes tended to decrease with reduction of source energy release. Third, the radial seismic signature of infrasonic signals displayed an approximate ω^{-3} slope between wave frequencies and amplitudes. Because there is an additional ω^{-2} dependency of the seismic signals compared with the microbarometric signals, the radial component seismograms should be more useful for yield or source dimension determination than the corresponding microbarograms.

In addition to the standard period-amplitude relationship, we have also examined using the moving window analysis technique (Landisman, Dziewonski, and Sato, 1969) to extract useful quantitative data about the infrasonic-acoustic signals. This analysis method results in contoured relative energy levels in a period-versus-velocity space. The input to the algorithm consists of the digital time series data and parameters such as the distance to the event, origin time, start time of the data string and filter characteristics. Because the exact origin time is uncertain, there is a comparable uncertainty in correctly locating the energy contours with respect to the velocity coordinate. Since the GR_0 and S_0 modes are essentially nondispersive, and the effects of wind shear on their propagation velocities are relatively well known (Pierce, 1966), the origin time can be adjusted until the energy lobe associated with these modes is best-fit to the appropriate velocity range. Through this procedure, the exact origin time can be approximated with relatively small error, and the relative velocities of the other modes can be

Event No.

088

093A

Vertical
Period (Seconds) Amplitude (Nanometers)

234 \pm 16 4520 \pm 480

105 \pm 10 1367 \pm 133

90 * 820

60 \pm 6 250 \pm 28

48 136 \pm 17

40 \pm 7 243 \pm 67

28 \pm 2 295 \pm 32

24 576 \pm 236

21 \pm 2 700 \pm 76

18 * 2002

Radial
Period (Seconds) Amplitude (Nanometers)

132 * 3758

126 * 19336

111 * 3056

68 \pm 4 433 \pm 65

32 \pm 5 193 \pm 59

Vertical
Period (Seconds) Amplitude (Nanometers)

210 \pm 40 460 \pm 140

186 \pm 14 673 \pm 127

63 265 \pm 85

55 \pm 5 162 \pm 34

35 \pm 2 111 \pm 25

27 \pm 3 296 \pm 86

18 \pm 2 744 \pm 217

Radial
Period (Seconds) Amplitude (Nanometers)

300 * 16141 \pm 3859

195 \pm 45 4573 \pm 2927

87 \pm 13 609 \pm 190

54 240 \pm 125

24 172 \pm 78

Vertical
Period (Seconds)

204 \pm 16

47

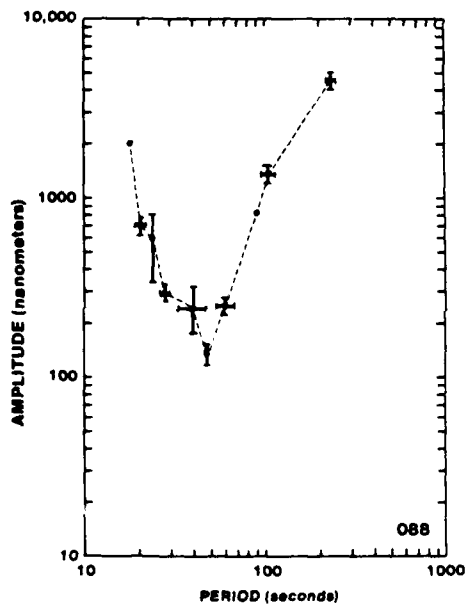
38 \pm 2

28 \pm 2

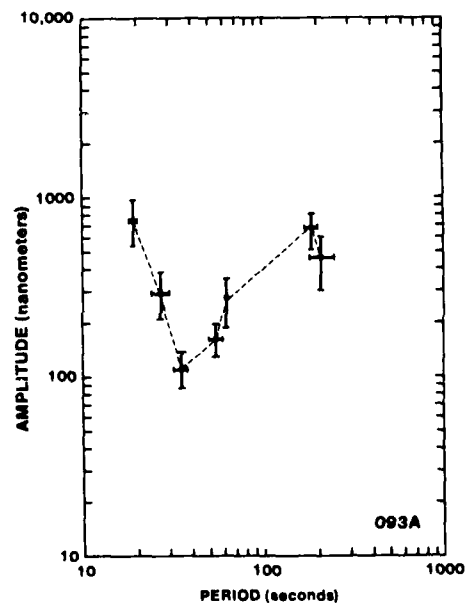
24 \pm 1

20 \pm 21

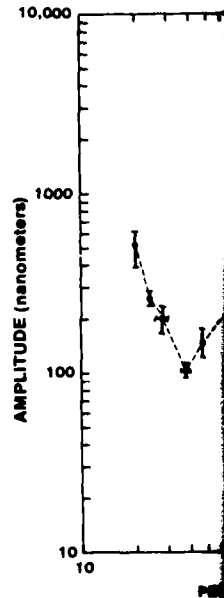
* Indicates single wave measurement

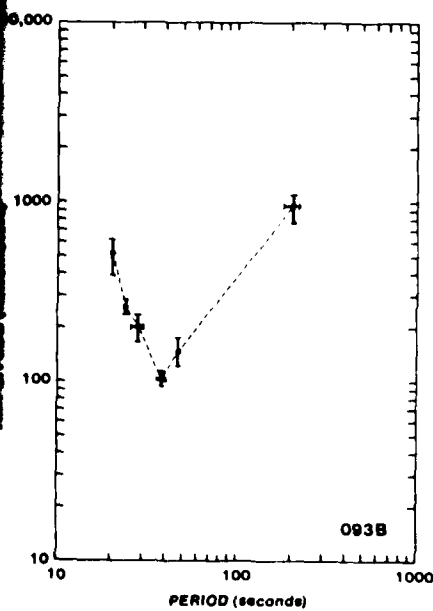


(a)

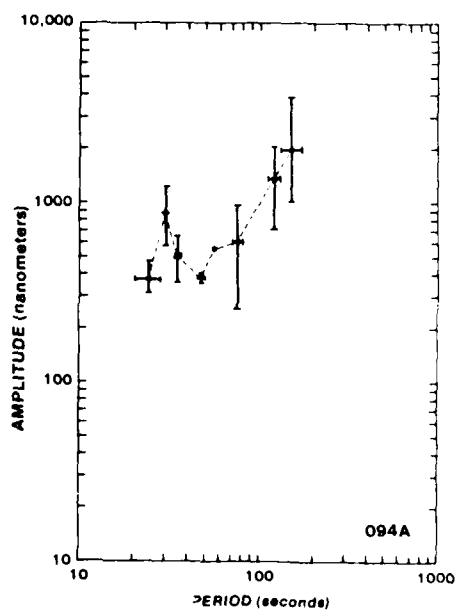


(b)

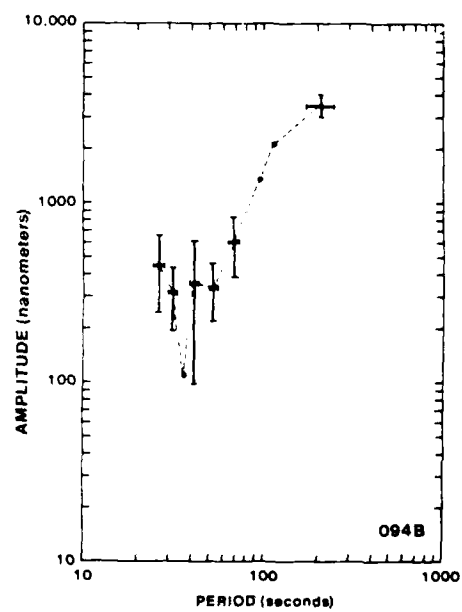




(c)



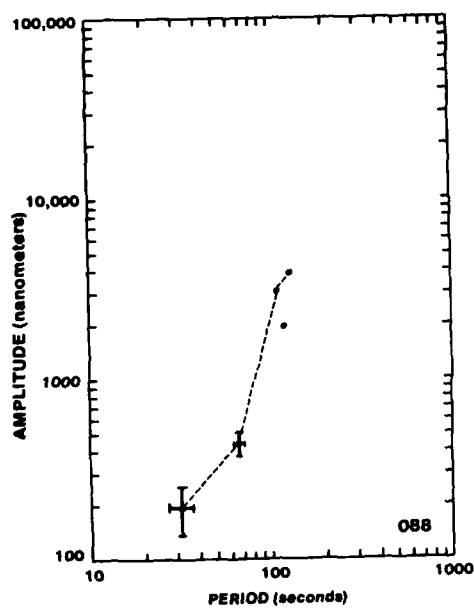
(d)



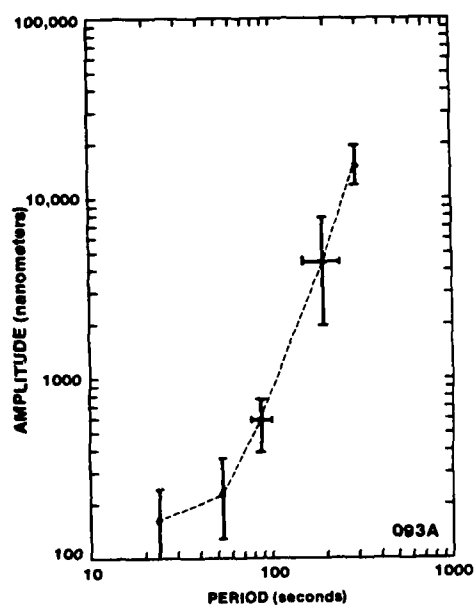
(e)

FIGURE 47. PERIOD AND PEAK-TO-PEAK AMPLITUDE (CORRECTED FOR INSTRUMENT RESPONSE) MEASUREMENTS OF ATMOSPHERIC GRAVITY/ACOUSTIC MODES EXCITED BY FIVE EXPLOSIVE ERUPTIONS OF EL CHICHON VOLCANO. LONG-PERIOD VERTICAL SEISMIC SIGNALS RECORDED AT MCKINNEY, TEXAS ($\Delta = 16.16^\circ$)

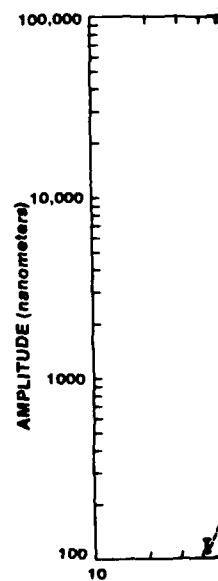
G 1304

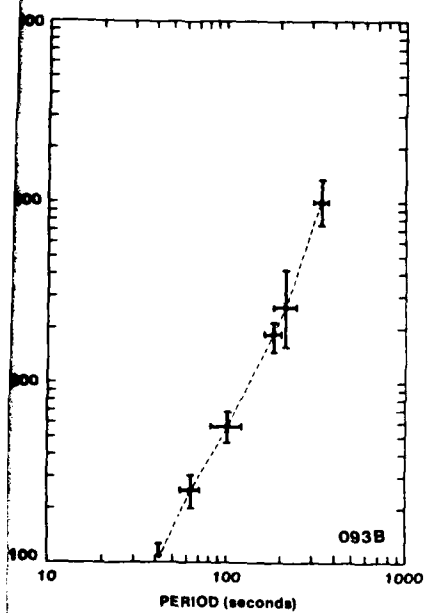


(a)

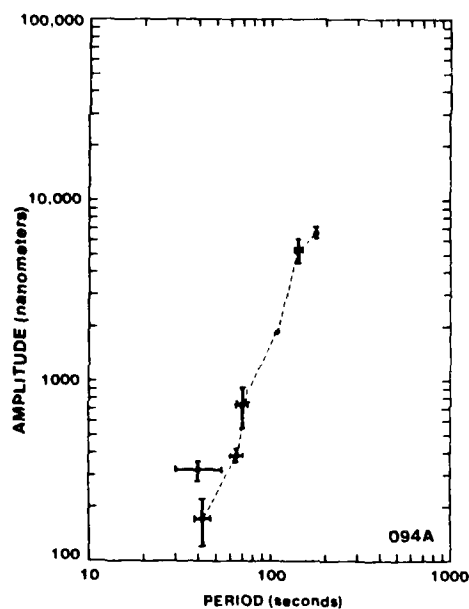


(b)

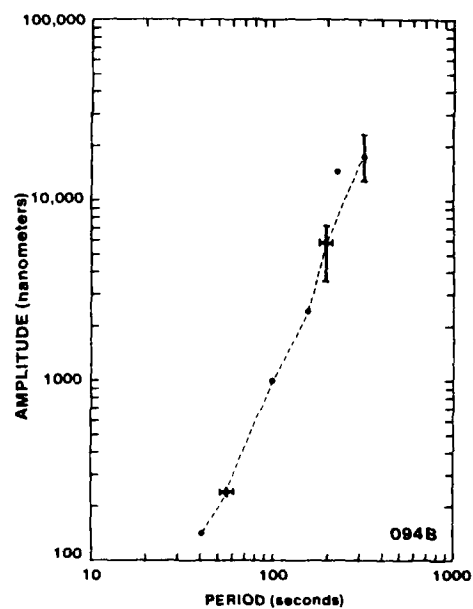




(c)



(d)



(e)

FIGURE 48. PERIOD AND PEAK-TO-PEAK AMPLITUDE (CORRECTED FOR INSTRUMENT RESPONSE) MEASUREMENTS OF ATMOSPHERIC GRAVITY/ACOUSTIC MODES EXCITED BY FIVE EXPLOSIVE ERUPTIONS OF EL CHICHON VOLCANO. LONG-PERIOD RADIAL SEISMIC SIGNALS RECORDED AT MCKINNEY, TEXAS ($\Delta = 16.16^\circ$)

G 13033

defined. Using this procedure, we have analyzed the microbarometric signal of event 093A (figure 22, red line). The results of these analyses are illustrated as figures 49 and 50. From the period-versus-amplitude study (figure 46b), it is known that the signal amplitude varies almost two decades over the period range covered by the A_1 time series train. Because the amplitude resolution of the moving window analysis is linear, plotting the entire spectral band results in contouring only the most prominent energy features. This is illustrated in figure 49. Enhanced resolution of the shorter period spectrum is possible by plotting only the period range below the major energy lobes. This is illustrated in figure 50.

An examination of figure 49 reveals one principal energy region centered approximately at a period of 290 seconds and a velocity of 310 meters/second. This corresponds well with the major energy feature of figure 46b which is the GR_0 and S_0 model frequency band. Interestingly, a second energy lobe at approximately the same period, but with mean velocity near 255 m/sec and one third the energy, is also apparent. This energy lobe may be the signature of the elusive GR_1 mode. Although this observed velocity difference between GR_0 and GR_1 is approximately equivalent to theoretical predictions, the calculations of Pierce (1966) indicate that the amplitude difference should be over an order of magnitude rather than a factor of three different. Two additional energy lobes with roughly one tenth the amplitude of the maximum occur at periods of 50 to 80 seconds and mean velocity 300 m/sec, and 80 to 200 seconds with mean velocity of 280 m/sec.

Figure 50 illustrates the energy distribution in the period range from five to one hundred seconds in greater detail. The hummocky topography of the energy in the period-velocity space of figure 50 is typical of discrete wave guiding rather than continuously dispersed propagation of waves. We conclude from this preliminary study that a wealth of information pertinent to yield determination may be embodied in moving window analyses of infrasonic-acoustic data. In particular, energy distribution in higher modes can be evaluated more exactly. This could be important for the design of optimum filtration schemes to enhance signal-to-noise ratios of marginally observable infrasonic-acoustic signals.

2.4.3 Estimation of Energy Release from the El Chichon Explosions

In the previous section, we demonstrated the comparable procedures of detecting and identifying infrasonic signals using seismic as well as microbarometric instrumentation. We have shown that for five explosive eruptions of El Chichon volcano, there is a well-defined ω^{-3} relationship between amplitude and period of infrasonic-acoustic waves recorded on radial component seismograms. Similar analyses of contemporaneous microbarograms yielded approximate ω^{-1} relationships. This supports strongly that radial-component, long-period seismograms may be utilized more effectively than microbarograms to determine yield of atmospheric nuclear weapons tests or, alternatively, energy release of volcanic explosions. Derivation of a reliable yield estimation procedure based on the current data is not possible because there are several important relationships for which robust limits have yet to be determined. In this section, we will examine several of these deficiencies and requirements to formulate a reliable yield estimator.

The principal obstacle to formulation of a yield determinant is insufficient data. Currently, there are no calibrated atmospheric nuclear weapons tests with which to reference observations of events with unknown explosivity. Volcanic explosions are relatively abundant sources of infrasonic-acoustic signals and have energy releases known to cover several orders of magnitude. Unlike thermonuclear devices, however, the mechanism of volcanic energy release is generally temporally complex and involves both thermal and mechanical energy components. For these reasons, it is difficult to estimate exact energy release, the coupling of total energy release to atmospheric perturbation, and, ultimately, the simplicity of the volcanic and nuclear detonation sources.

Fortunately, determination of volcanic explosivity has been one goal of volcanology for many decades, and there is a variety of techniques reported in the literature. A bibliography of selected references on volcanic explosivity, energy, and magnitude is included as appendix D of this report. Observations used to estimate volcanic energy release include measures of volume and areal dispersion of ejecta, phenomena related to airblast such as treefall, etc., and various aspects of plume rise. Most techniques reported to estimate energy release by volcanoes have relatively restricted application and rely on empirical observations without equivalent counterpart in atmospheric nuclear weapons tests. Nevertheless, these restricted techniques do provide alternative methods to estimate limiting energy release conditions and thus may assist in ultimate scaling of nuclear weapons tests. Currently, there is no quantitative volcanic explosivity scale correlative with the Richter earthquake magnitude scale. The volcanic explosivity index (VEI) of Newhall and Self (1982) (table 2, this report) is an attempt to qualify volcanic eruptions and is similar to an earthquake Mercalli intensity scale. Like the Mercalli intensity scale, however, the VEI has generally defined arbitrary limits for many unrelated phenomena and, none of the "quantitative" limits can be related explicitly to either total energy or energy release rates in conventional units. The reason for this is obvious: there are few instrumental measurements, particularly far field, which are included in this explosivity scale. In fact, the far-field measurement of infrasonic-acoustic wave trains may prove to be the most useful technique to evaluate volcanic

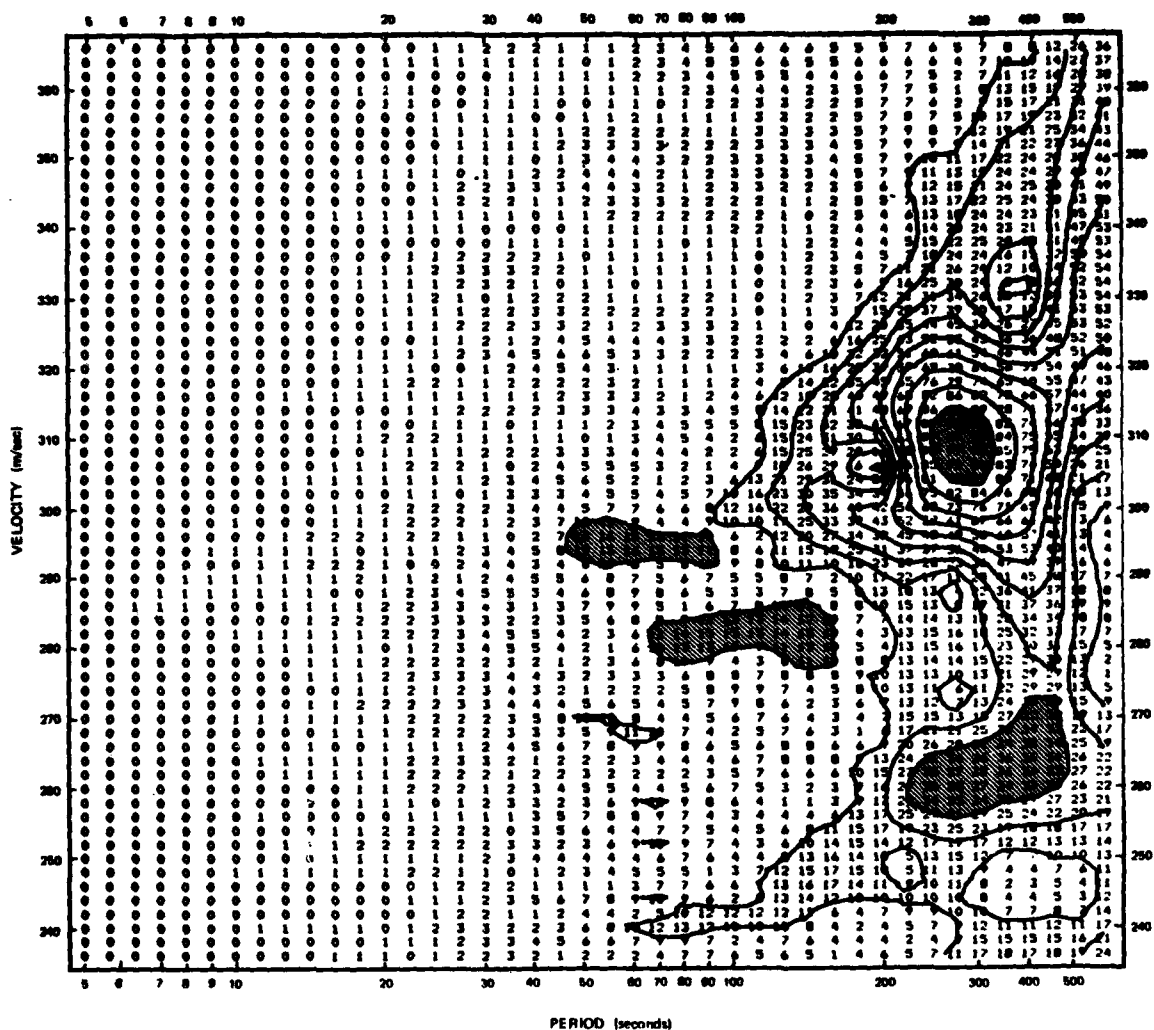


FIGURE 49. MOVING WINDOW ANALYSIS OF THE MICROBAROMETRIC A₁ WAVE TRAIN FROM THE 093A ERUPTION OF EL CHICHON VOLCANO. REGIONS OF THE PERIOD (5-500 SECONDS) VERSUS VELOCITY (240-360 m/SEC) SPACE CHARACTERIZED BY LOCAL POWER MAXIMA ARE SHADED FOR CLARITY.

G 13072

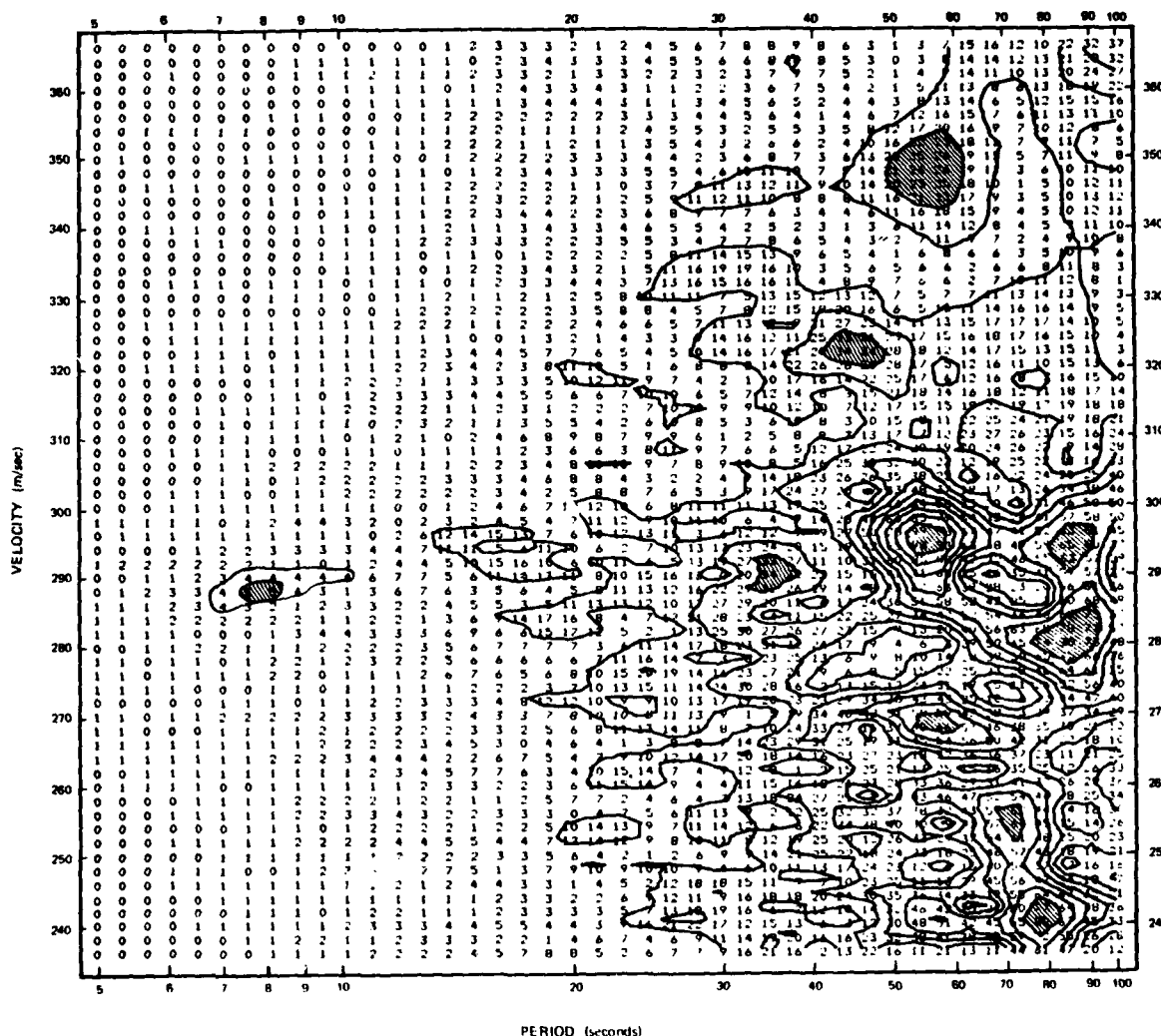


FIGURE 50. MOVING WINDOW ANALYSIS OF THE MICROBAROMETRIC A_1 WAVE TRAIN FROM THE 093A ERUPTION OF EL CHICHON VOLCANO. THE PERIOD RANGE HAS BEEN RESTRICTED FROM 5 TO 100 SECONDS TO ENHANCE THE RELATIVE POWER DETAILS OF FIGURE 49. REGIONS OF THE PERIOD VERSUS VELOCITY SPACE CHARACTERIZED BY RELATIVE LOCAL POWER MAXIMA ARE SHADED FOR CLARITY. SEE TEXT FOR ADDITIONAL DISCUSSION.

G 13073

explosive energy in a repeatable robust manner once proper scaling has been achieved.

Given the state-of-the-art quantification of volcanic explosivity, one of the most useful measurements currently made is the height of the volcanic eruption cloud. Factors governing eruption column height have been discussed by Briggs (1969), Settle (1976, 1978), Wilson (1976), Wilson et al (1978, 1980), Kienle and Shaw (1979), Wilson (1980), and Sparks and Wilson (1982).

Factors such as vent diameter, ejecta velocity and fragmentation (mass flux), eruption duration, atmospheric thermal stratification, wind shear, latitude and elevation have been demonstrated to be important in controlling ultimate cloud height of nonsubmarine eruptions. Although these factors blend both thermal and kinetic energy, it has been shown that total plume height is dominated ultimately by thermal convective rise (Wilson, 1976; Settle, 1976, 1978). Since energy release from surface-located atmospheric thermonuclear detonations also result in plumes dominated by thermal convective rise, analyses of plume heights from short-duration volcanic explosions may provide an independent, useful measure of energy release which is applicable to estimation of nuclear test yields. Because the source dimensions and dynamics of volcanic explosions and nuclear weapons tests are vastly different, however, an energy estimation of one based completely on the data of the other can never be fully satisfactory. It is the proverbial comparison of apples and oranges.

Given the preceding precautionary note, we will assign an energy estimation for the El Chichon explosions based on observed plume heights. Assuming that these estimates are approximately correct and that the eruptions are reasonable facsimiles of surface-based atmospheric nuclear weapons tests, we will estimate the threshold yields which may be discriminated with far-field, infrasonic-acoustic data. These extrapolated conclusions are based on very little data. A scheme for reliable estimation of yield would require a more extensive and robust treatment.

Settle (1978) has shown that the maximum height attained by volcanic eruption clouds is directly correlated with the mass flux rate of the volcano when the data are corrected for known controlling factors. Given a mass flux rate, it is relatively simple to estimate a kinetic energy rate, which if integrated for a specified period of time, yields an eruptive kinetic energy. Figure 51 illustrates a graph of eruption kinetic energy versus maximum eruption cloud height. Several sets of data have been incorporated in this illustration. The maximum cloud heights and estimations of kinetic energy release from six volcanic eruptions derived from Settle (1978) are illustrated as solid circles. The kinetic energy estimations were computed from the reported kinetic energy rate by integrating the kinetic energy flux for sixty seconds. Although this integration time constant is arbitrary, it was used assuming that the major drive to most explosive eruptions occurs within the first minute of eruption. Near-field observations of eruptions like that at Mount St. Helens on 18 May 1980 certainly support this hypothesis. Estimations of kinetic energy release and maximum cloud height for three eruptions of Mt St. Helens, which were taken from USGS Professional Paper 1250, are illustrated as solid triangles on figure 51. The kinetic energy release of the 18 May

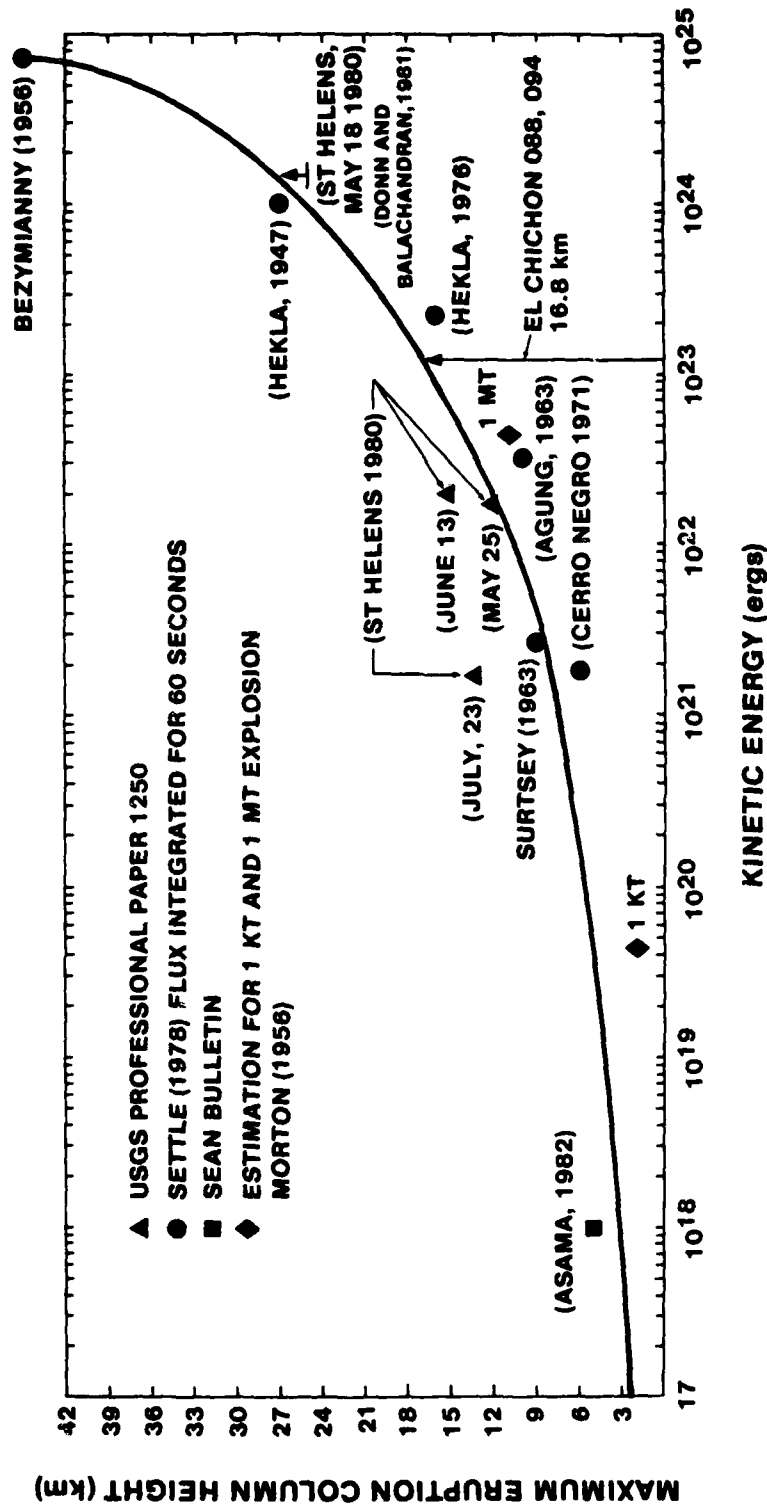


FIGURE 51. ERUPTION CLOUD HEIGHT VERSUS KINETIC ENERGY

G13160

1980 Mount St. Helens eruption is from Donn and Balachandran (1981) and the corresponding cloud height is from the USGS Professional Paper 1250. The maximum cloud height attained by this eruption is unknown because it exceeded the lidar observation limit of 25 kilometers. This eruption is symbolized on figure 51 as an arrow truncated at the 25 kilometer cloud height. One observation from Mount Asama of kinetic energy and cloud height, which is taken from the Smithsonian SEAN Bulletin, is illustrated as a solid square on figure 51. Finally, using the formula of Morton (1956), we have calculated the atmospheric perturbation heights for an equivalent one kiloton and one megaton impulsive explosion. These are illustrated as solid diamonds. A curve fitting these data is relatively well constrained for events with energy releases greater than 10^{21} ergs. The functional relationship between cloud height and kinetic energy is poorly constrained for energy release less than 10^{21} ergs.

The maximum cloud height attained by the 088 and 094B eruptions of El Chichon were reported to be 16.8 kilometers based on lidar observations and satellite images. Utilizing the relationship of figure 51, this would yield an energy release between $1 * 10^{23}$ and $2 * 10^{23}$ ergs. Similarly, a cloud height of 3.6 kilometers, reported for the smaller eruptions would suggest an energy release in the neighborhood of 10^{19} ergs. Although the energy release of the larger events seems approximately correct, the energy estimation for the smaller events appears to be too low by at least an order of magnitude.

Comparing these energy estimations with observations made during the era of atmospheric nuclear weapons tests also suggests that these energy estimations are approximately correct. It is known from observations of infrasonic waves generated by atmospheric nuclear detonations that excitation of GR_0 modes occurred only for devices with yields exceeding one megaton (Al Bedard, personal communication). Since the 094B El Chichon explosion excited a GR_0 mode wave (see figure 46e), it is obvious that the yield-equivalence exceeded one megaton. The 093A and 094A events were both marginally into the GR_0 mode range and likely were in the high hundreds of kilotons to low megaton yield range. The 093B event, however, not only did not excite GR_0 oscillations, but barely excited oscillations in the low S_0 mode range. Thus, it is likely that this explosion was less than 100 kT yield-equivalence.

Observations of maximum amplitude A_1 microbarograph signals from a 58-megaton weapons test at Novaya Zemlya on 30 October 1961 also offer some insight into the yield-equivalence problem. These data were examined by a number of investigators (Wexler and Hass, 1962; Harkrider, 1964) to determine attenuation characteristics of infrasonic-acoustic waves. The results of Wexler and Hass are illustrated as figure 52 and indicate that a fifty-eight megaton explosion generated a maximum A_1 train signal of 2213 microbars at a distance of 16° . The maximum amplitude oscillation of the A_1 wave train from the 094B El Chichon explosion was 165 microbars at 16° . If the 094B event is scaled for yield-equivalence from these data, it is 4.5 MT. This yield seems approximately correct for the 094B event. However, when this method is used to approximate the yield of the 093B event, it results in a yield-equivalence of 446 kT which seems to be an overestimation by possibly an order of magnitude.

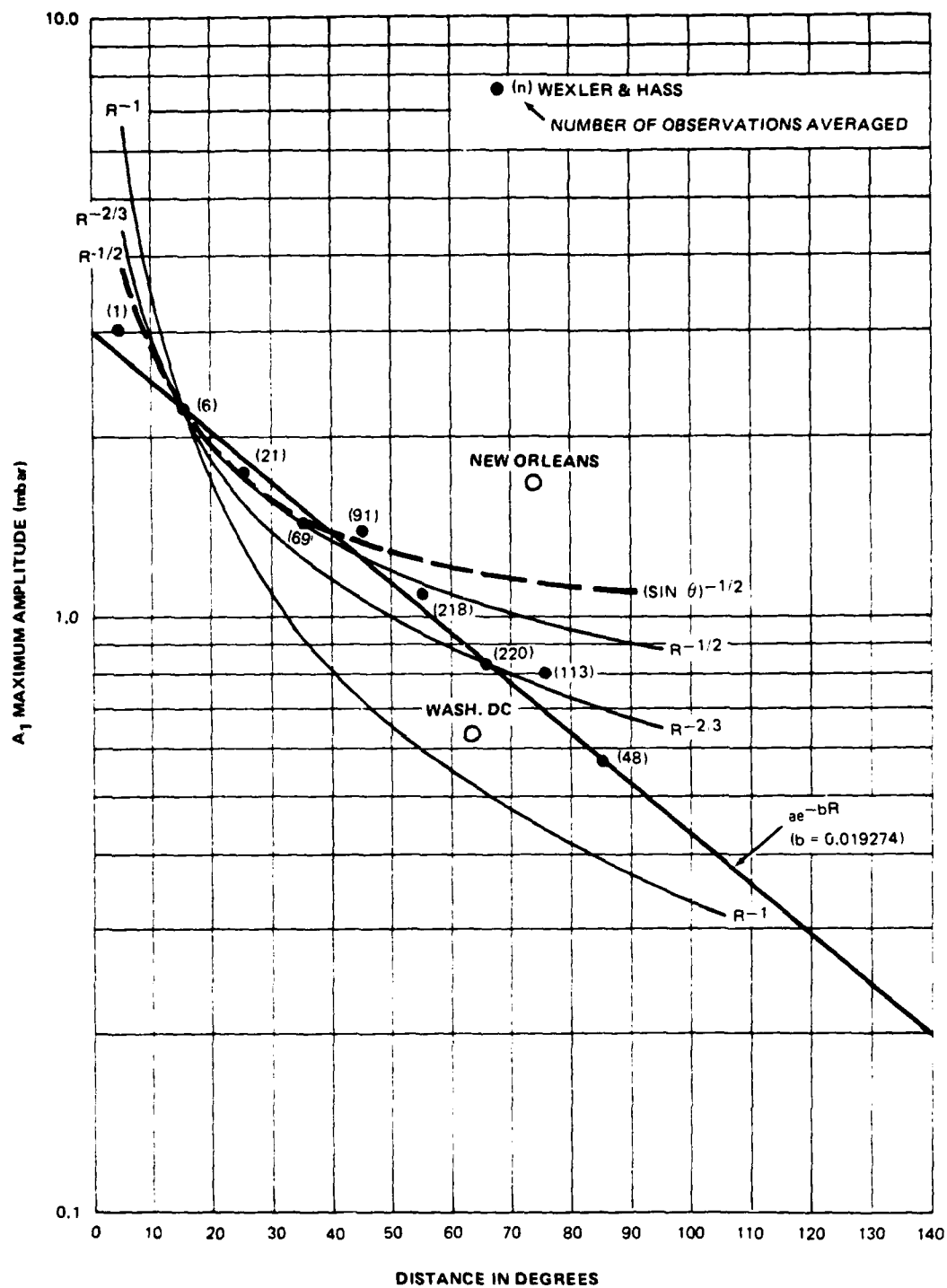


FIGURE 52. RELATIONSHIP BETWEEN THE MAXIMUM AMPLITUDE OF INFRASONIC-ACOUSTIC A₁ WAVE TRAIN AND DISTANCE. THEORETICAL ATTENUATION CURVES ARE FOR THE RELATIONSHIPS OF WEXLER AND HASS (1962) (SOLID); HARKRIDER (1964) (DASHED); AND THREE INVERSE DISTANCE RELATIONSHIPS $R^{-1/2}$, $R^{-2/3}$, R^{-1} . OBSERVED DATA ARE FOR THE 30 OCTOBER 1961 NOVAYA ZEMLYA 58 MT WEAPONS TEST (FROM WEXLER AND HASS)

Utilizing the recorded infrasonic-acoustic data, it is possible to estimate the energy release of the El Chichon explosions from a formulation of Posey and Pierce (1971).

$$E = 13P [R \sin (\frac{\Delta}{R})]^{1/2} H (cT)^{3/2}$$

where:

E = Energy in ergs

P = Amplitude (peak-trough) of pressure change in microbars

R = Radius of earth (6.371×10^8 cm)

Δ = Great circle distance (source-receiver, cm)

H = Atmospheric scale height (8×10^5 cm)

C = Velocity of observed wave (cm/sec)

T = Period of observed wave (seconds)

Following the Wexler and Hass methodology of using the largest amplitude wave of the A_1 train (i.e., the largest period observable), the energy releases for the five explosions of El Chichon were computed and are listed in table 5. For comparison, the energy release from the Mt. St. Helens 18 May 1980 eruption is also given in table 5. Energy estimations based on microbarometric and radial mode seismic data are included. Note the close correspondence of the energy releases estimated for events 093A, 094A and 094B to those estimations previously mentioned. Also note the reasonable agreement between the estimations based on microbarometric and seismic data. Although the energy of the 093B event is estimated by this method to be 4.2×10^{21} ergs, it is likely an overestimation. The reason for this overestimation, like the Wexler and Hass method, is that the methods both were formulated to use the nondispersive GR_0 and SR_0 modes. It is unlikely that the higher acoustic modes attenuate in a similar manner to these longer period modes and so, strictly speaking, the formula of Posey and Pierce (1971) likely is not applicable.

In conclusion, these estimations of energy release by the El Chichon explosions suggest that the yield threshold for these observations is likely in the range of a few tens of kilotons. Further, SK_0 derived estimations are within a factor of 2-4 of the equivalent microbarometric data derived estimations. Additional analyses will be necessary to improve these capabilities.

TABLE 5. ENERGY AND EQUIVALENT YIELD ESTIMATIONS FOR
THE EL CHICHON EXPLOSIONS

<u>Number</u>	<u>Event Code</u>	<u>Microbarograph Energy</u>	<u>~ Yield *</u>	<u>Radial SRO Seismograph</u>
1	088	1.10×10^{22}	259.5 KT	-
2	093A	4.49×10^{22}	1.06 MT	3.79×10^{22}
3	093B	4.20×10^{21}	99.5 KT	6.12×10^{21}
4	094A	4.79×10^{22}	1.14 MT	1.58×10^{22}
5	094B	1.08×10^{23}	2.6 MT	4.92×10^{22}
6	Mt. St. Helens (Donn and Balachandran, 1981)	1.48×10^{24}	35.0 MT	

* assumes 1 KT = 4.22×10^{19} ergs

3. SUMMARY CONCLUSION AND RECOMMENDATIONS

The primary goal of this research program has been to assess the capability of detecting and analyzing infrasonic signals recorded by three-component, long-period seismograph systems. Accomplishment of this goal required installation and operation of a collocated standard microbarograph array and three-component KS-36000 (SKO) seismograph system to provide data with which to make a meaningful comparison. A discussion of the data acquisition task of this program has been given in section 2.2. During the performance period, we examined the relative effects of the ambient noise fields on discrimination of infrasonic-acoustic signals recorded microbarometrically and seismically. A discussion of this aspect of the research is summarized in section 2.3. Based on the results of these analyses, we have made several conclusions about the relative infrasonic signal discrimination capabilities of standard microbarometric recording versus seismic recording methods.

During times characterized by low wind conditions, the microbarograph system has a better signal-to-noise ratio for the spectral region from 0.001 hertz to 0.1 hertz than does the vertical component seismograph. During times characterized by moderate to high wind conditions, however, the vertical component seismograph has a significantly better signal-to-noise ratio than does the microbarograph. High-amplitude microseismic storms periodically can obfuscate infrasonic signals recorded only on seismograph systems; and, although low-pass, prediction error, and t-k filtering can reduce this interference, there may not be sufficient post-filtration digital count resolution to discriminate infrasonic signals.

In addition to noise field analyses, we had the opportunity to study infrasonic-acoustic signals generated from several sources. Of these, the two most important were the Millrace detonation and an explosive-eruption sequence from El Chichon volcano. The infrasonic signal generated by the Millrace explosion was not capable of being discriminated from the ambient noise on either the seismic or the microbarometric digital records. This is an important result because it establishes one observation threshold limit. On the other hand, five explosive eruptions of El Chichon volcano were recorded well on both the seismic and microbarometric records.

Comparison of the signals recorded on the seismograph system and the microbarograph array has demonstrated extremely good agreement between the theoretical and observed vertical mode earth response function in the frequency band from 0.1 hertz to 0.001 hertz. On the other hand, the observed radial mode earth response function is a factor of five larger than was theoretically predicted. The exact cause of this discrepancy has not been determined. If this specific case is generally valid, then the resolution of infrasonic signals on radial mode seismograms is significantly better than was thought previously.

Additional analyses of the infrasonic signals from the El Chichon explosive eruptions are discussed in section 2.4. The results of these analyses indicate that "size" of the eruptions varied considerably, and certain conclusions about the characteristics of the associated infrasonic signals have been drawn. In general, there are linear relationships between amplitudes and periods of waves constituting the A_1 signals on both the microbarograph and seismograph records. The slopes of the amplitude-versus-period relationships are approximately ω^{-1} and ω^{-3} for the microbarograph and radial seismograph records respectively. As the intensity of the source increases, there is an increase in the longest period observed. All observed explosions had high acoustic-mode number waves in the A_1 wave trains. The amplitudes of the high mode number (high-frequency) waves were relatively constant, even though the "magnitudes" of the explosions varied by at least two orders of magnitude. Although these high-frequency waves were useful for examining temporal complexity of the source function, we concluded that they are not useful for determining yield.

Because these explosions produced signals which varied considerably in their signal-to-noise ratios, it would be useful to know what their yield-equivalent energy release was. The two event extremes were the 093B and the 094B explosions.

Attempts to assign yield-equivalences to these events have demonstrated the need to develop such a capability for small yield explosions which currently does not exist. Utilizing a variety of techniques which are discussed in section 2.4.3, we suggest that the yield-equivalence of the largest explosion (094B) is approximately two to four megatons. On the other hand, the yield-equivalence of the smallest explosion studied (093B) is approximately twenty to ninety kilotons. If the dimension of this latter event is correct, then the yield of the smallest explosion resolvable is in the neighborhood of a few tens of kilotons. Because of the large uncertainties involved in these calculations, however, these limits must be regarded with caution. We recommend that significant additional research be conducted using both historical atmospheric nuclear explosion data and current volcanic explosion data to reduce these uncertainties and formulate a more robust yield estimation technique.

4. REFERENCES

- Blackburn, E. A., Wilson, L., and Sparks, R. S. J., (1976), Mechanisms and dynamics of strombolian activity, Jour. Geol. Soc. London, 132, pp. 429-440.
- Briggs, G. A., (1969), Plume Rise, U.S.A.E.C. Critical Review Series, NTIS Report No. TID-25075, 81p.
- Chimonas, G. and Hines, C., (1979), Atmospheric Gravity waves launched by auroral currents, Planet Space, Sci., 18 00. 565-582.
- Daniels, F., (1959), Noise-reducing line microphone for frequencies below 1 cps, Jour. Acoust. Soc. Amer., 31, pp 529-531.
- De La Cruz-Reyna, S., (1982), The March-April, 1982 eruption of El Chichon volcano, Chiapas, Mexico, EOS, 63, p. 1126 (abstract).
- Donn, W., and Balachandran, N., (1981), Mount St. Helens Eruption of 18 May 1980: Air Waves and Explosive Yield, Sci., 213, pp 539-541.
- Fix, J. E., (1972), Ambient earth motion in the period range from 0.1 to 2560 seconds, Bull. Seis. Soc. Amer., 62, pp 1753-1760.
- Gorshkov, G. S., (1959), Gigantic eruption of the Volcano Bezymianny, Bull. Volcanol., 20, pp. 77-109.
- Harkrider, D. G., (1964), Theoretical and acoustic gravity waves from explosive sources in the atmosphere, Jour. Geophys. Res., 69, pp 5295-5321.
- Havskov, J., De La Cruz-Reyna, S., Singh, S., Medina, F., and Gutierrez, C., (1982), Seismic Activity Related to the March-April, 1982 Eruptions of El Chichon Volcano, Chiapas, Mexico, EOS, 63, p. 1126 (abstract).
- Herdervari, P., (1963), On the energy and magnitude of volcanic eruptions, Bull. Volcanol., 25, pp. 373-385.
- Kienle, J., and Shaw, G. E., (1979), Plume dynamics, thermal energy and long-distance transport of Volcanian eruption clouds from Augustine Volcano, Alaska, Jour. Volcanol. & Geothermal Res., 6, pp. 139-164.
- Le Guern, F., Bernard, A., and Chevrier, R. M., (1980), Soufriere of Guadeloupe 1976-1977 eruption-mass energy transfer and volcanic health hazards, Bull. Volcanol., 43-3, pp. 577-593.
- Landisman, M., Dziewonski, A. and Sato, Y., (1969), Recent improvements in the analysis of surface wave observations, Geophys. Jour., 186, pp 39-
- Larson, R. J., Craine, L. B., Thomas, J. E. and Wilson, C. R., (1971), Correlation of winds and geographic features with the production of certain infrasonic signals in the atmosphere, Geophys. Jour., 26, pp 201-214.

- Lucas, D. H., (1967), Application and evaluation of results of Tilbury plume rise and dispersion experiment, Atmos. Environ., 1, pp 421-424.
- McDonald, J. A., Douze, E. J. and Herrin, E., (1971), The structure of atmospheric turbulence and its application to the design of pipe arrays, Geophys. Jour., 25, pp 99-109.
- Melson, W. G., and Saenz, R., (1973), Volume, energy and cyclicity of eruptions of Arenal Volcano, Costa Rica, Bull. Volcanol., 37-3, pp. 416-437.
- Newhall, C. B., and Self, S., (1982), The Volcanic Explosivity Index (VEI): an estimation of explosive magnitude for historic volcanism, Jour. Geophys. Res., 87 (Green), pp. 1231-1238.
- Pierce, A. D., (1966), Guided infrasonic modes in a temperature and wind stratified atmosphere, Jour. Acoust. Soc. Amer., 41, pp 597-611.
- Savino, J., McKamy, K. and Hade, G., (1972), Structure in earth noise beyond 20 seconds - a window for earthquakes, Bull. Seis. Soc. Amer., 62, p 141-
- Savino, J. and Rynn, J. M. W., (1972), Quasi-static loading of the earthy propagating air waves, Jour. Geophys. Res., 77, pp 5033-5041.
- Settle, M., (1976), Rise of Volcanic Eruption Clouds: Relationship between Cloud Height and Eruption Intensity, Air Force Geophysical Laboratory Technical Report AFGL-TR-76-0127, 37 p.
- Settle, M., (1978), Volcanic eruption clouds and the thermal power output of explosive eruptions, Jour. Volcanol. and Geothermal Res., 3, pp. 309-324.
- Silva, L., Cocheme, J., Canul, R., Duffield, W., Tilling, R., (1982), The March-April, 1982, Eruptions of Chichonal Volcano, Chiapas, Mexico: Preliminary Observations, EOS, 63, p 1126 (abstract).
- Sorrells, G. G., (1971), A preliminary investigation into the relationship between long-period noise and local fluctuations in the atmospheric pressure field, Geophys. Jour., 26, pp 71-82.
- Sorrells, G. G., and Goforth, T., (1973), Low frequency earth motion generated by slow moving partially organized pressure fields, Bull. Seis. Soc. Amer., 63, pp 1583-1601.
- Sorrells, G. G. and Douze, E. J., (1974), Studies of long-period seismic noise generated by atmospheric pressure charges, Teledyne Geotech technical report 74-5, 29 p.
- Sorrells, G. G., (1981), The investigation of the combined use of microbarometric and seismic data to detect and identify infrasonic signals, Teledyne Geotech technical report no. 81-11, 18 p.
- Sparks, R. S. J., and Wilson, L., (1982), Explosive volcanic eruptions-V. Observations of plume dynamics during the 1979 Soufriere eruption, St. Vincent, Geophys. J. R. Astr. Soc., 69, pp. 551-570.

Wexler, H. and Hass, W. A., (1962), Global atmospheric pressure effects of the October 30, 1961, explosion, Jour. Geophys. Res., 67, pp 3875-3887.

Wilson, L., (1976), Explosive volcanic eruptions-III. Plinian eruption columns, Geophys. J. R. Astr. Soc., 45, pp. 543-556.

Wilson, L., Sparks, R. S. J., Huang, T. C., and Watkins, N. D., (1978), The control of volcanic column heights by eruption energetics and dynamics, Jour. Geophys. Res., 83, pp. 1829-1836.

Wilson, L., (1980), Relationships between pressure, volatile content and ejecta velocity in three types of volcanic explosion, Jour. Volcanol. Geo. Res., 8, 297-313.

Wilson, L., Sparks, R. S. J., and Walker, G. P. L., (1980), Explosive volcanic eruptions-IV. The control of magma properties and conduit geometry on eruption column behavior, Geophys. J. R. Astr. Soc., 67, pp. 117-148.

APPENDIX A

Derivation of Infrasonic SNR

APPENDIX A

DERIVATION OF INFRASONIC SNR

Let $m(t)$ and $u_z(t)$ denote the outputs of a microbarograph and vertical seismograph, respectively. With the wind blowing, and an infrasonic signal present:

$$m(t) = r_m^*(p_s + p_n) \quad (1)$$

where r_m is the response of the microbarograph, p_s is the infrasonic pressure signal, p_n is the turbulent noise created by the wind, and $(*)$ denotes convolution. Similarly,

$$u_z(t) = r_s^*(g_{zs}^*p_s + g_{zn}^*p_n + n_z) \quad (2)$$

where r_s is the response of the seismograph, g_{zs} and g_{zn} are the Greens functions for the vertical component of displacement caused by an infrasonic signal and wind noise, respectively, and n_z is the vertical component of seismic noise. For a vertical seismograph located at a depth of 150 meters, it can be shown that the expected value of the noise due to atmospheric noise will be much less than that of other noise sources.

$$\langle (g_{zn} * p_n)^2 \rangle \ll \langle (n_z)^2 \rangle \quad (3)$$

So, equation 2 may be approximated as

$$u_z(t) \approx r_z^* (g_{zs} * p_s + n_z) \quad (4)$$

The corresponding power spectra of $m(t)$ and u_z (5) may be written

$$M(\omega) = |R_m|^2 (P_s + P_n) \quad (5)$$

$$U_z(\omega) \approx |R_z|^2 (|G_{zs}|^2 P_s + N_z) \quad (6)$$

where M , U_z , P_s , P_n are the power spectral density functions associated with m , u_z , p_s , p_n , and n_z . R_m , R_z and G_{zs} are the complex terms for functions associated with r_m , r_z and g_{zs} . Rewriting equation 5 as:

$$\frac{M(\omega)}{|R_m|^2} = P_s + P_n \quad (7)$$

and equation 6 as

$$\begin{aligned} \frac{U_z(\omega)}{|R_z|^2 |G_{zs}|^2} &\approx P_s + \frac{N_z}{|G_{zs}|^2} \\ &\approx P_s + P_n' \end{aligned} \quad (8)$$

It can be seen that the term

$$p'n = \frac{N_z}{|G_{zs}|^2} \quad (9)$$

and can be thought of as an equivalent pressure noise power spectral density estimate for the earth motion field.

Let $(SNR)_z$ and $(SNR)_m$ be the signal-to-noise ratios for the earth motion and pressure fields, the

$$(SNR)_z = \frac{P_s}{P'_n} \quad (10)$$

and

$$(SNR)_m = \frac{P_s}{P_n} \quad (11)$$

The ratio, I_{zm} of the signal-to-noise ratios can be written

$$I_{zm} = \frac{(SNR)_z}{(SNR)_m} \quad (12)$$

and will reduce to

$$I_{zm} = \frac{P_n}{P'_n} \quad (13)$$

Therefore, if we restrict our attention to an interval in time where $P_s \approx 0$ and we know the module of the transfer functions R_m , R_z , G_{sz} , we can estimate I_{zm} for the outputs of a microbarograph and vertical seismograph.

APPENDIX B

Earth Transfer Function

APPENDIX B

EARTH TRANSFER FUNCTION

From equations (5) and (6) of appendix A the seismograph vertical power spectra, $U_z(\omega)$ and microbarograph power spectra, $M(\omega)$ are

$$U_z(\omega) \approx |R_z|^2 (|G_{zs}|^2 P_s + N_z) \quad (1)$$

$$M(\omega) = |R_m|^2 (P_s + P_n) \quad (2)$$

The cross-power spectral density between the vertical seismograph power spectra and microbarograph power spectra is defined as $G_{zm}(\omega)$, which equals

$$G_{zm}(\omega) = [R_z(G_{zs} P_s + N_z)]^* \cdot R_m(P_s + P_n) \quad (3)$$

where (*) as a superscript is a complex conjugate.

Expanding equation (3),

$$\begin{aligned} G_{zm}(\omega) = & R_z^* G_{zs}^* P_s^* R_m P_s + R_z^* N_z^* R_m P_s \\ & + R_z^* G_{zs}^* P_s^* R_m P_n \\ & + R_z^* N_z^* R_m P_n \end{aligned} \quad (4)$$

If we restrict our interval in time to one where other inputs to the seismograph are uncorrelated with changes in the local atmospheric load, then the cross power spectra reduces to

$$G_{zm}(\omega) = R_z^* G_{zs}^* R_m P_s^2 \quad (5)$$

Taking the magnitude of the cross spectrum, equation (5) is transformed to

$$|G_{zm}(\omega)| = |R_z| |G_{zs}(\omega)| |R_m| |P_s|^2 \quad (6)$$

Dividing the cross spectra magnitude by the power spectrum of the microbarograph

$$\frac{|G_{zm}(\omega)|}{M(\omega)} = \frac{|R_z| |G_{zs}(\omega)| |R_m| P_s^2}{|R_m|^2 (P_s^2 + P_n^2)} \quad (7)$$

equation (7) can be reduced to

$$\frac{|G_{zm}(\omega)|}{M(\omega)} = \frac{|G_{zs}(\omega)| |R_z|}{|R_m| (1 + \frac{P_n^2}{P_s^2})} \quad (8)$$

We assume that during an infrasonic signal, the power spectra of a signal will be \gg than the noise spectra and equation (8) reduces to

$$\frac{|G_{zm}(\omega)|}{M(\omega)} = \frac{R_z}{R_m} |G_{zs}(\omega)| \quad (9)$$

We can then solve for the earth transfer function $G_{zs}(\omega)$ by equation (10)

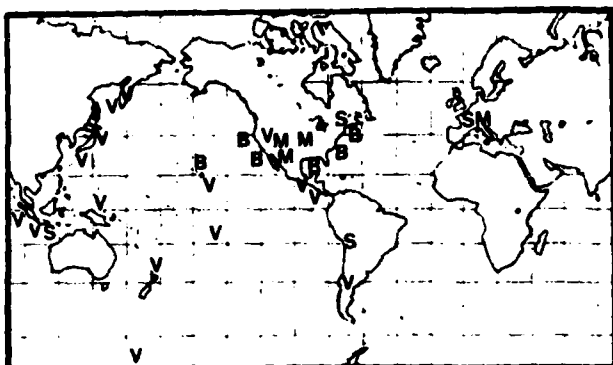
$$\frac{|R_m|}{|R_z|} \frac{|G_{zm}(\omega)|}{M(\omega)} = G_{zs}(\omega) \quad (10)$$

APPENDIX C

El Chichon Reports from SEAN Bulletin,
Volume 7, Numbers 3, 4, 5, and 6



Smithsonian Institution



B-Biologic M-Meteoritic S-Seismic V-Volcanic

SEAN Scientific Event Alert Network BULLETIN

VOLUME 7, NO. 3, MARCH 31, 1982

VOLCANIC EVENTS

El Chichón (México): Large explosions; voluminous ashfalls; many deaths; first eruption in historic time	2-6
Colima (Mexico): Lava extrusion continues	7
Mt. St. Helens (Washington): First large explosion since October 1980; 2 new lobes added to lava dome	7-10
Galunggung (Indonesia): Heavy ashfall; mudflows; 8 killed	10
Marapi (Indonesia): 30-minute ash ejection	11
Plosky (Kamchatka): Glacier surge	11
Alaid (Kurile Is.): Plume on satellite imagery	11
Kilauea (Hawaii): Small intrusions into E and SW rifts	11-12
Erebus (Antarctica): Lava lake level lower	12
Manam (Bismarck Sea): Strong explosions; pyroclastic flow; seismicity	12-13
Langila (New Britain): Incandescent tephra; increased seismicity	13
Akan (Japan): Sudden increase in local seismicity	13
Sakurajima (Japan): Frequent explosions; B-type earthquakes	13-14
Usu (Japan): Cryptodome growth slows; local seismicity continues	14-15
Ruapehu (New Zealand): Explosions from crater lake; seismicity summarized	15-17
Pacaya (Guatemala): Flank lava effusion continues	17
Descabezado Grande (Chile): New fumarole in main crater	17
Mehetia (French Polynesia): Seismic activity stops	17-18
Nicaragua: Activity at 7 volcanoes summarized	18
Atmospheric Effects: Volcanic cloud remains in stratosphere; source still uncertain	19

EARTHQUAKES

S Netherlands (M 4.5) 2 March	20
Lesser Sunda Islands, Indonesia (M 6.5) 11 March	20
Hokkaido, Japan (M 6.9) 21 March	20
N Peru (M 4.7) 23 March	20
W Peru (M 6.1) 28 March	20
New Brunswick, Canada (M 4.8)	20

METEORITIC EVENTS

Fireballs: Czechoslovakia, S Germany, Netherlands (update), USA (4)	20-23
---	-------

NATURAL HISTORY SPECIMENS

Marine Turtles	24-25
----------------	-------

MARINE MAMMAL STRANDINGS & SIGHTINGS

Cetacea	25-30
Seals	30-33
Sea Otters	33
Manatees	34-37

ADDITIONAL INFORMATION & CORRECTIONS

37

Lindsay McClelland, Janet Crampton (geologists) • Shirley Maina, Paula Rothman (biologists)
SCIENTIFIC EVENT ALERT NETWORK • National Museum of Natural History
Mail Stop 129 • Washington, DC 20560 • Telephone (202) 357-1511 • Telex 89599SCINET WSH

(Data are preliminary and subject to change: contact the original source or SEAN before using)



VOLCANIC EVENTS

El Chichón Volcano, S Mexico (17.33°N, 93.20°W). All times are local (= GMT - 6 hours).

After several weeks of local seismicity, explosions from El Chichón in late March and early April ejected a series of tephra columns, 2 of which penetrated well into the stratosphere. No previous historic eruptions are known from this volcano, situated to the SE of México's main volcanic belt. Officials reported that as many as 100 persons may have been killed by the eruption and associated seismic activity. Tephra falls were very heavy near the volcano, forcing tens of thousands of residents to flee their homes, and causing major damage to crops and livestock.

28-29 March

The eruption began 28 March at 2332 and NOAA geostationary weather satellite imagery showed that the eruption column was about 100 km in diameter 40 minutes later. Analysis of an infrared image returned at 0300 yielded a cloud top temperature of -75°C, corresponding to an altitude of 16.8 km, about 1 km above the tropopause. Surface and vault microbarographs and a KS36000 (SRO-type) seismograph operated by Teledyne Geotech near Dallas, Texas (1797 km from El Chichón) received 22 minutes of infrasonic signals generated by explosive activity. Nine distinct signals were recorded, including a strong gravity wave, indicating that the eruption column struck the tropopause. Instruments at McMurdo, Antarctica, 11865 km from El Chichón, recorded about 2 hours of infrasonic signals. Nine intensity peaks were detected, of which 5 were clearly from the eruption.

Vigorous feeding of the plume continued for several hours but had clearly ended by 0600. A dense tephra cloud drifted ENE from the volcano and a much more diffuse plume moved in roughly the opposite direction (see Figure 1). By 0530 the next morning, satellite images showed the main plume extending from the Yucatán Peninsula, S of Cuba, to Haiti, and remnants of the more diffuse plume over the E Pacific Ocean at about 15°N, and 118-119°W. The U. S. National Weather Service analyzed wind directions and speeds at different altitudes near the volcano, and concluded that the ENE drift of the dense cloud indicated that it was in the upper troposphere, whereas the diffuse plume blown to the WSW was in the middle troposphere at roughly 6-7.5 km altitude. Initially, none of the tephra appeared to be drifting in a direction consistent with the lower stratospheric circulation, but significant aerosol development in the stratosphere is indicated by the LIDAR measurements described in the next-to-last paragraph of this report.

Excerpts from the geophysical section of the SEAN Bulletin are printed in EOS, a publication received weekly by members of the American Geophysical Union (2000 Florida Avenue NW, Washington, DC 20009). The complete Bulletin is available in the microfiche edition of EOS, as a microfiche supplement, or a paper reprint. For the microfiche, order document number E82-003 at \$1.00 from AGU. For reprints, order SEAN Bulletin (give date and volume number) through AGU Separates: \$3.50 for the first copy of any issue to those who do not have a deposit account; \$2.00 to those who do; additional copies are \$1.00. Orders must be prepaid. SEAN Bulletin subscriptions are available from AGU at \$18/year to US addresses and \$28/year to other countries.

The SEAN Bulletin is also available from the National Technical Information Service (U. S. Department of Commerce, Springfield, Virginia 22161), publication number PB82-9157. Annual subscription fee for North American continent countries is \$40.00; elsewhere, \$80.00. One calendar year of the Bulletin on microfiche is available at \$6.25 and \$12.50 respectively for the above geographic areas. PB82-915703

El Chichón Volcano (continued)

Heavy ashfall was reported from towns near the volcano. At Pichucalco, about 20 km NE of the summit, 15 cm of ash was reported, and 5 cm of ash fell at Villahermosa (population 100,000), 70 km NE of the volcano. Residents of Nicapa, a village on the NE flank, took refuge in a church that was toppled by a magnitude 3.5 earthquake, killing 10 people and injuring about 200. Initial estimates of the number of additional deaths varied, ranging as high as 100, and many more were probably killed on the SW flank during this or subsequent eruptions (see 5 paragraphs below). Most of the casualties on the N flank were reportedly caused by fires started by incandescent airfall tephra. Tens of thousands of people fled the area. The heavy ashfall forced the closure of roads and the airports at Villahermosa and Tuxtla Gutierrez (about 70 km S of the volcano). Cocoa, coffee, and banana crops were destroyed, and the cattlemen's association requested that animals from a wide area be transported for butchering because ashfall had made grazing impossible.

30 March-3 April

A second but much smaller explosion was observed on the satellite imagery at about 0900 on 30 March. A thin plume drifted E about 120 km before dissipating. A somewhat larger explosion that was first visible at 1500 produced a cloud that rose into the mid-troposphere and moved about 350 km to the N. Activity was declining by 1900. Haze was widespread over central Mexico, reducing visibility to about 8 km in Mexico City (about 650 km WNW of the volcano) and to only about 3 km in Tampico (about 750 km NW of the volcano). A small explosion shortly before 1330 on 31 March produced a plume that reached the upper troposphere and blew to the E but dissipated quickly.

A small explosion during the early afternoon of 2 April ejected a mushroom-shaped cloud that rose to about 3.5 km altitude in 30 minutes. Satellite images showed renewed explosive activity early 3 April. An eruption column was emerging from the volcano by 0300 and blew to both the NE and SW. A series of gravity waves and acoustic signals from this activity were again recorded by Teledyne Geotech instruments near Dallas, Texas. The calculated start time for this activity was 0250 and signals continued for 14 minutes. As with the initial explosion 28 March, the powerful gravity waves generated by this event indicated that the eruption column struck the tropopause forcefully. Smaller explosions, calculated to have begun at 0312, generated acoustic waves and a single gravity wave that were received near Dallas for 10 minutes. During the next 5 hours, ash drifted over N Guatemala and Belize. At Nicapa, on the NE flank, 7.5 cm of new ash was reported and a haze of SO₂ was visible during the day. Explosive activity resumed about 2000. Acoustic data recorded by Teledyne Geotech indicated that explosions probably occurred every 2-3 minutes, generating a few initial gravity waves and a complex series of acoustic waves that continued for 48 minutes. The total acoustic energy of this activity was significantly greater than that produced by the early morning explosions, and the eruption plume was denser and probably rose somewhat higher. It was initially elongate NE-SW and drifted over S Mexico, N Guatemala and Belize. By noon the next day, a faint plume extended to about 25°N, 79°W, almost to Cuba, and lower altitude material, probably at only about 1.5 km, was drifting directly northward along the 95°W meridian.

4 April

A stronger explosion, possibly larger than the initial event 28 March, first appeared on the NOAA geostationary weather satellite image returned at 0530 4 April and was reported by ground observers to have started at 0522. An infrared image 3.5

El Chichón Volcano (continued)

hours later showed a temperature of -76°C at the top of the eruption cloud, corresponding to an altitude of 16.8 km, identical to the altitude measured from the 28 March plume. Wind speeds near the volcano apparently remained relatively low and most of the cloud remained over S Mexico and N Guatemala more than 24 hours later. In Pichucalco (about 20 km NE of the summit) incandescent tephra could be seen rising from the volcano and the ash cloud darkened the sky during the morning as though it were night. Felt earthquakes were also reported early 4 April. At Ixtacomitán, 18 km ENE of the summit, there was a heavy fall of tephra no larger than 4 cm in diameter and the army was sent to evacuate 3,000 residents. No casualties were reported. All villages within 15 km of the summit had previously been evacuated and tens of thousands of people had fled their homes. Government officials reported ashfall over an area of 24,000 km² and crop damage of \$55,000,000.

A pumice flow deposit from the 4 April eruption extended about 5 km NE from the summit, terminating about 2 km from Nicapa. At its distal end, the deposit was about 100 m wide and 3 m thick and contained pumice blocks 1 m in diameter. Temperatures measured by a thermocouple at 40 cm depth on 8 April averaged 360°C , and were as high as 402°C . The pumice flow deposit appeared to have been emplaced as 2 separate events in rapid succession. Shortly afterward, an ash flow flattened trees in the valley surrounding the pumice flow deposit and left a relatively thin layer of ash that had a temperature of 94°C at 10 cm depth 3 days later.

Airfall tephra thickness in Nicapa, 7 km NE of the summit, totaled 25-40 cm after the 4 April eruption. Bombs as large as 50-60 cm in diameter had made numerous holes in the roofs of houses and many other roofs had collapsed. In hand specimen, the tephra appeared to be a crystal-rich andesite or dacite containing hornblende and considerable feldspar. In Ostuacán, 12.5 km NW of the summit, tephra was 15-20 cm thick after the 4 April eruption, including pumice as large as 15 cm in diameter. Many roofs had been destroyed. Extreme heat made it impossible to approach the village of Francisco León, 5 km SW of the summit. Midway between Ostuacán and Francisco León, a river was boiling and flattened trees could be seen upslope. Geologists thought it was likely that pyroclastic flows had moved through the area. Of the roughly 1000 residents of Francisco León, about half had reportedly left before the eruption because of the many felt earthquakes in February and March, but the remainder were missing in early April. A helicopter flight over the village during the first week in April revealed no signs of life. Because of the danger of mudflows when the rainy season begins around the end of April, authorities established a prohibited zone extending outward 10 km from the summit.

By 5 April, the low-altitude plume from the second 3 April explosion had reached the S Texas coast and Brownsville reported visibility of only 6.5 km in haze. A few flights into small S Texas airports were cancelled, but winds initially forced most of this material into the Gulf of Mexico. Low-altitude (1.5-2 km) ejecta from the 4 April explosion also moved northward, and a slight change in wind direction blew the ash cloud further N and inland over Texas by late 7 April. A light ashfall occurred in Houston during the night of 7-8 April and samples were collected for analysis by NASA geologists.

5-11 April

A plume generated by a smaller explosion was observed on satellite imagery at 1130 on 5 April. Ground observers reported that the comparatively minor activity lasted about 3 hours and that no incandescent tephra was ejected. A similar but possibly slightly larger explosion could be seen on the satellite image returned at

El Chichón Volcano (continued)

0930 on 6 April. Geologists reported that earthquakes as strong as magnitude 1.5 were recorded about every 3 minutes 6 April. Geologists working a few km NE of the summit reported that about 2 mm of wet ash fell at about 1000 on 8 April and 1130 on the 9th. Satellite images returned at 0728 on 9 April and 0238 on 10 April both showed small diffuse plumes, drifting NNE and SSE respectively.

Data from laser radar (LIDAR) measurements at Mauna Loa Observatory, Hawaii (about 19.5°N, 155.6°W) during the nights of 9-10 and 10-11 April indicated that El Chichón had injected large quantities of volcanic material into the stratosphere (see Table 1). Several layers were detected, with strongest backscattering at an altitude of 25.7 km. Analysis of wind conditions at 25 km altitude in Hawaii and México indicated a likely drift of about 5-7 m/second (roughly 430-600 km/day) towards the W, which would carry volcanic debris from El Chichón to Hawaii in 1 1/2 to 2 weeks. Inspection of a satellite image returned late 11 April showed a moderately dense cloud extending from México to just W of Hawaii, spreading from roughly 300 km wide near the Mexican coast to nearly 850 km near its distal end.

No previous eruptions of El Chichón are known in historic time. Before the 1982 eruption, the volcano was heavily forested, with a shallow crater, 1900 m by 900 m, elongate NNW-SSE. Solfataras and hot springs were present in the crater and on the flanks. Müllerried (1933) describes voluminous airfall deposits from previous eruptions that he believed to be post-Pleistocene.

References: Müllerried, F.K.G., 1932, Der Chichón, ein bisher unbekannter taetiger Vulkan im noerdlichen Chiapas, México; Zeitschrift für Vulkanologie v. 14, no. 3, p. 191-209.

Müllerried, F.K.G., 1933, El Chichón, Unico Volcán en Actividad en el Sureste de México; Universidad de México, v. 5, no. 27, p. 156-170.

TABLE 1

DATE AND TIME	LAYER ALTITUDE IN KM (peak in parentheses)	BACKSCATTER
10 April, 0600 GMT	19-20.6 (20.6)	3.5
	21.5-23 (22)	48
	23-24.5 (24)	25
	24.5-26.2 (25.7)	222
11 April, 1400 GMT	(13.7)	60
	(22)	32
	(23.8)	112

Table 1: Altitudes of layers of material, probably from El Chichón, observed by ruby-wavelength LIDAR from Mauna Loa Observatory, Hawaii. The backscattering ratios given are peaks for each layer. A layer of volcanic debris of unknown origin, observed during each LIDAR measurement since late January, is not included in this table but is described in the "Atmospheric Effects" report at the end of the Volcanic Events section.

Information contacts: Cinna Lomnitz, Instituto de Geofísica, Universidad Nacional Autónoma de México, México 20, D.F. México; Servando de la Cruz and Francisco Medina, Instituto de Geofísica, Universidad Nacional Autónoma de México,

El Chichón Volcano (continued)

Ciudad Universitaria, 04510 México D.F. México; Maurice Krafft, Centre de Volcanologie Vulcain, B.P. 5, 68700 Cernay, France; Dennis Haller and Charles Kadin, Synoptic Analysis Branch, NOAA/National Earth Satellite Service, S/OP33, Camp Springs, Maryland 20233 USA; Michael Matson, Land Sciences Branch, NOAA/National Earth Satellite Service, Camp Springs, Maryland 20233 USA; H. M. Johnson, Applications Laboratory, NOAA/National Earth Satellite Service, Camp Springs, Maryland 20233 USA; Arthur Krueger, Climate Analysis Center, NOAA/National Weather Service, Camp Springs, Maryland 20233 USA; Fred Mauk, Teledyne Geotech, 3401 Shiloh Road, Garland, Texas 75041 USA; Charles Wilson, Geophysical Institute, University of Alaska, Fairbanks, Alaska 99701 USA; Kenneth Coulson, Mauna Loa Observatory, P.O. Box 275, Hilo, Hawaii 96720 USA; Charles A. Wood, NASA, Johnson Space Center, Code SN-6, Houston, Texas 77058 USA; Notimex Radio, México City, México; The New York Times; United Press International.

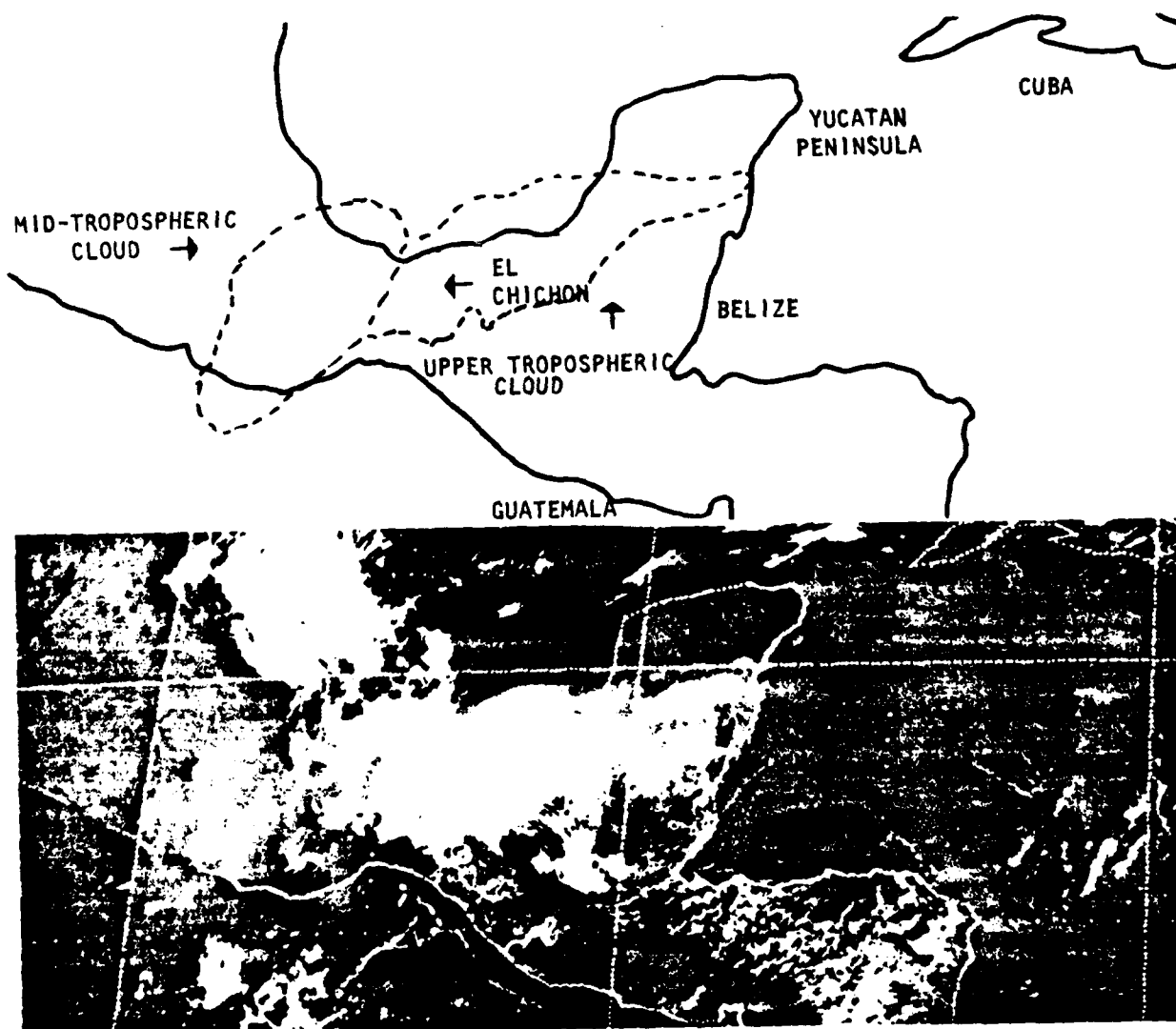


Figure 1: NOAA geostationary weather satellite image returned 29 March at 1000, about 10.5 hours after El Chichón's initial explosion. A dense upper tropospheric eruption cloud drifts ENE, and a more diffuse cloud drifts WSW, probably in the mid-troposphere.

See also the addendum at the bottom of page 23.

Missouri (continued)

Information Contact: Gary Baird, Route 5, Box 568A, Carthage, Missouri 64836 USA.

W Texas, USA, 27 February, 044520 GMT (214520 Mountain Standard Time)

Observers: More than 40 local citizens; 1 airline pilot, who gave the time

Location: El Paso (31.23°N, 106.45°W)

Path: E to W, nearly straight down (deviating from the vertical only about 5°)

Duration: 4-5 seconds

Magnitude: 1/8-1/2 the size of the full moon; like a magnesium flare

Color: Brilliant bluish white, to bright then dark red, to orange

The pilot observed the fireball, traveling steeply downward, appear to expand and brighten before it reddened and disappeared below his altitude of 11.2 km. An observer on the E side of El Paso reported that fireball lit the E slope of Mt. Franklin, in the center of the city. Observers on the W side of the city heard 2 or 3 booming noises that rattled windows about 3 minutes after the fireball had disappeared. A rancher between El Paso and Deming, New Mexico reported that the fireball extinguished at about 30° above the horizon. In Deming an observer described it as small and brilliant, then red, then orange, and appearing to travel very slowly.

Information Contact: Donald Rathbun, M.D., El Paso Medical Center, Suite 1-C, 1501 Arizona, El Paso, Texas 79902 USA.

Addendum

El Chichon Volcano

Hector Galindo provided the following additional information about the eruption at press time.

The initial vulcanian eruption started suddenly at 2332 on 28 March, ejected about 1/3 km of ash, and deposited pumice more than 10 km from the summit. After several days of relatively minor activity, a similar eruption began 3 April at about 1933 and lasted for about an hour. At 0536 on 4 April, a third strong eruption ejected large quantities of ash and pumice as well as several pyroclastic flows that were no longer than 6 km. In mid-April, continuous emission of ash limited visibility to several hundred meters and flights around the volcano were precluded by the large number of particles suspended in the atmosphere.

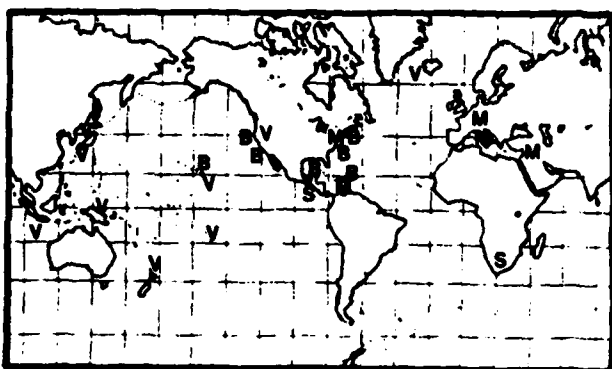
Most of the ashfall from El Chichon has been N of the volcano, with reported thicknesses of 0.1 cm at 200 km distance, 0.3 cm at 100 km, and 25 cm at 10 km. The total volume of ejecta was estimated at 0.5 km.

Installation of a seismic net around the volcano began 31 March. As of mid-April, 10 portable seismographs from the National University of Mexico were in place, as were several radon detectors.

Information Contact: Hector Galindo, Director, Instituto de Geofisica, Universidad Nacional Autonoma de Mexico, Ciudad Universitaria, 04510 Mexico D.F. Mexico.



Smithsonian Institution



B-Biologic M-Meteoritic S-Seismic V-Volcanic

SEAN

Scientific Event Alert Network

BULLETIN

VOLUME 7, NO. 4, APRIL 30, 1982

VOLCANIC EVENTS

El Chichón (México): 4 April stratospheric cloud circles the globe; minor explosive and seismic activity continues	2-5
Mt. St. Helens (Washington): Lava extrusion adds new lobe to composite dome	5-6
Teahitia (French Polynesia): Seismicity suggests first historic eruption ...	6-7
Kilauea (Hawaii): Small fissure eruption in summit caldera	7-8
Galunggung (Indonesia): Explosions and pyroclastic flows	8-9
Asama (Japan): Explosions; small pyroclastic flow; ash falls on Tokyo	9-11
Sakurajima (Japan): Explosion rate declines; gas damages crops	10
Ruapehu (New Zealand): Explosive activity declines	11
Manam (Bismarck Sea): Smaller explosions; earthquakes and harmonic tremor ..	12
Langila (New Britain): Incandescent tephra; ashfalls; seismicity	12
Krafla (Iceland): Slow inflation continues; previous activity summarized ...	12-13

EARTHQUAKES

Off S Guatemalan Coast (M 6.8) 6 April	14
S Africa (M 5.0) 13 April	14

METEORITIC EVENTS

Fireballs: Czechoslovakia (2), Italy, Lebanon, Netherlands (update), USA (2), U.S. Virgin Islands	14-17
---	-------

NATURAL HISTORY SPECIMENS

Marine Turtles	18-19
----------------------	-------

MARINE MAMMAL STRANDINGS & SIGHTINGS

Cetacea	19-24
Seals	24-27
Sea Otters	28
Manatees	28-30

ADDITIONAL INFORMATION & CORRECTIONS	31-33
--	-------

Lindsay McClelland, Janet Crampton (geologists) • Shirley Maina, Paula Rothman (biologists)
 SCIENTIFIC EVENT ALERT NETWORK • National Museum of Natural History
 Mail Stop 129 • Washington, DC 20560 • Telephone (202) 357-1511 • Telex 89599SCINET WSH
 (Data are preliminary and subject to change; contact the original source or SEAN before using)



VOLCANIC EVENTS

El Chichón Volcano, S México (17.33°N, 93.20°W). All times are local (= GMT - 6 hours).

A major eruption of El Chichón, its first in historic time, began with a large explosion late 28 March (see last month's Bulletin). This explosion produced heavy tephra falls N of the volcano, but the initial press reports of the thickness of ash deposits, included in last month's Bulletin, were exaggerated (see below). As many as 100 persons may have been killed on the N side of the volcano and flank villages were badly damaged. Tens of thousands of people fled the area, and damage to crops and livestock grazing areas was substantial. Intermittent weaker tephra emission continued for the next several days. A series of 3 explosions of increasing size occurred 3-4 April, the last of which, at 0522 on 4 April, was the largest of the eruption and produced a major stratospheric cloud, described below. Pyroclastic flows moved several km down flank valleys (see description in last month's Bulletin). Conflicting reports persist about the fate of the approximately 1000 residents of a SW flank village that was apparently in the path of one or more pyroclastic flows ejected 28 March or 3-4 April.

Infrasonic Data

In addition to the infrasonic data collected from near Dallas, Texas (see last month's Bulletin), the array at McMurdo, Antarctica (11865 km from El Chichón) recorded about 2 hours of acoustic waves from the 28 March explosion. At College, Alaska (6634 km from the volcano), about an hour of acoustic signals were received from both the 28 March and 4 April explosions. Antipodal acoustic-gravity wave signals from the first 3 April and 4 April explosions were detected at Tennant Creek, Australia (19.52°S, 134.25°E).

Volume and Composition of Tephra

Tephra samples were collected from about 100 sites around El Chichón in mid-April. Near the volcano, 3 separate layers were evident, ejected by explosions 28 March, 3 April (at 2000) and 4 April. Farther away, only 28 March and 4 April tephra had been deposited. The axis of maximum deposition extended approximately N from the summit for the 28 March tephra and roughly E from the summit for the 4 April material. Both of these layers were normally-graded but the 3 April layer, where present, consisted only of fine ash. James Luhr calculated that about 0.20 km³ of tephra (converted to a density of 2.6 grams/cm³) had fallen within the 0.1 cm isopach (see Figure 1). X-ray fluorescence analyses of pumice samples showed no significant variation in chemical composition, either within individual units or between units. The pumice, a porphyritic trachyandesite, has a whole-rock silica content of about 57.5%; silica content of the glass is about 61%.

Minor Activity April-May

No large explosions have taken place since 4 April, but occasional minor ash emission continued. The active crater, about 600 m in diameter in early May, was located within the pre-existing shallow summit crater that had dimensions of about 1900 m by 900 m. A 12-km prohibited zone around the summit remained in effect in early May. A 4-station seismic monitoring network operated by the Universidad Nacional Autónoma de México (UNAM) recorded 6-8 small earthquakes per day in early May, including some B-type events. The ejection of a minor ash column on 11 May was

El Chichón Volcano (continued)

accompanied by a few small discrete earthquakes centered at about 2 km depth, and additional seismicity that may have been harmonic tremor.

Stratospheric Cloud

Careful inspection of visible satellite imagery from the NOAA 6 and 7 polar orbiters, the GOES East and West (U.S.), GMS (Japan), and Meteosat (Europe) geostationary weather satellites has permitted the tracking of the densest portion of the 4 April stratospheric cloud as it circled the globe from E to W. The cloud reached Hawaii by 9 April, Japan by 18 April, the Red Sea by 21 April, and had crossed the Atlantic Ocean by 26 April, dipping S to about 5°N at its W edge. Diffusion into higher latitudes appeared to be very limited. During its first circuit of the globe, the cloud could be seen in part (but usually not all) of the range 5°-30°N, sometimes occupying a band roughly 15°-20° wide. Tracking of the cloud after late April has been difficult, but careful work may allow the position of the cloud front to be established after that date. Ozone data from the NIMBUS 7 polar orbiting satellite, available for the 2 weeks following the cloud's ejection, allowed its path to be clearly traced, and scientists at the Goddard Space Flight Center hope to continue observations of its position as more satellite data arrives. A balloon flight from Laramie, Wyoming (41.33°N, 105.63°W) in mid-April detected a sharp peak at 17 km (just below the tropopause at 18 km).

Laser radar (LIDAR) stations in the United States, Japan, and Europe recorded enhanced backscattering in the stratosphere at times that correlated well with satellite observations of the cloud's movement (see Table 1). Very strong signals were detected by stations at lower latitudes, while the cloud appeared to be present only intermittently and near the base of the stratosphere over mid-latitude stations. A possible northward diffusion of the cloud, probably on its second circuit of the globe, is shown by the sharply higher backscattering ratios detected at Fukuoka, Japan (33.65°N, 130.35°E) in May. At lower latitudes, the strongest layers were centered above 25 km. The highest layer detected was at 29.7 km altitude.

Persons in the SW United States observed phenomena that indicated the presence of stratospheric layers. A Bishop's Ring was first seen from Houston, Texas on 11 April and has been intermittently visible since. The 22° angular distance from the sun indicated a particle size of 0.7-0.9 microns. Unusual sunrises and sunsets have been reported from E Texas since 24 April. From Tucson, Arizona, Aden and Marjorie Meinel observed a primary scattering layer at 13.2 km and a weaker layer at 20 km around sunset on 30 April. By early May, the aerosol cloud had become extremely dense, with most of the material between 14 and 18 km and a trace to 20.5 km. The main body of the layer appeared to pass NW of Tucson during the evening of 7 May. Long windrows of aerosol were visible, similar to the phenomenon seen after the 1976 Augustine eruption. The conspicuous clouds had nearly disappeared by 9 May, but a strong aureole remained around the sun all day 10 May.

The high altitude of the cloud made direct sampling difficult and none has been possible in the densest portion above 25 km. Flights from the NASA Ames Research Center near San Francisco to about 23°N on 19 April and 5 May sampled the base of the cloud at about 19 km altitude. Optical depths of the cloud as measured with a sun photometer reached 0.3-0.4, increasing southward. Particles ranging in size from 0.1 to 3 microns were collected. Sulfuric acid droplets were common, but there were very few silicate particles. However, NaCl crystals were a significant component and salt

El Chichón Volcano (continued)

has apparently never before been found in significant quantities in a volcanic cloud. Measurement of the degree of depolarization of layers detected at 15-16.5 km and 24-25.5 km 22 April by LIDAR equipment at Nagoya University (about 35°N, 137°E) suggested that particles in the lower layer were strongly non-spherical, while those in the upper layer were mostly spherical droplets.

Information Contacts: Francisco Medina, Instituto de Geofísica, UNAM, Ciudad Universitaria, 04510 México D.F., México; James Luhr, Dept. of Geology and Geophysics, University of California, Berkeley, California 94720 USA; Michael Matson, Dennis Haller, and Charles Kadin, NOAA/National Earth Satellite Service, Camp Springs, Maryland 20233 USA; Bernard Mendonça, NOAA/ERL, Air Resources Laboratory, Code RF 3292, 325 Broadway Avenue, Boulder, Colorado 80303 USA; Kenneth Coulson, Mauna Loa Observatory, P.O.Box 275, Hilo, Hawaii 96720 USA; Motokazu Hirono, Department of Physics, Kyushu University, Fukuoka 812, Japan; William Fuller, NASA, Langley Research Center, Hampton, Virginia 23665 USA; Yasunobu Iwasaka, Water Research Institute, Nagoya University, Chikusa-ku, Nagoya 264, Japan; Raymond Chuan, Brunswick Corporation, Costa Mesa, California 92626 USA; Charles Wilson, Geophysical Institute, University of Alaska, Fairbanks, Alaska 99701 USA; D.R. Christie, Research School of Earth Sciences, Australian National University, Canberra, ACT, Australia; James Rosen, Dept. of Physics and Astronomy, University of Wyoming, Laramie, Wyoming 82071 USA; Aden and Marjorie Meinel, Optical Sciences Center, University of Arizona, Tucson, Arizona 85721 USA; Michael Helfert, NOAA, 1050 Bay Area Blvd., Houston, Texas 77058 USA; W.F.J. Evans, ARPX-AES, 4905 Dufferin St., Downsview, Ontario M3H 5T4 Canada.

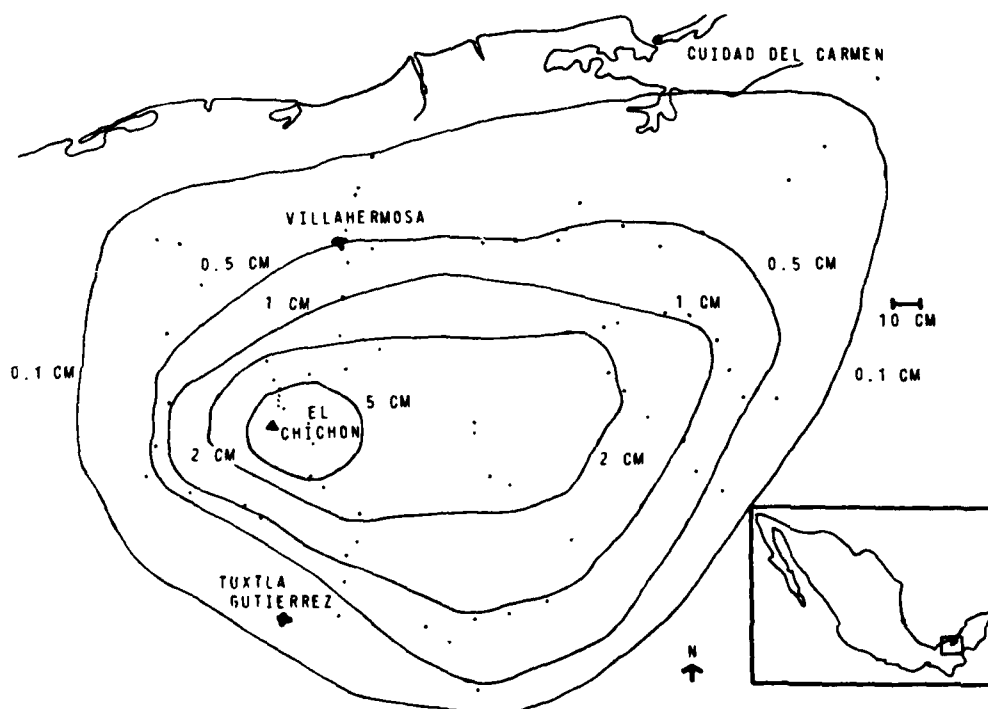


Figure 1: Isopach map showing thickness of compacted ash at a density of 1.2 g/cm^3 , for tephra ejected from El Chichón Volcano, 28 March-4 April.

El Chichón Volcano (continued)

LOCATION AND DATE	TABLE 1 LAYER ALTITUDE IN KM (peak in parentheses)	BACKSCATTER
Mauna Loa, Hawaii (19.5°N, 155.6°W) 23 April	(16.4) (17.8) (21) (24.4)	2 2 6.5 2.4
5 May	13.7-14.3 (14.0) (18.4) 21-22.6 (22) 25-28 (26.8)	4 5 50 118
11 May	(21.4) (22.3) (25) (27.1) (29.7)	17.5 22.4 21.6 83.9 2.7
Fukuoka, Japan (33.65°N, 130.35°E) 18 April	(16) (24) (25) (26)	6.2 3.2 2.3 5
4 May	(17) (21.5) (23) (24.5) (26)	12.5 18 24 470 57
Langley, Virginia (37.1°N, 76.3°W) 29 April	(26.5) (16.3) (19.2)	52 1.9 1.8
4 May	no layers detected	
10 May	16.7-17.7 (17.4)	2.3

Table 1: LIDAR data from various stations showing altitudes of aerosol layers. The altitude of the peak backscattering ratio in each layer is in parentheses. All backscattering ratios are for the ruby wavelength of 0.69 microns. For earlier data from Mauna Loa, see last month's Bulletin.

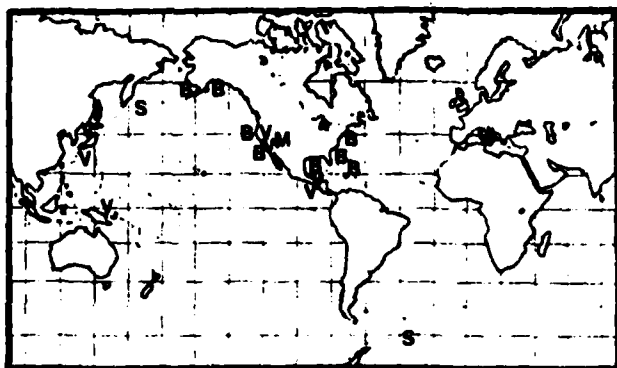
Mt. St. Helens Volcano, Cascade Range, S Washington, USA (46.20°N, 122.18°W). All times are local (= GMT - 8 hours through 24 April, GMT - 7 hours thereafter).

The eruptive episode that began 19 March included the first large explosions since October 1980 and the extrusion of 2 new lobes onto the composite dome (see last month's Bulletin). The tephra volume of the 19 March eruption column was of the same order of magnitude as (but probably slightly less than) that of the October 1980 cloud (not 20-60 times less, as reported in last month's Bulletin). Extrusion of lava onto the N side of the composite dome stopped by 10 April and seismicity had dropped to low levels by the 12th, but another dome-building phase began on 14 May.

During the 19 March activity, the crater floor thrust fault scarps near the dome were either buried or scoured away. Measurement of the rates of movement of these small faults had previously been an important deformation monitoring technique. By early May a number of small new thrusts had formed on the crater floor W and SW of the dome, but had not yet yielded useful deformation data. Data from a



Smithsonian Institution



B-Biologic M-Meteoritic S-Seismic V-Volcanic

SEAN

Scientific Event Alert Network

BULLETIN

VOLUME 7, NO. 5, MAY 31, 1982

VOLCANIC EVENTS

El Chichón (México): Fatal flood after natural pyroclastic dam fails; stratospheric cloud effects; eruption summary	2-6
Mt. St. Helens (Washington): Frequent gas and ash emission; more on May lobe	6-7
Long Valley (California): Seismic swarms; new fumaroles; uplift	7-9
Costa Rica: Activity at 4 volcanoes summarized	9-10
Langila (New Britain): Explosive activity, lava flow and ashfalls	10
Manam (Bismarck Sea): Ash emission; slight inflation	10
Sakurajima (Japan): Incandescent tephra, ashfall	11
Asama (Japan): No further eruptions; vapor emission remains high	11
Etna (Italy): Small central crater explosions follow earthquakes and higher ground temperatures	11-13
Krafla (Iceland): Ground level high but no eruption	13

EARTHQUAKES

SW Atlantic Ocean (M 6.7) 5 May	13
Komandorsky Islands (M 6.5) 31 May	13

METEORITIC EVENTS

Fireball: Colorado, USA	13
-------------------------------	----

NATURAL HISTORY SPECIMENS

Marine Turtles	14-15
----------------------	-------

MARINE MAMMAL STRANDINGS & SIGHTINGS

Cetacea	16-19
Seals	20-28
Sea Otters	28-29
Manatees	29-30

ADDITIONAL INFORMATION & CORRECTIONS	30
--	----

Lindsay McClelland, Janet Crampton (geologists) • Shirley Maina, Paula Rothman (biologists)
SCIENTIFIC EVENT ALERT NETWORK • National Museum of Natural History
 Mail Stop 129 • Washington, DC 20560 • Telephone (202) 357-1511 • Telex 89599SCINET WSH

(Data are preliminary and subject to change: contact the original source or SEAN before using)



VOLCANIC EVENTS

El Chichón Volcano, S México (17.33°N, 93.20°W). All times are local (= GMT - 6 hours).

The following summary was prepared by L. Silva, J.J. Cochemé, R. Canul, W. Duffield, and R. Tilling.

"Violent eruptions of the strato-volcano El Chichón destroyed its summit dome and formed a 1-km-wide crater. Field studies and eyewitness accounts indicate that the initial activity (28-29 March) was phreatomagmatic, and produced a plinian column over 15 km high and tephra deposits extending more than 200 km downwind. More vigorous activity 3-4 April produced several pyroclastic flows, some more than 15 m thick, followed by 2 airfall deposits. Distal sections consist of 3 airfall layers whereas proximal sections include pyroclastic flows. The total volume of eruptive products is probably less than 0.5 km³, much of which is juvenile pumice, which is highly porphyritic with plagioclase, amphibole, and clinopyroxene as major phenocrysts. Petrographic and chemical data suggest an alkali-rich "andesitic" composition. The high alkali content of the pumice, occurrence of anhydrite in tephra, and presence of halite in the stratospheric cloud reflect contamination by evaporites. Villages within a 7-km radius were entirely destroyed or heavily damaged. Pyroclastic flows dammed a river and created a 5-km-long lake of hot water; the failure of the natural dam on 26 May caused a destructive flood. Study of pre-1982 deposits indicates that El Chichón has developed by several cycles of pyroclastic eruptions, with or without a subsequent growth of domes, with the last pre-1982 pyroclastic eruption about 130 years ago. The current activity may continue and could include dome emplacement."

Premonitory Seismicity

During field work at El Chichón between December 1980 and February 1981, more than 1 year before the eruption, René Canul heard loud noises and felt small earthquakes near the central dome, and could also feel some events while on the flanks of the volcano. People living near the volcano reported felt earthquakes several months before the eruption.

March-April Explosions

The March and April explosions destroyed most of the former central lava dome and formed a new crater, about 1 km in diameter and slightly elongate NW-SE. In

Excerpts from the geophysical section of the SEAN Bulletin are printed in EOS, a publication received weekly by members of the American Geophysical Union (2000 Florida Avenue NW, Washington, DC 20009). The complete Bulletin is available in the microfiche edition of EOS, as a microfiche supplement, or a paper reprint. For the microfiche, order document number E82-005 at \$1.00 from AGU. For reprints, order SEAN Bulletin (give date and volume number) through AGU Separates: \$3.50 for the first copy of any issue to those who do not have a deposit account; \$2.00 to those who do; additional copies are \$1.00. Orders must be prepaid. SEAN Bulletin subscriptions are available from AGU at \$18/year to US addresses and \$28/year to other countries.

The SEAN Bulletin is also available from the National Technical Information Service (U. S. Department of Commerce, Springfield, Virginia 22161), publication number PB82-9157. Annual subscription fee for North American continent countries is \$40.00; elsewhere, \$80.00. One calendar year of the Bulletin on microfiche is available at \$6.25 and \$12.50 respectively for the above geographic areas. PB82-915705

El Chichón Volcano (continued)

early June, there were several explosion pits on the floor of the new crater, all of which were filled with boiling water or mud and were emitting vapor. Although heavy rains had compacted the ash, 3-4 m remained at the rim of the new crater.

The army reported that 187 deaths were caused directly by the eruption. Among the deaths were one geologist and 32 soldiers sent to the village of Francisco León, about 6 km SW of the summit, after the 28-29 March explosion. The pyroclastic flow that traveled through Francisco León left only a thin deposit, but of the structures in the village, only one wall of the church, parallel to the direction of the pyroclastic flow's movement, remained standing.

All of the volcano's major drainages contained pyroclastic flow deposits, which were more than 15 m thick in some of the deeper valleys. These deposits were still hot in late May and were occasionally the source of small secondary explosions. In the 2 months since the March-April explosions, as much as 20 m of erosion has taken place in some areas and fan deposits have formed at the base of the volcano.

May Activity and Flood

Lakes formed behind natural dams of new pyroclastic flow deposits at several sites around the volcano. The largest lake, in the valley of the Río Magdalena at the SW foot of the volcano, grew about 1 m deeper each day until 26 April, then more slowly, eventually reaching 5 km in length and several million m³ in volume. Late 26 May, the pyroclastic dam holding back this water failed. Seismographs recorded the draining of the lake over a period of about 1 hour, sending a flood of hot water downstream. At Ostuacán, more than 10 km from the dam, the water temperature was measured at 82°C. Most residents of low-lying areas had been evacuated, but at a hydroelectric project 35 km downstream 1 worker was killed and 3 were badly burned by 52°C water. The flood also destroyed a bridge several km from the pyroclastic dam. Geologists inspecting the former lake bed in early June saw a series of strand lines several m high, indicating that the lake had been draining slowly before the dam failed.

No large explosions have occurred at El Chichón since 4 April. Minor ash emission continued through early May but none has been reported since the 11th (see last month's Bulletin). A 4-station Instituto de Geofísica seismic net N of the volcano recorded 4-7 very small events per day in late May.

By late May, significant revegetation had begun in some areas devastated by the eruption. Near Nicapa (about 7 km NE of the summit), coconut trees totally denuded by the 4 April explosion showed new leafy growth. Some residents had returned to Nicapa and cattle were grazing in the area. Closer to the summit, fields that had been completely buried contained tufts of grass about 1/3 m high.

Stratospheric Cloud

The major stratospheric cloud ejected by El Chichón has remained concentrated over lower northern latitudes, but laser radar (LIDAR) data and observations of brilliant sunsets appeared to indicate the beginning of significant northward dispersal in early June. However, with NASA's SAGE satellite no longer functional, determination of the extent of the cloud at any given time is very difficult. Through mid-May, wind data from Hilo, Hawaii showed a strong (up to 240 km/hour), steady W to E flow between 10 and 20-22 km altitude, and a steady, 50-60 km/hour E to W flow above 25-26 km. Between these levels, winds were light and variable. No

El Chichón Volcano (continued)

significant N-S component had developed above 10 km since the El Chichón eruption. LIDAR at Mauna Loa, Hawaii (19.5°N, 155.6°W) and Fukuoka, Japan (33.65°N, 130.35°E) continued to detect dense layers of stratospheric material through early June, at altitudes of as much as 32 km over Hawaii (see table 1). University of Wyoming balloon flights from Laredo, Texas 17-19 May passed through 2 primary layers, at 15-20 km and 24-27 km altitude. In the upper layer there were more than 500 particles of less than 0.01 micron size per cm³ and about 20 particles larger than 1 micron per cm³. April 1982 NOAA 7 satellite data between 120°E and 122.5°W showed an apparent increase in albedo (visible band) and an apparent decrease in outgoing longwave radiation (thermal infrared band) between 15°N and 35°N, peaking at 23°-26°N, when compared with the zonal average from the previous 4 years. Further analysis of samples collected 5 and 7 May during NASA Ames Research Center flights south from San Francisco shows particles ranging from less than 0.1 microns to several microns at the base of the cloud (about 19 km altitude). Silicates and halite crystals of several microns in size were found. Halite concentration was only a few percent of the amount of H₂SO₄ sampled, but H₂SO₄ was not as dominant as in many previous volcanic clouds. Geologists suggested that the halite sampled by NASA and anhydrite found in tephra near the volcano are probably the result of contamination by evaporites, which were found in bedrock penetrated by 2 Petroleos Mexicanos drillholes near El Chichón.

From Tucson, Arizona on 14 May, Aden and Marjorie Meinel observed a roughly 40 by 400 km band of smoky clouds pass overhead during the afternoon, but at sunset these clouds appeared to be at an altitude of only 8 km. A dense veil covered the sky 15-16 May. A brilliant fiery red glow appeared 35 minutes after sunset on 16 May. The top of this glow was at 24 km, the highest altitude observed from Tucson thus far. A feature similar to Bishop's Ring was observed 17 May and windrows of aerosol moved over Tucson later that afternoon. A dense veil was present 18 May but was nearly gone on the 19th and skies were almost normal early 20 May. From Kitt Peak National Observatory near Tucson, extinction of 2 times normal at 3900 Angstroms was measured in mid-May. Scattering was about equal at all wavelengths except near-infrared, where the cloud was more transparent. Unusual twilight colors were observed through mid-May from Flagstaff, Arizona, and extinction coefficients measured there were about 3 times the normal value. A strong haze has been present over Houston, Texas since early May. Spectacular sunsets were observed there in late May and early June and the haze blotted out stars during the night of 2-3 June. Similar conditions plus a Bishop's Ring were seen from Austin, Texas during the night of 5-6 June. From Norwich, England, H.H. Lamb observed a rose-colored pillar of light at sunset 27 April and 9 May. At sunset 10-12 May, this phenomenon was accompanied by brilliant orange to fiery red diffused light that extended to 3-4 sun diameters. Strongly diffused light extended 2-3 diameters from a fiery red sun on 23 May. From the dimensions of the extended twilight illumination, Lamb estimated that the layer was at very roughly 20 km altitude. Lamb saw no abnormal effects on other evenings, although poor weather frequently made observations impossible.

By early June, laser radar (LIDAR) observations and reports of unusual sunsets indicated that the cloud was beginning to move northward. LIDAR operated by NASA at Langley, Virginia (37.1°N, 76.3°W), began to detect layers at higher altitudes in early June. After a brilliant sunset on 14 June, a dense layer at 20.2-23.1 km was accompanied by material at 26.5 km (see table 1). However, as of early June, LIDAR stations in Italy and West Germany had not detected layers at these altitudes. Enhanced sunsets with definite striations began 4 June in Boulder, Colorado and continued for the next several days. Residents of Jacksonville, Florida also began to see brilliant sunsets 4 June.

El Chichón Volcano (continued)

LOCATION AND DATE	TABLE 1	BACKSCATTER
	LAYER ALTITUDE IN KM (peak in parentheses)	
Mauna Loa, Hawaii (19.5°N, 155.6°W) 14 May	20.5-22 (21.4)	13
	23.2-25.3 (24.1)	40
	25.3-30 (26.8)	153
	30	10
3 June	31	3
	(15.2)	6
	22-31 (23.2)	36
	(24.1)	38
Fukuoka, Japan (33.65°N, 130.35°E) 3 June	(28.1)	89
	(18)	5
	(23)	40
	(25.5)	150
Langley, Virginia (37.1°N, 76.3°W) 2 June 9 June	(28)	4
	(28.5)	10
	(29)	4
	15.5-20.4 (17)	1.5
14 June	(23.4) 400 m thick	2.7
	16-19.5 (18.6)	1.8
	(19.5) 500 m thick	1.6
	(20.5) 600 m thick	4
	(21.5) 5-600 m thick	2
	16.5-19.5	1.5
	(19.9) 400 m thick	3.5
	20.2-23.1 (20.4)	2
	(22.2)	3
	(22.6)	8
	(26.5) 800 m thick	1.6

Table 1: LIDAR data from various locations, showing altitudes of aerosol layers. The altitude of the peak backscattering ratio in each layer is in parentheses. Note that some layers have multiple peaks. Backscattering ratios from Hawaii and Virginia are for the ruby wavelength of 0.69 microns. Those from Japan are for the YAG wavelength of 1.06 microns.

Correction: The caption for Table 1 of last month's Bulletin incorrectly stated that all LIDAR measurements were at the ruby wavelength. In fact, LIDAR data from Fukuoka, Japan were at the YAG wavelength of 1.06 microns, as they are in the table above. The relationship between ruby and YAG values is on the average, approximately $r - 1 = k(y - 1)$, where r = ruby wavelength backscatter and y = YAG wavelength backscatter. The value of k is not constant and its variation provides information on the size distribution of the aerosols. Motokazu Hirono provided a preliminary estimate for the present value of k at 0.4.

Information Contacts: Luis Silva M. and Jean-Jacques Cochemé, Instituto de Geología, UNAM, Ciudad Universitaria, México, D.F., México; René Canul D., Comisión Federal de Electricidad, Gerencia de Geotermia, Morelia, México; Servando de la Cruz R., Francisco Medina, and Manuel Mena, Instituto de Geofísica, UNAM, Ciudad Universitaria, 04510 México, D.F., México; Jens Hauskov and Shri Krishna Singh, Instituto de Ingeniería, UNAM, Ciudad Universitaria, México D.F., México; Robert Tilling, USGS, Stop 951, National Center, Reston, Virginia 22092 USA; Wendell Duffield, USGS, Mail Stop 90 C, 345 Middlefield Road, Menlo Park, California 94025

El Chichón Volcano (continued)

USA; William Fuller, NASA, Langley Research Center, Hampton, Virginia 23665 USA; Thomas DeFoor, Mauna Loa Observatory, P.O. Box 275, Hilo, Hawaii 96720 USA; Motokazu Hirono, Department of Physics, Kyushu University, Fukuoka 812, Japan; Bernard Mendonça, NOAA/ERL, Air Resources Laboratory, Code RF 3292, 325 Broadway Avenue, Boulder, Colorado 80303 USA; James Rosen, Department of Physics and Astronomy, University of Wyoming, Laramie, Wyoming 82071 USA; Raymond Chuan, Brunswick Corporation, Costa Mesa, California 92626 USA; Michael Matson, Land Sciences Branch, NOAA/National Earth Satellite Service, Camp Springs, Maryland 20233 USA; Aden and Marjorie Meinel, Optical Sciences Center, University of Arizona, Tucson, Arizona 85721 USA; Brian Skiff, San Francisco Mountain Cosmographic Group, 421 W Aspen, Flagstaff, Arizona 86001 USA; William Livingston, Kitt Peak National Observatory, Box 26732, Tucson, Arizona 85726 USA; Michael Helfert, NOAA, 1050 Bay Area Blvd., Houston, Texas 77058 USA; James Nania, Deaconess Hospital, West 800 5th Avenue, Spokane, Washington 99210 USA; Numero Uno newspaper, Tuxtla Gutierrez, México.

Mt. St. Helens Volcano, Cascade Range, S Washington, USA (46.20°N, 122.18°W). All times are local (= GMT -7 hours).

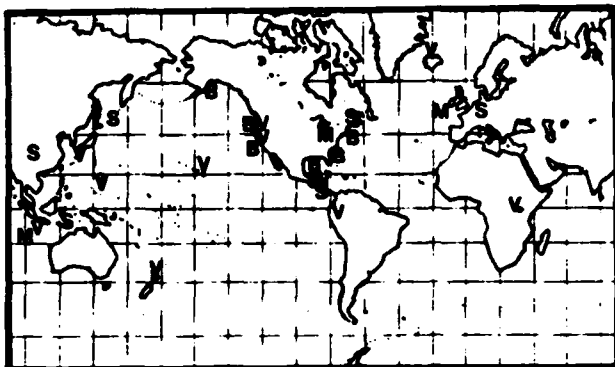
Increasing deformation and seismicity in early May was followed by the extrusion of new lava onto the composite dome. Lava began to flow down the NE side of the dome 14 May, but the bulk of the new lava formed a lobe on the dome's NW flank 15-19 May. Since then, ejections of steam and ash, similar to those of July and August 1981, have occurred about once a day. Two of these, on 7 and 8 June, caused light ashfalls on Portland (about 80 km to the SW). Gas emission rates remained high through early June.

Deformation of the composite dome and the surrounding crater floor was slow until early May, then accelerated (see last month's Bulletin). The crater floor deformation was blocky and incoherent, as it has been during previous pre-extrusion periods. While a continuously recording tiltmeter at a new site on the W crater floor recorded increasingly rapid subsidence (as did a dry tilt station at the same location), reoccupation of dry tilt stations less than 100 m away showed accelerating uplift. The development of a small thrust fault was observed between the dome and the continuously recording tiltmeter, leading Dan Dzurisin to suspect that thrusting was responsible for the different tilt directions at nearby sites.

Local seismicity had begun to increase on 8 May (see last month's Bulletin). In the 24 hours starting at 0700 on 13 May, 63 earthquakes were recorded (about twice the previous day's number) and some were felt by geologists working in the crater that day. Three radiating fractures, trending NE, N, and NW were seen in the April lobe, on the N side of the dome. SO₂ emission remained at background levels of about 100 tons/day. The rapid subsidence measured by the continuously recording tiltmeter stopped about midnight. Harmonic tremor started shortly thereafter, at 0055 on 14 May, and continued until about 0600. Bursts of seismic energy could be seen within the tremor. During an overflight at 0415, spectacular, nearly continuous cascades of incandescent material could be seen on the NE flank of the dome, but an hour later the rockfalls had ceased almost entirely. After dawn, a jumbled, blocky area could be seen on the dome's summit and upper NE flank and there was a rockfall apron on the NE side of the dome. The jumbled area was larger by afternoon, but it was not certain whether it was new lava or scoriaceous older material being uplifted by endogenous dome growth. Episodic gas emission was observed on 14 May and by afternoon the rate of SO₂ release had increased fourfold from the previous day, to about 400 tons/day. The number of earthquakes decreased to 20 in the 24 hours starting at 0700 on 14 May.



Smithsonian Institution



B-Biologic M-Meteoritic S-Seismic V-Volcanic

SEAN Scientific Event Alert Network BULLETIN

VOLUME 7, NO. 6. JUNE 30, 1982

VOLCANIC EVENTS

El Chichón (México): No new explosions; dense stratospheric cloud over N hemisphere; unusual sunrises and sunsets	2-5
Nyiragongo (Zaire): Fountaining feeds new lava lake	5
Galunggung (Indonesia): Explosions continue; most of 1918 dome destroyed; 40,000 evacuated	5-7
Long Valley (California): Minor earthquake swarm; additional uplift of resurgent dome since 1980	7
Kilauea (Hawaii): Intrusion into the SW rift	7-8
Mt. St. Helens (Washington): Gas and tephra plumes; deformation	8-9
Guagua Pichincha (Ecuador): Phreatic explosions; new fumaroles; seismicity ..	9-11
Esmeralda Bank (Mariana Is.): Submarine sulfur emission	11-12
White Island (New Zealand): Localized inflation; no eruptive activity	12-13
Ruapehu (New Zealand): Lake temperature and level drop; no new explosions ..	13-14
Sakurajima (Japan): Frequent explosions; tephra cause minor damage	14
Krafla (Iceland): Inflation stops without eruption	15

EARTHQUAKES

S Mexico (M 6.7 and M 7.0) 7 June	15
Sichuan, China (M 5.6) 15 June	15
New Brunswick, Canada (M 4.7) 16 June	15
El Salvador (M 7.0) 19 June	15
Banda Sea (M 6.5) 22 June	15
W Germany (M 4.8) 28 June	15
Kuril Islands (M 6.9) 30 June	15

METEORITIC EVENTS

Fireballs: N Atlantic Ocean, E Indian Ocean, SW Michigan	16
--	----

NATURAL HISTORY SPECIMENS

Marine Turtles	17-19
----------------------	-------

MARINE MAMMAL STRANDINGS & SIGHTINGS

Cetacea	19-21
Seals	21-26
Sea Otters	27
Manatees	28

Lindsay McClelland, Janet Crampton (geologists) • Shirley Maina, Paula Rothman (biologists)
SCIENTIFIC EVENT ALERT NETWORK • National Museum of Natural History
 Mail Stop 129 • Washington, DC 20560 • Telephone (202) 357-1511 • Telex 89599SCINET WSH

(Data are preliminary and subject to change. Contact the original source or SEAN before using.)



VOLCANIC EVENTS

El Chichón Volcano, S México (17.33°N, 93.20°W).

No large explosions have occurred at El Chichón since 4 April and weak ash emission was last observed 11 May. Minor microseismic activity was continuing in early July. The large stratospheric cloud ejected by the 4 April explosion remained dense over lower northern latitudes, but lidar (laser radar) measurements indicated that gradual northward dispersal was continuing.

Pyroclastic Flows and Casualties

Major erosion of pyroclastic flow deposits around El Chichón (see figure 1) has taken place since the eruption. Some small accumulations of water remain associated with these deposits, but there have been no recent observations of large lakes such as the one that produced a fatal flood 26 May (see last month's Bulletin). The largest eruption killed many people in and near the village of Francisco León (about 5 km SW of the summit), but initial reports that all of its residents died were incorrect, according to an American missionary who had lived in the village for many years. Many villagers who had fled the heavy tephra falls from the initial explosions 28-29 March, however, returned a few days later. About 140 residents of the village itself and a similar number from the countryside nearby were killed by the pyroclastic flow that destroyed the village 4 April (see last month's Bulletin).

Stratospheric Cloud

A late April - early May NASA flight collected stratospheric material at altitudes above 18 km over the W United States (including Alaska). The flight crew reported unambiguous evidence of the cloud as far N as the US-Canada border and estimated that it reached more than 21 km altitude. A preliminary examination of the material collected showed that it was a well-sorted assemblage of 5-10 micron plagioclase crystals and silicic glass, with a small amount of a mafic mineral (probably an amphibole) and traces of a Ca and S-rich mineral (probably a Ca sulfate). Scientists proposing investigation of this sample should write to: Curator, Code SN2, NASA Johnson Space Center, Houston, Texas 77058 USA.

Lidar data collected in June at Mauna Loa, Hawaii (19.5°N, 155.6°W) showed backscattering that typically increased from near the base of the stratosphere to a peak at 26-27 km altitude, with significantly enhanced values to 33-34 km (see table 1). In June, the Mauna Loa data were less variable from night to night and layering

Excerpts from the geophysical section of the SEAN Bulletin are printed in EOS, a publication received weekly by members of the American Geophysical Union (2000 Florida Avenue NW, Washington, DC 20009). The complete Bulletin is available in the microfiche edition of EOS, as a microfiche supplement, or a paper reprint. For the microfiche, order document number E82-006 at \$1.00 from AGU. For reprints, order SEAN Bulletin (give date and volume number) through AGU Separates: \$3.50 for the first copy of any issue to those who do not have a deposit account; \$2.00 to those who do; additional copies are \$1.00. Orders must be prepaid. AGU will offer SEAN Bulletin subscriptions at \$18/year to US addresses and \$28/year to all other countries.

The SEAN Bulletin is also available from the National Technical Information Service (U. S. Department of Commerce, Springfield, Virginia 22161), publication number PB82-9157. Annual subscription fee for North American continent countries is \$40.00; elsewhere, \$80.00. One calendar year of the Bulletin on microfiche is available at \$6.25 and \$12.50 respectively for the above geographic areas. PB82-915706

El Chichón Volcano (continued)

within the cloud was less distinct than in May. The cloud above Hawaii has apparently affected incoming solar radiation, measured for about 50 years by the Hawaiian Sugar Planters Association. Although mean daily solar radiation would normally have been about 110% of the long-term average (because precipitation in May at the primary station was only 27% of normal), the measured value for the month was only 92% of average.

Lidar at Fukuoka, Japan (33.65°N, 130.35°E), showed persistent but decreased backscattering from the 21-29 km layer in late June, but backscattering increased again in early July. The less dense layer at 18.5 km remained stable through this period. In early July, backscattering detected by lidar at Langley, Virginia (37.1°N, 76.3°W) increased sharply for the (highest) layer centered at about 25 km altitude, approaching those values measured at lower latitudes for the first time.

To assess latitudinal variation in the stratospheric cloud, a lidar-equipped NASA aircraft flew from Wallops Island, Virginia to Puerto Rico during the night of 8-9 July, to about 12°N (near the coast of Venezuela) 10 July, and from Puerto Rico to the vicinity of Albany, New York (about 42°N) 11 July. From 25-30°N to the southern limit of the flight, preliminary data show greatly enhanced backscattering from a dense layer between 21 and 33 km altitude. Some material was present below 21 km, but it was much less dense. Strong local variation in the cloud was observed. Although the cloud diminished in density N of 25-30°N, significantly enhanced stratospheric backscattering was detected to the northern limit of the flight.

Brilliant Sunrises and Sunsets-Saudi Arabia

Weather satellite images first showed the front of the 4 April stratospheric cloud (visible over water during the day) over the Red Sea 21 April. Edward Brooks, who has made frequent sunrise and sunset observations from Jeddah, Saudi Arabia (21.5°N, 39.16°E) saw WNW-ESE-trending bands of haze in the WNW sky after sunset 20 April and similar bands before dawn the next morning. The twilight of 24 April was a brilliant pink from bands and patches of WSW-ENE-trending aerosol. During the next several weeks, volcanic cloud effects could be seen in the sky around sunrise and sunset most days, often as bands of material oriented within 45° of E-W. Brooks observed a layer 10° above the horizon at twilight 18 May and calculated its altitude at roughly 20-25 km. Multiple layers began to be visible in June. At sunrise on 5 June, criss-cross bands of aerosol trended SW-NE and SSE-NNW. Brilliant sunrises and sunsets were common in mid-June. Beginning on 19 June, many sunrises illuminated 2 distinct layers, at about 30 minute intervals. This effect weakened later in the month and by 30 June the higher layer (illuminated earlier in the morning) had disappeared. Brooks and others also noted that on 6 July roughly the upper half of the eclipsed moon was considerably darker than the lower half, which Brooks interprets as indicating the presence of volcanic aerosols in the atmosphere of the earth's northern (but not southern) hemisphere.

El Chichón Volcano (continued)

LOCATION AND DATE	TABLE 1 LAYER ALTITUDE IN KM (peak in parentheses)	BACKSCATTER
Mauna Loa, Hawaii (19.5°N, 155.6°W) 22 June	16-34 (27)	90
Fukuoka, Japan (33.65°N, 130.35°E) 26 June	(18) (21) (24)	5.2 37 5
3 July	(21.3) (23.2) (25) (26.2)	7.5 37 92 122
Langley, Virginia (37.1°N, 76.3°W) 2 July	15.0-19.5 (17) (19.2) 19.8-21.8 (20.2) 22.5-23.5 (23) 24.0-26.8 (25.2)	2 2.4 1.8 5 35

Table 1: Lidar data from various locations, showing altitudes of aerosol layers. Note that some layers have multiple peaks. Backscattering ratios from Hawaii and Virginia are for the ruby wavelength of 0.69 microns. Those from Japan are for the YAG wavelength of 1.06 microns. For an equation expressing the average relationship between ruby and YAG values, see p. 5 of last month's Bulletin.

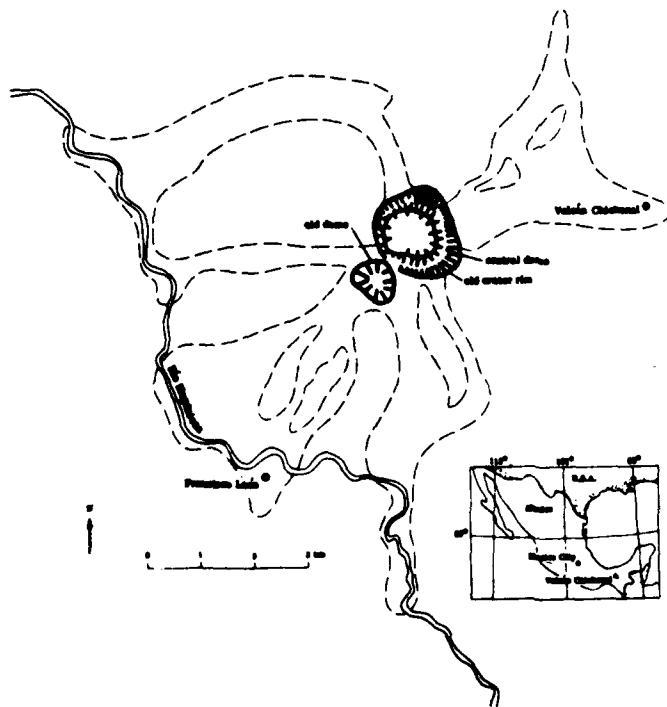


Figure 1: Sketch map (adapted from a map by Luís Silva) showing approximate locations of pyroclastic flow deposits around El Chichón, and changes to the summit area. The new crater (rim outlined by the inner hachured ring) is nested within the old crater. Most of the former central dome was destroyed by the eruption.

El Chichón Volcano (continued)

Information Contacts: Servando de la Cruz R., Instituto de Geofísica, UNAM, Ciudad Universitaria, 04510 México D.F., México; Luis Silva M., Instituto de Geología, UNAM, Ciudad Universitaria, México D.F., México; Robert Tilling, Stop 951, USGS, National Center, Reston, Virginia 22092 USA; William Fuller and M. P. McCormick, NASA, Langley Research Center, Langley, Virginia 23665 USA; Thomas DeFoor, Mauna Loa Observatory, P.O. Box 275, Hilo, Hawaii 96720 USA; Motokazu Hirono, Department of Physics, Kyushu University, Fukuoka 812, Japan; Edward M. Brooks, c/o JECOR/ARMETED, P.O. Box 8638, Jeddah, Saudi Arabia; Karl How, Hawaiian Sugar Planters Association, P.O. Box 1057, Aiea, Hawaii 96701 USA; William Wonderly, 4209 San Pedro NE, Apt. 322, Albuquerque, New Mexico 87109 USA; James Gooding, Code SN2, NASA, Johnson Space Center, Houston, Texas 77058 USA; Michael Matson, Land Sciences Branch, NOAA/National Earth Satellite Service, Camp Springs, Maryland 20233 USA.

Nyiragongo Volcano, E Zaire (1.48°S, 29.23°E).

Lava fountaining began 26 June in Nyiragongo's central crater and by 7 July a lava lake covered the crater floor. No activity had been reported at Nyiragongo since 10 January 1977, when the lava lake that had persisted since 1928 drained through flank fissures in a 1-hour eruption that killed between 60 and 100 people (see Tazieff, H., Bulletin Volcanologique, v. 40, p. 189-200 and SEAN Bulletin v. 2, nos. 1-4).

On 26 and 27 June, two 5-10 m-high lava fountains were observed at the bottom of the crater. By 30 June, only 1 fountain was active, feeding a very small lava pool. However, when a geologist climbed to the crater rim 7 July, a lava lake about 1/2 km across covered the crater floor. In the center of the lake was a domical lava fountain 30-50 m high and 150 m in diameter. The fountain and the rim of the lake were bright orange, a color similar to that seen during periods of vigorous fountaining before 1977. About 1/3 of the lake was covered by a fissured black skin. Based on comparisons with known pre-eruption features in the crater, the lake level was estimated to have risen 100-150 m between 26 June and 7 July. Most of the lava seemed to be entering the lake from below, but a very small amount of lava was emerging from a 10-m-diameter vent in the N wall of the crater, about 50 m above the lake surface. This vent had apparently been more active a few days earlier. From Goma, 17 km to the SSW, a glow was still visible over the crater 13 July. Earthquakes during the night of 4-5 July shook furniture and formed fissures in old houses in Goma.

Information Contact: Maurice Krafft, Centre de Volcanologie Vulcain, B.P. 5, 68700 Cernay, France.

Galunggung Volcano, W Java, Indonesia (7.25°S, 108.05°E). All times are local (= GMT + 7 hours).

Intermittent explosions from Galunggung began 5 April (see SEAN Bulletin v. 7, no. 4), destroying about 90% of Gunung Jati, the lava dome extruded into Galunggung's large breached summit crater during the last eruption in 1918. Lahars and nuées ardentes flowed southeastward through the breach onto the upper portion of the major prehistoric landslide deposit. The highest reported ash column reached 16.5 km, pitting the windshield of a passing airplane. Ash fell as far away as the Yogyakarta-Solo area, about 300 km to the E.

The 10 eruptive episodes that had occurred as of late June were separated by quiescent periods that ranged from 3 days (early in the eruption) to 3 weeks (before

APPENDIX D

Selected References on Volcanic
Explosivity, Energy, and Magnitude

REFERENCES

- Blackburn, E. A., Wilson, L., and Sparks, R. S. J., (1976), Mechanisms and dynamics of strombolian activity, Jour. Geol. Soc. London, 132, pp. 429-440.
- Briggs, G. A., (1969), Plume Rise, U.S.A.E.C. Critical Review Series, NTIS Report No. TID-25075, 81p.
- Donn, W., and Balachandran, N., (1981), Mount St. Helens Eruption of 18 May 1980: Air Waves and Explosive Yield, Sci, 213, pp 539-541.
- Gorshkov, G. S., (1959), Gigantic eruption of the Volcano Bezymianny, Bull. Volcanol., 20, pp. 77-109.
- Gorschkov, G. S., (1980), Determination of the explosion energy in some volcanoes according to barograms, Bull. Volcanol., vol 23, pp 141-144.
- Guerra, C. I., et al, (1978), Stromboli and its 1975 eruption, Bull. Volcanol., 41-3, pp. 259-285.
- Herdervari, P., (1963), On the energy and magnitude of volcanic eruptions, Bull. Volcanol., 25, pp. 373-385.
- Kienle, J., and Shaw, G. E., (1979), Plume dynamics, thermal energy and long-distance transport of Volcanian eruption clouds from Augustine Volcano, Alaska, Jour. Volcanol. & Geothermal Res., 6, pp. 139-164.
- Knox, J. B., and Short, N. M., (1964), A diagnostic model using ashfall data to determine eruption characteristic and atmospheric conditions during a major volcanic event, Bull. Volcanol., 27, pp. 5-24.
- Le Guern, F., Bernard, A., and Chevrier, R. M., (1980), Soufriere of Guadeloupe 1976-1977 eruption-mass energy transfer and volcanic health hazards, Bull. Volcanol., 43-3, pp. 577-593.
- Liu, C., Klostermeyer, J., Yeh, K., Jones, T., Robinson, T., Holt, O., Leitinger, R., Ogawa, T., Sinno, K., Kato, S., Bedard, A., and Kersley, L., (1982), Global Dynamic Responses of the Atmosphere to the Eruption of Mount St. Helens on May 18, 1980, Jour. Geophys. Res., 87, pp 6281-6290.
- McBirney, A. R., (1973), Factors governing the intensity of explosive andesitic eruptions, Bull. Volcanol., 37, pp. 443-453.
- Melson, W. G., and Saenz, R., (1973), Volume, energy and cyclicity of eruptions of Arenal Volcano, Costa Rica, Bull. Volcanol., 37-3, pp. 416-437.
- Minakami, T., (1950), On explosive activities of andesitic volcanoes and their forerunning phenomena, Bull. Volcanol., 10, pp. 59-87.

- Newhall, C. B., and Self, S., (1982), The Volcanic Explosivity Index (VEI): an estimation of explosive magnitude for historic volcanism, Jour. Geophys. Res., 87 (Green), pp. 1231-1238.
- Roberts, D. H., Klobuchar, J., Fougere, P. F., and Hendrickson, D.H., (1982), A Large-Amplitude Traveling Ionospheric Disturbance Produced by the May 18, 1980, Explosion of Mount St. Helens, Jour. Geophys. Res., 87, pp 6291-6301.
- Settle, M., (1976) Rise of Volcanic Eruption Clouds: Relationship between Cloud Height and Eruption Intensity, Air Force Geophysical Laboratory Technical Report AFGL-TK-76-0127, 37 p.
- Settle, M., (1978), Volcanic eruption clouds and the thermal power output of explosive eruptions, Jour. Volcanol. and Geothermal Res., 3, pp. 309-324.
- Sparks, R. S. J., and Wilson, L., (1976), A model for the formation of ignimbrite by gravitational column collapse, Jour. Geol. Soc. London, 132, pp. 441-451.
- Sparks, R. S. J., and Wilson, L., (1982), Explosive volcanic eruptions-V. Observations of plume dynamics during the 1979 Soufriere eruption, St. Vincent, Geophys. J. R. Astr. Soc., 69, pp. 551-570.
- Steinberg, G. S., (1976-77), On the determination of the energy and depth of volcanic explosions (Paper dedicated to G. S. Gorshkov), Bull. Volcanol., 40-2, pp. 116-120.
- Tokarev, P. I., (1978), Prediction and characteristics of the 1975 eruption of Tolbachik Volcano, Kamchatka, Bull. Volcanol., 41-3, pp. 251-258.
- Walker, G. P. L., (1973), Explosive volcanic eruptions - a new classification scheme, Geol. Rundsch., 62, pp. 431-446.
- Wilson, L., (1976), Explosive volcanic eruptions-III. Plinian eruption columns, Geophys. J. R. Astr. Soc., 45, pp. 543-556.
- Wilson, L., Sparks, R. S. J., Huang, T. C., and Watkins, N. D., (1978), The control of volcanic column heights by eruption energetics and dynamics, Jour. Geophys. Res., 83, pp. 1829-1836.
- Wilson, L., (1980), Relationships between pressure, volatile content and ejecta velocity in three types of volcanic explosion, Jour. Volcanol. Geo. Res., 8, 297-313.
- Wilson, L., Sparks, R. S. J., and Walker, G. P. L., (1980), Explosive volcanic eruptions-IV. The control of magma properties and conduit geometry on eruption column behavior, Geophys. J. R. Astr. Soc., 67, pp. 117-148.
- Yokoyama, I., (1956), Energetics in active volcanoes, first paper, (Activities of volcano Mihara, Ooshima Island during the period 1953-54), Bull. Earthq. Res. Inst., 34, 1956.

Yokoyama, I., (1957), Energetics in active volcanoes, second paper, Bull.
Earthq. Res. Inst., 35, pp. 75-96.

Yokoyama, I., (1957), Energetics in active volcanoes, third paper, Bull.
Earthq. Res. Inst., 35, pp. 99-106.

APPENDIX E

Selected References on the Propagation Characteristics
of Acoustic-Gravity Modes in the Atmosphere

REFERENCES

- Bhartendu, and Currie, B. W., (1963), Atmospheric waves from U.S.S.R. nuclear test explosions in 1962, Canadian Jour. Physics, 42, pp. 632-637
- Burridge, R., (1971), The acoustics of pipe arrays, Geophys. J. R. Astr. Soc., 26, pp. 53-69.
- Donn, W. L., and Ewing, M., (1962), Atmospheric waves from nuclear explosions, Jour. Geophys. Res., 67, pp. 1855-1866.
- Donn, W. L., and Shaw, D. M., (1967), Exploring the atmosphere with nuclear explosions, Rev. Geophys., 5, pp. 53-82.
- Douze, E. J., and Sorrells, G. G., (1974), Prediction of pressure generated earth motion using optimum filters, Teledyne Geotech Technical Report No. 74-6, 3401 Shiloh Road, Garland, Texas 75041.
- Einaudi, F., and Hines, C. O., (1970), WKB approximation in application to acoustic-gravity waves, Canadian Jour. Physics, 48, pp. 1458-1471.
- Ericsson, U., (1962), Microbarographic waves from nuclear explosions, Kosmos (Cosmos) annual of the Swedish Society of Physicists, 40, 1962, pp. 187-208, Translation.
- Fix, J. E., (1972), Ambient earth motion in the period range from 0.1 to 2560 sec, Bull. Seis. Soc. Am., 62, pp. 1753-1760.
- Goerke, V. H., Young, J. M., and Cook, R. K., (1965), infrasonic observations of the May 16, 1963, volcanic explosion on the island of Bali, Jour. Geophys. Res., 70, pp. 6017-6022.
- Greenfield, R. J., and Harkrider, G. D., (1971), Acoustic-gravity wave calculations in a layer with a linear temperature variation, Geophys. J. R. Astr. Soc., 26, pp. 323-339.
- Grover, J. H., (1971), Experimental noise reducers for an active microbarograph array, Geophys. J. R. Astr. Soc., 26, pp. 41-52.
- Harkrider, D. G., (1964), Theoretical and observed acoustic-gravity waves from explosive sources in the atmosphere, Jour. Geophys. Res., 69, pp. 5295-5321.
- Jones, R. V., (1962), Sub-acoustic waves from large explosions, Nature, 193, pp. 229-232.
- Larson, R. J., Craine, L. B., Thomas, J. E., and Wilson, C. R., (1971), Correlation of winds and geographic features with production of certain infrasonic signals in the atmosphere, Geophys. J. R. Astr. Soc., 26, pp. 201-214.
- Mac Kinnon, R. F., (1967), The effects of winds on acoustic-gravity waves from explosions in the atmosphere, Geophys. Jour., pp. 436-454.

REFERENCES (continued)

- Murphy, A. J., and Savino, J. M., (1974), A comprehensive study of long-period (20-200 sec) earth noise at the high-gain world-wide seismograph stations, Lamong-Doherty Geological Observatory of Columbia University, Palisades, New York 10964.
- Pierce, A. D., Theoretical source models for the generation of acoustic-gravity waves by nuclear explosions, Dept. of Mech. Eng., MIT, Cambridge, Mass 02139.
- Pierce, A. D., (1966), Guided infrasonic modes in a temperature and wind-stratified atmosphere, Jour. Acoust. Soc. Amer., 41, pp. 597-611.
- Pierce, A. D., and Posey, Joe W., (1971), Variation of nuclear explosion generated acoustic-gravity wave forms with burst height and with energy yield, Jour. Geophys. Res., 76, pp. 5025-5042.
- Posey, J. W., and Pierce, A. D., (1971), Estimation of nuclear explosion energies from microbarograph records, Nature, 232, pp. 71.
- Press, F., and Ewing, M., (1951), Theory of air-couples flexural waves, Jour. Appl. Phys., 22, pp. 892-899.
- Sorrells, G. G., and Douze, E. J., (1974) Studies of long-period seismic noise generated by atmospheric pressure changes, Teledyne Geotech Technical Report No. 74-5, 3401 Shiloh, Garland, Texas.
- Sorrells, G. G., and Goforth, T. T., (1973), Low-frequency earth motion generated by slowly propagating partially organized pressure fields, Bull. Seis. Soc. Am., 63, pp. 1583-1601.
- Sorrells, G. G., McDonald, J. A., Der, Z. A., and Herrin, E., (1971), Earth motion caused by local atmospheric pressure changes, Geophys. J. R. Astr. Soc., 26, pp. 83-98.
- Thomas, J. E., Pierce, A. D., Flinn, E. A., and Craine, L. B., (1971), Bibliography on infrasonic waves, Geophys. J. R. Astr. Soc., 26, pp. 399-426.
- Wagner, H., and Ericsson, U., (1963), Period and amplitude in atmospheric gravity waves from nuclear explosions, Nature, 197, p. 994.
- Weston, V. H., and Van Hulsteyn, D. B., (1962), The effect of winds on the gravity wave, Canadian Jour. of Physics, 40, pp. 797-804.
- Wexler, H., and Hass, W. A., (1962), Global atmospheric pressure effects of the October 30, 1961, explosion, Jour. Geophys. Res., 67, pp. 3875-3887.
- Wilson, C. R., and Forbes, R. B., (1969), Infrasonic waves from Alaskan volcanic eruptions, Jour. Geophys. Res., 74, pp. 4511-4522.
- Ziolkowski, A., (1973), Prediction and suppression of long-period nonpropagating seismic noise, Bull. Seis. Soc. Am., 63, pp. 937-958.

APPENDIX F

Abstracts of Papers Presented

American Geophysical Union
Annual Fall Meeting
San Francisco, California
December 7-15, 1982

An Approach to Estimation of Volcanic Explosion Energy Using
Propagated Infrasonic-Acoustic Waves

FREDERICK J. MAUK
GORDON G. SORRELLS
LORI GRANT
KENNETH TAYLOR

(Teledyne Geotech Geophysical Research Department,
3401 Shiloh Road, Garland, Texas 75041)

A desirable and elusive geophysical measurement is the energy associated with explosive volcanic eruptions. Total energy quantification is difficult because it involves both thermal and kinetic energy contributions which are temporally complex. Far-field volcanic explosion evaluation which is analogous to earthquake moment estimation may be possible using propagated infrasonic-acoustic waves. The method was first proposed by Gorshkov (1959) who used the infrasonic signals recorded on remote millibarographs to estimate large explosive energies of volcanoes in Kamchatka. Except for a brief period during the era of atmospheric nuclear weapons testing, the technique has been largely ignored. Utilizing data from the El Chichon eruption sequence recorded by a collocated microbarograph array and SKO instrumentation near McKinney, Texas, we have demonstrated that infrasonic-acoustic signals from volcanic explosions are well-recorded on SRO seismographs. By knowing the appropriate earth response characteristics, it is possible to derive the amplitude of the microbarometric fluctuations at the SKO site. Using the published amplitude and wave-period empirical relationships determined from atmospheric nuclear weapons tests, the excitation energy of the source can be derived. Estimations of the separate event energies for the El Chichon sequence of 29 March through 6 April 1982, using this technique and alternative methods, will be given.